pH-triggered Supramolecular Hydrogels

Rheology analysis, Modelling gelation times & Electrochemical patterning

Lakshminarayanan, V.

DOI
10.4233/uuid:c76c17aa-e647-4b5b-89a7-3dd90e20755f

Publication date
2024

Document Version
Final published version

Citation (APA)
Lakshminarayanan, V. (2024). *pH-triggered Supramolecular Hydrogels: Rheology analysis, Modelling gelation times & Electrochemical patterning*. [Dissertation (TU Delft), Delft University of Technology]. https://doi.org/10.4233/uuid:c76c17aa-e647-4b5b-89a7-3dd90e20755f

Important note
To cite this publication, please use the final published version (if applicable).
Please check the document version above.

Vasudevan Lakshminarayanan

pH-triggered Supramolecular Hydrogels

Rheology analysis, Modelling gelation times & Electrochemical patterning

pH-triggered Supramolecular Hydrogels – Rheology analysis, Modelling gelation times & Electrochemical patterning

Dissertation

For the purpose of obtaining the degree of doctor at Delft University of Technology
by the authority of the Rector Magnificus prof. dr. ir. T. H. J. J. van der Hagen
Chair of the Board of Doctorates
to be publicly defended on
Monday, 17th June 2024 at 15:00

by

Vasudevan LAKSHMINARAYANAN

Master of Science in Chemical Engineering, Delft University of Technology, The Netherlands
Born in Chennai, India

This Dissertation has been approved by the

Promotor: Prof. dr. J. H. van Esch

Second Promotor: Dr. hab. E. Mendes

Composition of the doctoral committee:

Rector Magnificus	Delft University of Technology	Chairman
Prof. dr. J. H. van Esch	Delft University of Technology	Promotor
Dr. hab. E. Mendes	Delft University of Technology	Promotor

Independent members

Prof. dr. A. del Guerzo	Université de Bordeaux, France	
Prof. dr. F. Hollmann	Delft University of Technology	
Prof. dr. S. J. Picken	Delft University of Technology	
Dr. ir. G. M. H. Meesters	Delft University of Technology	
Dr. P.E. Boukany	Delft University of Technology	Reserve member

Other members

Dr. I. Kryven	Utrecht University, The Netherlands

The work described in this thesis was carried out in the Advanced Soft Matter group at Delft University of Technology. This research was funded by programme 07A.11 of NanoNextNL, a Dutch consortium of 130 companies. Universities, knowledge institutes and university medical centres.

Cover Design: Proefschrijft Specialist, Zaandam

Printed by: Proefschrijft Specialist, Zaandam

I dedicate this thesis to

My Amma, Appa, my mentor Gabrie, my dear wife Rajamaadhanghi, my sister Bhuvaneswari and my friend Amrit

I am eternally grateful for your love, support, patience and encouragement

கற்றது கைமண் அளவு, கல்லாதது உலகளவு

- ஔவையார்

(Translation – Known is the amount of sand in the fist, Unknown is the total sand in the world)

Table of Contents

Chapter 1

Introduction

1.1 Hydrogels

Hydrogels are one of the most ubiquitously present materials in our lives right from food products such as jellies, oral hygiene products such as toothpaste, personal care products such as cosmetics, creams, personal hygiene products such as hair gels ,diapers, hand sanitisers to biomedical products such as wound dressings, supplements among others.[1–3] Hydrogels are unique among the class of soft materials comprising of polymers, elastomers, foams, colloids, liquid crystals etc. due to their high-water content, complex microstructure and stimuli responsiveness.[4–6] The term hydrogel was coined 1894 already and referred to colloidal gels.[7] The first biological application of a hydrogel based on Hydroxyethyl Methacrylate (HEMA) was already shown in 1960 by Wichterle and Lim.[8] But what is a hydrogel exactly?

A hydrogel is a solid-like easily deformable soft material that can contain up to 99% water (by weight) but does not flow naturally.[9,10] Hydrogels owe their unique visco-elastic properties to their internal structure formed either by cross-linked networks (polymers) or colloidal aggregates that entrap a large volume fraction of water.[9] Taking note of their inherent biocompatibility arising from the large internal aqueous environment, researchers in the recent years have developed numerous biomedical applications in the fields of cell culturing, tissue engineering, regenerative medicine, diagnostics etc.[11–13] Apart from providing a reservoir of growth medium, hydrogels also provide rigid support (scaffolds) which is essential for cell growth, proliferation and differentiation in the case of stem cells.[14,15] Besides the numerous biomedical applications, hydrogels also find uses in food industry (jellies, mayonnaise), cosmetics, paints, water treatment and oil remediation.[16–22] Beyond, science and materials, they have also contributed to culture through their use in art conservation as agents for cleaning precious paintings[23]. Hydrogels, hence have a broader societal impact.

1.2 Supramolecular hydrogels

Hydrogels can be classified in many ways based on the origin of material (natural vs. synthetic vs. hybrid), on their ionic charger (charged vs. non-charged), on their mechanical

properties (hard vs. soft, elastic vs. tough), but the most useful classification from a design perspective is based on the interactions which are involved in their formation of their internal 3-D structure.[7,9] Depending on the cross-linking that is present, hydrogels can classified as physically cross-linked, chemically cross-linked or radiation cross-linked hydrogels.[24,25] Chemically or radiation cross-linked hydrogel networks are formed via covalent interactions. Typically, this gel network has defined parts of the network where the cross-links are present and hence fixed in space. This is easily visualized in the schematic of Figure 1 as the red dots. Physically cross-linked hydrogels on the other hand are formed through non-covalent interactions such van der waals forces, hydrogen bonding, π-π interactions or host-guest interactions.

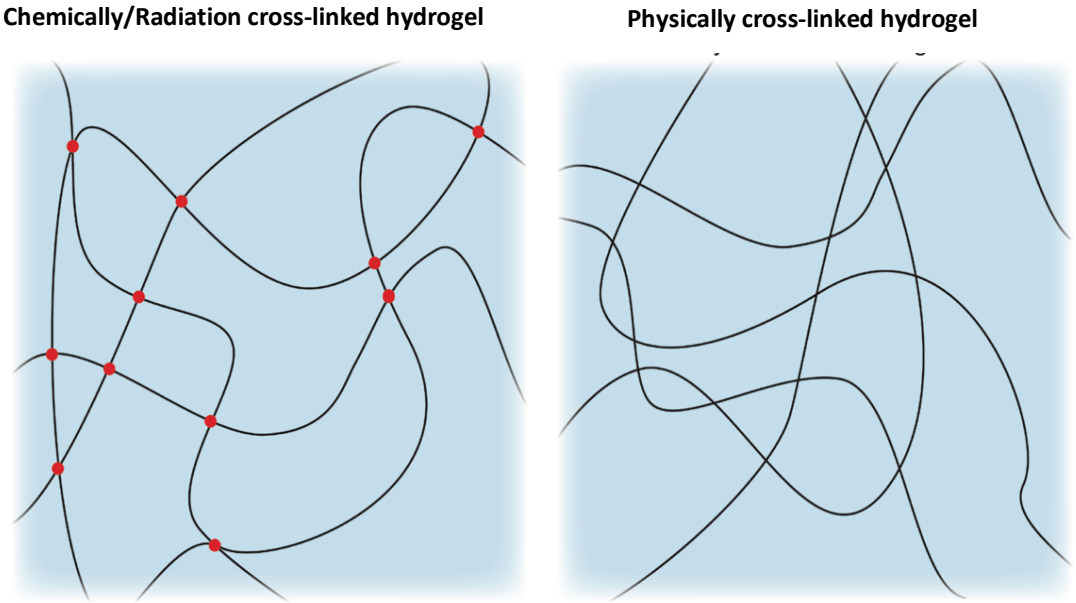

Figure 1. Schematic representation of chemically/radiation cross-linked hydrogel (left) with cross-link points represented as red dots vs. Physically cross-linked hydrogel (right). Image adapted from [9].

An example of chemically crosslinked hydrogel is pHEMA which is formed through radical polymerization of low molecular weight monomers (HEMA) in the presence of cross-linking agent (ethylene glycol dimethacrylate).[24] An example of a radiation cross-linked

hydrogel is Hydroxypropyl cellulose which forms a cross-linked hydrogels which irradiated with electron beam or gamma radiation. Covalently bonded 'permanent' hydrogel networks are mechanically strong but rupture easily at high stress.[9] Additionally, when they need to be used for biomedical applications, they need to be flushed off cross-linking agents that are usually harmful.[24] Physically cross-linked hydrogels are softer but inherently do not need to be flushed to remove harmful chemical cross-linking agents. The non-covalent interactions also provide these hydrogels with interesting dynamic properties such as reversibility, self-healing and thixotropicity.[26–28] These arise due to the individual hydrogel fragments to reform their network after the removal of stress. In scientific literature this class of hydrogels are often referred as Supramolecular hydrogels.[29,30] Depending on the molecular structure, supramolecular gels can be made from macromolecules such as synthetic polymers, biopolymers, DNA or Low Molecular Weight Gelators (LMWGs). Some authors categorize the supramolecular gels from macromolecules as separate subclass of physical gels called as 'supramacromolecular' (SMM) gels and not under supramolecular hydrogels (see Figure 2a).[31] However, in scientific literature these gels are commonly grouped under the name of supramolecular hydrogels.[30,32]

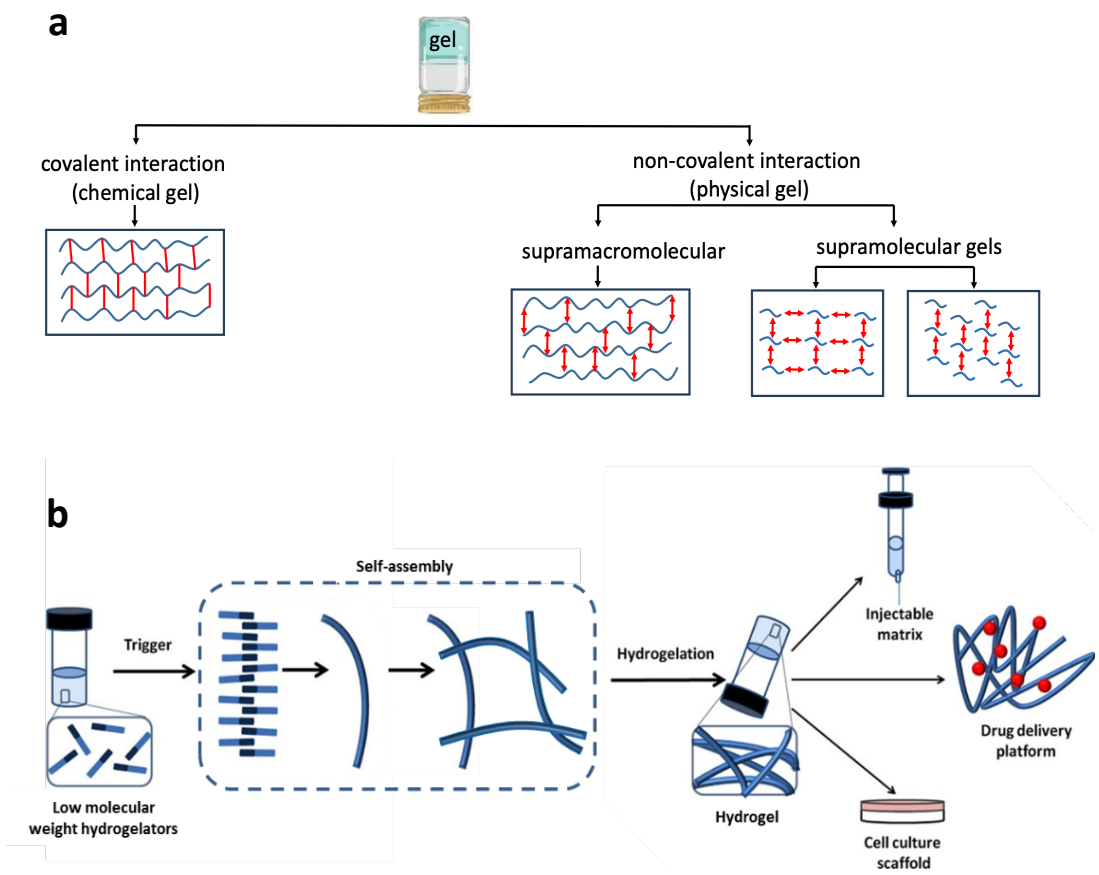

Figure 2. Schematic of gel classification reproduced from [31][a]. Schematic representation of formation of supramolecular gel from Low Molecular Weight Hydrogelators (LMWHs), reproduced from [26].

Some examples of supramacromolecular gels include polysaccharide-based hydrogels such as chitosan, dextran, pullulan which form due to hydrophobic interactions which cause the polymer strands to swell to form a gel.[33,34] Other forms of interactions that can have been shown to form physically cross-linked hydrogels are electrostatic interactions (Ca^{2+} and alginate system), stereocomplex formation (involving interaction between lactic acid and oligomers of opposite chirality), protein interactions in copolymers containing silk-like and elastin like blocks (Prolastins)leading to crystallization of silk-like domains), hydrogen bonding induced complex formation in Poly Acrylic Acid (PAA) or Poly Methacrylic

Acid (PMA) with Polyethylene glycol (-COOH group of PAA/PMA and Oxygen in PEG).[33,35] Additionally, host-guest interactions between macrocyclic hosts such as Cucurbiturils, Cyclodextrins and guests such as cationic amines, metal or imidazolium ions, adamantane have been shown to form physically cross-linked hydrogels by incorporating the hosts on polymer chains.[26,36–38] SMM gels from DNA or modified DNA material such as aptamers have also been reported especially in the context of biomedical application.[39] SMM gels from synthetic polyisocyanopeptides grafted with oligomers of ethylene glycol have shown the formation of physically cross-linked hydrogels at low concentrations and strain stiffening, an important biomimetic property similar to gels from cytoskeletal proteins.[40] Due to large volume of scientific output in this area, the curious reader is referred to a set review articles for further reading.[33,34,41,42] In this thesis, the focus is on another class of supramolecular hydrogels that are formed by physically cross-linked fibres created by the self-assembly of small molecules. These molecules also referred to as Low Molecular Weight Hydrogelators (LMWHs) self-assemble through non-covalent interactions and form a fibrous network spanning the volume of the solvent to form the hydrogel (see Figure 2.).[26] Depending on the design and chemical modifications made on the molecule itself, the structure, mechanical properties, stimuli-response of the resulting hydrogel can be controlled thus making them sophisticated tuneable soft materials.[43–47] In the next section, the key LMWH systems developed over the years and triggers for forming supramolecular hydrogels are discussed.

1.3 Low Molecular Weight Hydrogelators and Triggering Systems

Much of the earlier reported work in this field of LMWHs were related to serendipitous discovery based on trial and error.[48] One of the earliest reports on a LMWH based supramolecular hydrogel was from an amino acid (Cystine) derivative called DBC (N-N' Dibenzoyl-L-Cystine).[49–51] DBC self-assembles via hydrogen bonding between the carboxylic acid group and interactions between the aromatic ring.[52] By studying this system a number of L-Cystine based gelators were later synthesized and shown to form hydrogels at various sub millimolar concentrations.[53,54] This library approach is one of the unique

aspects of the LMWHs since a motif such as L-Cystine can be used a chassis to build different functionalities on top through chemical functionalization. It is however good to note that not all modifications of a base gelator possess gelating properties since some of them can crystallize and precipitate out.[55] Researchers even acknowledge this challenge since it is difficult to predict whether a gelator will have the interactions to favour a 1-dimensional fibre structure that can form a physically entangled network.[56] Despite the challenges, many groups including ours, have synthesized and characterized different LWMHs and have identified new LMWG motifs aiding in rational gelator design.[43,57–62] These motifs include N-protected dipeptides such as (Fmoc) diphenylalanine, bola amphiphilic peptides, and amphipathic peptides.[46,56,60,63–66] In our group, there has been focus onto gelator motifs such as urea bisamides and C-3 symmetric cyclohexane/benzene amino acid based gelators[57,58,67–71]. The figure below (see Figure 3.) provides a quick visual summary of some of the LMWH motifs reported in scientific literature.

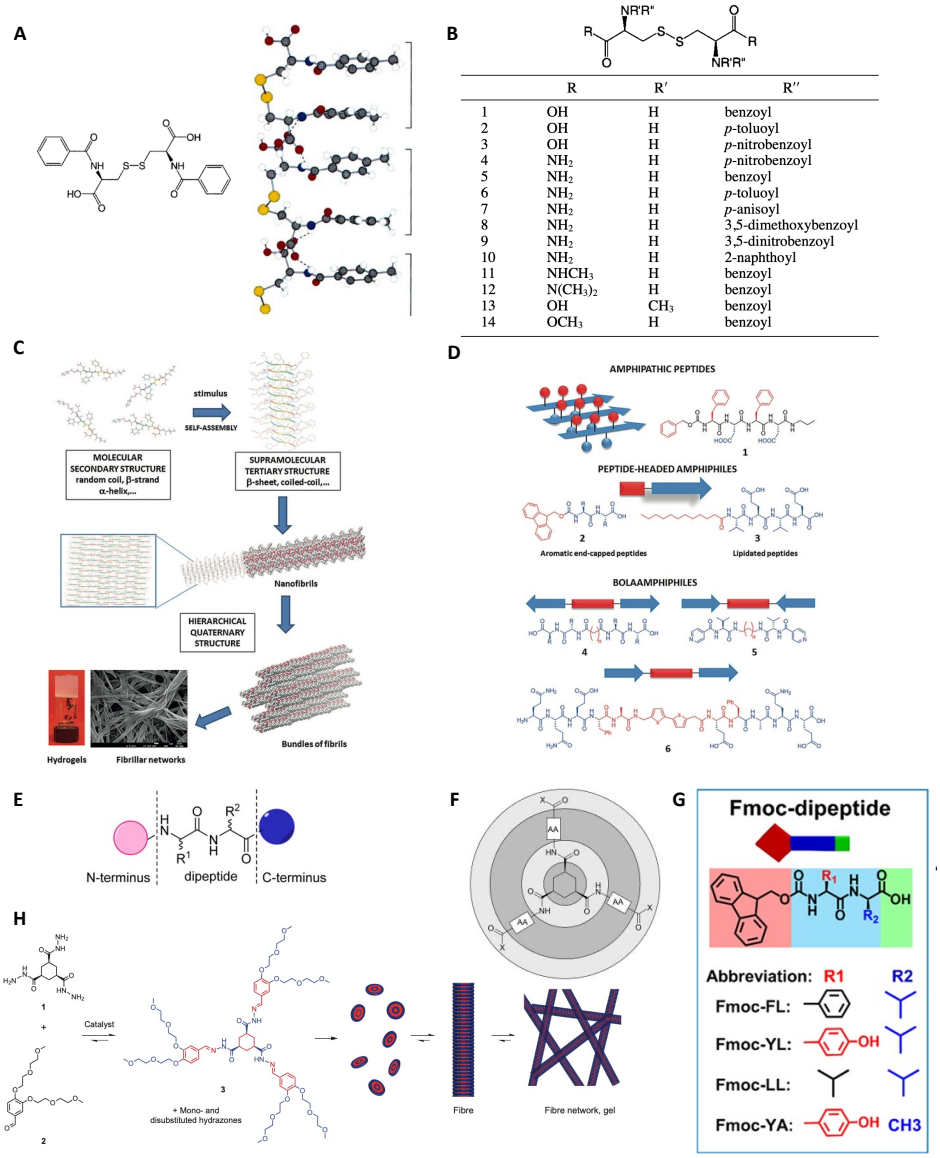

	R	R′	R″
1	OH	H	benzoyl
2	OH	H	*p*-toluoyl
3	OH	H	*p*-nitrobenzoyl
4	NH_2	H	*p*-nitrobenzoyl
5	NH_2	H	benzoyl
6	NH_2	H	*p*-toluoyl
7	NH_2	H	*p*-anisoyl
8	NH_2	H	3,5-dimethoxybenzoyl
9	NH_2	H	3,5-dinitrobenzoyl
10	NH_2	H	2-naphthoyl
11	$NHCH_3$	H	benzoyl
12	$N(CH_3)_2$	H	benzoyl
13	OH	CH_3	benzoyl
14	OCH_3	H	benzoyl

Figure 3. Molecular structure and schematic stacking model of N-N' Dibenzoyl-L-Cystine hydrogelator [A] (adapted from [55] and [72]); Table showing a library of LMWHs based on L-Cystine motif [B] (adapted from [55]); Self-assembly process of peptide based gelators including, secondary, tertiary structures, fibrils, fibre bundles and hydrogel network [C] (reproduced from [60]); Schematic representation of different peptide-based gelator systems [D] (reproduced from [60]); Schematic representation dipeptide LMWH motif [E] (reproduced from [73]); Schematic of cyclohexane based LMWH motif [F][H] (reproduced from [58] and [74]); Visual of Fmoc-dipeptide LMWH motif [G] ([75])

A number of triggering systems have also been developed for the formation of supramolecular gels from LMWHs. The motivation for the development of these triggers beyond controlling gel formation were to understand gelation kinetics, tuning mechanical properties or bringing these systems closer to biomedical applications.[76–78] The triggers that have been reported in literature are solvent-switch, temperature, pH, catalysts, enzymes, light, ionic strength, redox-reactions, ultrasound,, electrochemistry.[47,51,55,59,78–80] These examples come both from the world of More recently, researchers are working on multicomponent hydrogels where a combination of triggers are used to further tune gel properties and applications.[81–83]

Solvent-switching along with temperature are the earliest reported triggers for supramolecular gel formation. Solvent-switching involves the dissolution of LMWHs in an organic solvent (such as DMSO) and then introducing another solvent such as water.[55,84] The difference in polarities between the solvent and non-solvent, lead to the aggregation/self-assembly of LMWHs resulting in a gel network that spans the volume of the non-solvent (water). DBC, an L-cystine based gelator has been shown to form gels through the solvent switching from an organic solvent to water.[51] Temperature triggering involves heating gelator solutions till they are dissolved and cooling them down to form gels. Some examples include urea bisamide type gelators, L-Cystine based gelators, Fmoc-dipeptides, some of the cyclohexane based gelators.[58,63,67,69,85,86]

pH-triggering has reported since several decades as a method to form supramolecular gels at room temperature. The method is especially applicable on gelator motifs that contain carboxylic acid (-COOH) or amine groups which are capable of deprotonation and protonation respectively at alkaline and acidic conditions.[58,87,88] Hence by lowering the pH using acids or acidulants (< pKa) or raising the pH using bases, supramolecular gels can be formed. An example of acid-triggered LMWH is DBC which forms gels a low pH.[86,87] Fmoc-dipeptide based gelators have been shown to form gels at near neutral pH[89,90] Amine or pyridine functionalized gels are stable basic pH.[91] Besides strong acids like HCl, researchers

have also shown the acidulants such as glucono-δ-lactone, acid anhydrides can also be used as pH-triggers for a more gradual reduction in pH and thereby influencing the kinetics of supramolecular formation.[88,92]

Catalysts and enzymes catalyse the formation of the hydrogelator molecule from two or reactive subunits. The formed hydrogelator molecule thus self-assembles to form a hydrogel network. By controlling the catalyst or enzyme concentration, the kinetics gel formation can be controlled.[74,93] Examples include the cyclohexane tris hydrazone gelator motif shown in Figure 3. (see 3H) which can be catalysed by H^+ or Aniline.[94] Another example of catalytic control is the work of Escuder et.al on the use of L-Proline to catalyse the aldol reaction of cyclohexanone and p-nitrobenzaldehyde.[95] An example of enzymatic control over hydrogel formation is the use of alkaline phosphatase to from the gelator from its precursor thus triggering self-assembly and hydrogel formation.[96]

To bring a new dimension of controlling gelators, light-triggers have been developed and reported by several researchers over the years. The approaches here consisted of i) smart molecular gelator design by incorporating moieties that exhibit photo-isomerism or ii) using molecular switches that activate upon light irradiation or iii) incorporating moieties that undergo photo-dimerization iv) using pH- or catalyst triggered gelator systems in combination with a photoacid generator (PAG) or photocatalyst.[79,97–99] In approach i) the gelator typically has a azobenzene or derivative incorporated into it. Upon irradiation of UV light (340 nm), the azobenzene undergoes isomerization from trans to cis.[79] The trans form is the thermodynamically stable form which gets disrupted during light irradiation. By coupling this to LMWG motifs, researchers have been to control the formation and disassembly of supramolecular gels. The concept was first shown in an organogel system by Shinkai et.al but later also extended to LMWHs by Ulijn et.al who incorporated into dipeptides to produce a light triggered supramolecular hydrogels.[79,100,101] In approach ii) molecular switches such as spiropyran (SP) which undergo light-induced transition to merocyanine (MC) under UV light exposure.[99] SP in non-planar whereas MC is planar and

therefore can facilitate π-π stacking thus leading to gel formation when conjugated to a LMWH motif.[79,102] This was shown by Zhang et.al who conjugated SP with a dipeptide to be able to form fibrous hydrogel network in response to light.[103] One proof of principle for approach iii) is the work of Parquette and Grinstaff et al. where they reported on a LMWH in which two coumarins were connected to both the N-terminal and N-ε side chain free amine (-NH2) of a well-explored β-sheet forming dipeptide, dilysines.[104] The LWMH self-assembled to form a gel which increased in mechanical strength under UV light due to the photo-dimerization. The system was also shown by Adams et.al by conjugating to one of their commonly explored dipeptide LMWH motifs.[105] Some examples of approach iv) include again the work of Adams et.al on their dipeptide gelator motif using diphenyliodonium nitrate (DPIN) as PAG to bring the pH of solution below the pKa to facilitate self-assembly and gel formation, the work of our group on using visible light triggered conversion of SP to MC to control the pH which in turn was used to catalyse the formation of earlier reported cyclohexane tris hydrazone gelator to form supramolecular gels in a controlled manner.[106,107]

On ionic strength, it has been reported that the addition of salts such as to gelator solutions can trigger the formation of hydrogels by driving the hydrophobic interactions that drive self-assembly of gelator molecules.[108] To create redox-triggering/responsive capabilities, researchers have introduced into ferrocene moieties into hydrogel motifs (polymeric and supramolecular alike).[109] In the case of LMWHs, ferrocene containing peptides such as ferrocenoyl phenylalanine have been shown form to hydrogels which undergo gel-sol transition in the presence of oxidizing agents such as hydrogen peroxide.[110] The reason is due to the loss of aromaticity of Ferrocene by forming Ferrocenium cation. This disrupts the stability given to the dipeptide LMWH motif and thus forming a sol.[110] Many other examples of redox responsive supramolecular hydrogels are summarized in this review article for the curious reader.[109]

Ultrasound induced formation of supramolecular gels has been reported for the organogel systems and referred to as sonogels.[78,111] However there are examples in the scientific literature showing hydrogel formation upon exposure to ultrasound. Wu et al. demonstrated the formation of supramolecular hydrogels from dipeptides through sonication in the presence of $NaYF_4$ nanoparticles.[112] In another example, Stevens et al. ultrasound was used to permeabilize liposomes loaded with Ca^{2+} ions, these ions in turn activated the enzyme transglutaminase which catalysed intra and intermolecular cross-linking of fibrinogen to forma hydrogel.[113] In a more recent example, aspartic acid derivative N,N'-diaspartate-3,4,9,10-perylene tetracarboxylic acid imide (NAAPD) was dissolved in a mixture of water and THF to form a suspension which upon ultrasound exposure for ~ 2 hours formed a gel.[114]

Electrochemical triggering of hydrogels as a strategy has been primarily employed on pH-triggered or redox-triggered LMWHs to form supramolecular hydrogels.[82,109] Cameron et. al demonstrated the formation of nanometre thick hydrogel membranes in N-protected dipeptide Fmoc-Leu-Gly-OH through electrochemical oxidation of hydroquinone (HQ) to benzoquinone (BQ) which releases protons at the electrode solution interface and trigger gelator self-assembly.[115] This approach was later used by the group of Dave Adams for growing millimetre thick hydrogel layers from multiple dipeptide gelators to form hydrogels with varying chemical composition.[82] Recently, this method has also been used to form large volume (~ 3 cm^3) of di and tripeptide hydrogels using the same electrochemical pH-triggering system under inert atmosphere (to prevent air oxidation of HQ).[116] Some examples based on electrochemically triggered sol-gel transitions are based on the inclusion of redox active compounds such as Tetrathiafulvalene (TTF) or Ferrocene that undergo oxidation to form their respective cations.[117] Application of positive and negative potential has been used to shown reversible tuning of gel formation and properties.[117]

Finally, it is worth noting that researchers have tried to combine a number of triggers and gelator design/combination to develop strategies to produce what are called multistimuli-

responsive supramolecular gels that respond to multiple triggers.[117] These approaches have been shown to provide a greater control in drug delivery, sensing, diagnostics and other biomedical applications.[11,110,117,118] Additionally, the different triggers have enabled to also control self-assembly and structuring of supramolecular gels formed by LMWHs.[9]

1.4 Directed Self Assembly & Structuring of Supramolecular hydrogels

Structuring hydrogels as such is a vast domain with several decades of work. As stated before, in this thesis, the focus is on LMWHs. Hence in this section, we will take a look at the strategies employed over years to direct self-assembly and structuring of supramolecular hydrogels formed from them. However it is worth noting that polymeric hydrogels have been microfabricated through a number of top down approaches such as photolithography, micro moulding, 3D-printing and stop-flow lithography.[9] To cater to the limitations of these approaches (resolution, limitations from capillary forces, elasticity of materials) novel micro structuring using Aqueous two/three system-based approaches have also been proposed.[9] In the case of LMWHs, structuring strategies usually combine top-down with bottom up approaches. This is approach is relatively new waiting to be further explored and understood.[9]

The control over self-assembly can be understood from multiple lenses but one of the dominant motivations for control self-assembly and structuring is to be able to produce structures and systems that respond similar to living organisms or systems.[119] Living beings are macroscopic objects which have programmed micro and nanostructures with well-defined functions. A cell has a number of different organelles each of which have its own defined structure and function.[120] Researchers have hence attempted to develop methods and strategies to achieve this control over self-assembly and structuring at different length scales.

At the macroscopic scale, the simplest way to control the structure/shape/ can be achieved by controlling the shape of the container in which the supramolecular gel is formed. Once

formed, it is difficult to remove the hydrogel without the destroying its network structure due to their softness. To tune the mechanical properties, researchers have introduced polymer crosslinkers to strengthen the gel network.[121] The obtain gels were could be formed and removed while retaining the shape.[122] Other recent strategies such as reaction-diffusion have also been shown to form macroscopic objects and patterns based on the localization of the reactants in a scaffold gel network.[123] Based on the desired pattern, localized reactants diffuse and combine at the interface to form a hydrogelator that self-assembled to form networked hydrogel. To make the objects free-standing, the scaffold gel network is removed using a chemical agent (such as EDTA).[123] It is also possible to scale down the approach to micro-scale through wet stamping of the reactant solutions in specific patterns.[123] Furthermore, electrochemical pH-triggering of LMWGs using a conducting substrate such as fluorine-doped tin oxide (FTO) coated glass and hydroquinone oxidation has been used to produce macroscopic (few mm) hydrogel shapes. Through masking selected portions, a second hydrogel network was produced thus resulting in a spatially resolved multicomponent gel network.[82] Ulijn et.al demonstrated the formation of ~ 1mm wide temporary hydrogel scaffold based on electrochemical pH-triggering of Fmoc-dipeptide gelators.[124] This scaffold was further used for the formation of a thermoresponsive hydrogel based on agarose.[124] The size of the scaffold and formed agarose gel was determined by the width of the electrode surface.[124]

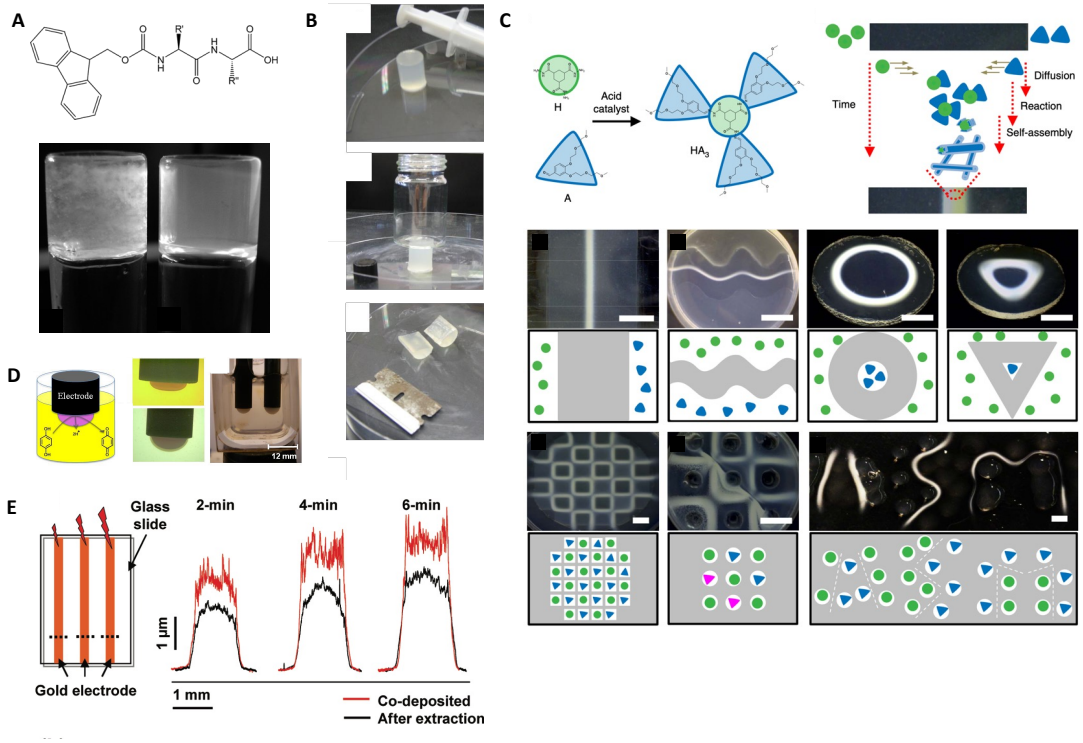

Figure 4. Schematic of Fmoc-dipeptide (top) and formed hydrogels using HCl (left) and GDL triggering (right) [A] (adapted from [88]; Macroscopic PEG-crosslinked LMWG hydrogels that retained shape after squeezing out of the syringe in which they were formed [B] (adapted from [121]); Schematic of reaction-diffusion LMWH system and formed hydrogel patterns [C] (adapted from [123]); Electrochemically pH-trigged formation of supramolecular hydrogel at electrode interface [D] (adapted from [82]); Electrochemically assisted formation agarose gel using temporary scaffold of pH-triggered LMWH [E] (adapted from [124]).

At the microscopic scale, gel self-assembly and structure have been controlled through a combination of top-down approaches and bottom strategies but also through understanding and controlling parameters influencing kinetics of supramolecular gel formation. Beyond wet stamping in the case of reaction-diffusion, negative charged catalytic surfaces been used to direct self-assembly of LMWHs.[125] Olive et al. showed by patterning sulfonic acid groups through microcontact printing, patterned hydrogel through local H^+ catalysis can be achieved.[125] This concept was later extended to polymeric brush patterns

that acted as catalytically active templates to form micro-patterned hydrogels.[126] Maity et.al showed the formation of sub-milli and micro-patterned LMWH hydrogels through the use of a light triggered photoacid.[107] By laser printing a mask on a transparent sheet, Maity et.al controlled irradiation of pre-gel solution and directed self-assembly and structuring only the location of the radiation.[107] Smith et.al have shown the formation of photo-patterned multi domain LMWH gels using a 2-step acidification of 1,3:2,4-dibenzyldene-d-sorbitol (DBS) derivative with the help of GDL and a photoacid.[81,127]

Understanding kinetics and structuring and thus controlling self-assembly in LMWHs has been shown in across micro and nano scales. A simple example of one-dimensional kinetic control was shown by Ziemecka et.al through a pH wave that directed the orientation of DBC hydrogel fibres to the direction of propagation of the pH wave.[87] Furthermore, through slow acidification using GDL and anhydrides, Adams et.al showed that different network structures can be accessed in Fmoc dipeptide LWMH system, a more homogenous transparent gel network under slow acidification and a non-homogenous turbid network under fast gelation.[88] Later the same group showed that kinetics does not dominate the mechanical properties of GDL-triggered LMWH hydrogels from selected Fmoc dipeptide.[65] They hypothesized that that close to pKa the LWMHs formed worm-like micelles which entangle. Also, there is an influence of final pH on the mechanical properties of the obtained gels.[128] Upon further of pH, stiffening of the structures, lateral association lead to stiffer structures of hydrogels. Later Baccile et.al showed that kinetics (rate of acidification) played a role in the self-assembly and mechanical properties of hydrogels formed from stearic acid sophorolipids which undergo micelle to ribbon transition at physiological pH.[129] They reported no dependence between mechanical properties and final pH but did positively report on its dependence on kinetics.[129] Very recently, Draper et.al showed that perylene bisimides hydrogelator can form different gels based on starting pH and solution history with possibility to change structure by reprogramming via pH.[130] The understanding of kinetics-structure dependence of pH-triggered LMWHs is hence gelator and system dependent with room for further exploration. Besides, pH-triggered LWMHs, directed self-assembly using

catalytic liposomes and nanoparticles have also been reported in the recent years to form hydrogel fibres that originate from the catalytic surface.[131,132]

These kinetically or pathway controlled self-assembly processes represent one of the self-assembly mechanisms that is outside of thermodynamic equilibrium. By controlling of rate at which different competing reactions can happen (gelation vs. reduction), Thordarson et.al have shown the formation of transient hydrogel structures using LMWHs (DBC).[133] Very recently, researchers have coupled pH-triggered LMWH to a reaction–diffusion system to achieve transient and directional growth of supramolecular hydrogels with controlled width maxima and lifetimes.[134] Another of self-assembly is far from equilibrium or out of equilibrium self-assembly that occurs in the presence of the energy rich fuels. The consumption of the fuel causes the creation of transient structures which are kinetic-controlled by fuel levels. Once the fuel is depleted, the structure disappears. Microfilaments and microtubules in cells are formed by self-assembly of actin and tubulin and respectively driven by adenosine triphosphate (ATP) and guanosine triphosphate (GTP). Researchers have attempted to mimic the transient structures using LMWH and an alkylating agent to form a transient hydrogel that disappeared when the fuel level was depleted.[135] Chemical fuels

Beyond the world of single component supramolecular gels, directed self-assembly also exists in multi component supramolecular hydrogels. Based on the reported scientific works mechanism of self-assembly can be i) co-assembly, ii) random assembly and iii) self-sorting.[136,137] Panja et.al showed very recently that multicomponent LMWHs can be controlled to co-assembled vs. self-sorted networks by varying hydrophobicity or by changing preparative pathway.[138] Also, chemically fuelled self-sorting supramolecular hydrogels have been recently prepared through careful selection of gelator system and chemical fuels.[139]

Overall, the understanding of kinetics, structure and strategies for structuring of LMWGs continues to be as relevant today as it was several decades ago. One of the key aspects to keep in mind is that gelation using LMWHs is a formulation science problem with a number of contributing factors as acknowledged by leading investigators in this domain.[10] While new synthetic approaches for creating library of gelators is definitely welcome, it is also important to further the understanding of existing well-studied gelator motifs to explore further on structure-property relationships and further develop novel structuring/patterning methods.

1.5 Research Aims

The world of supramolecular hydrogels formed by the triggering of LMWGs is large with many different molecular designs, triggers, micro-structuring/patterning strategies researched and reported thus far. In this research thesis, I aim to build further our understanding related to modelling, predicting material properties and micro-structuring of pH-triggered supramolecular hydrogels. Specifically, I try to answer the following questions

1. How can we model pH-triggered supramolecular hydrogel formation using available models? Are there existing models that can explain and any correlations between observed micro-structure and mechanical properties?
2. Is it possible to predict an application-relevant material property of a pH-triggered supramolecular hydrogel?
3. Is it possible to device a simple electrochemical method to micro-pattern pH-triggered supramolecular hydrogels? Current methods as explained in the previous sections work well in formation but it is not possible to detach the produced hydrogels. Also, dimensions are restricted to macro millimetre scale. Is it possible to go sub-millimetre scale?
4. Linked to the above question, is it possible to device a method that allows us to apply method developed to answer question 3 to smaller dimensions such as micro-patterns?

By answering the above-mentioned questions, I intend to contribute in bringing the domain of LMWHs a small step ahead in understanding while positively contributing towards bringing the field closer to applications.

1.6 Outline of the Thesis

This thesis describes the experimental and theoretical work done on a LMWG system that is pH-triggered. The system is used as a model system to be able to demonstrate the methods, strategies developed in this thesis which can potentially be extended to other pH-triggered systems with minor adjustments. The chapter-wise breakdown of content is given below

Chapter 1 provides the background for the scientific work carried out in this thesis.

Chapter 2 describes the approach to understand microstructure of a supramolecular hydrogel network formed by a pH-triggered LMWG based on its rheological properties. Structure-property relationships developed for temperature-triggered LMWGs were employed on a model pH-triggered system to understand if the predicted network fractal dimension could be reconciled with microstructure, as visualized through Confocal Laser Scanning Microscopy (CLSM).

Chapter 3 shows the early attempts of modelling supramolecular gel formation based on random graph theory. The approach, previously employed for polymeric gelation is employed on a model pH-triggered LMWG system by diligently accounting for the participating reactions, experimentally measuring or modelling their rate constants. Using a percolation threshold, the gelation time was predicted by the model which was experimentally verified by following the gelation through rheology.

Chapter 4 describes a new and simple methodology to electrochemically trigger hydrogel formation using Pt-catalysed water-splitting reaction. The method is employed on a simple pH-triggered LMWH system to form sub-mini microgels. The formed microgels are then

detached through the application of electrochemical potential to form microgel patches which are free-floating in solution. This proof of concept is followed by the first attempts at miniaturization of the technique to 100- and 10-micron scales through the use of pre-fabricated Pt microelectrodes to act catalytically active surface templates for hydrogel formation. The templating effect is further explored through the use of different shapes to yield different-shaped microgels.

Chapter 5 builds on the concept proposed in chapter 4 and uses it to develop a new strategy that provides a higher-degree of control over the formation of supramolecular hydrogels and micropatterning them using Pt nanoparticles. Different surface templates (dots, stripes, rings) of Pt nanoparticles are prepared employing electrochemistry at liquid-liquid interfaces. These in turn template the formation of hydrogels which then retain the shape of the underlying micropattern.

References

[1] K. Sano, Y. Ishida, T. Aida, *Angew. Chemie Int* **2018**, *57*, 2532–2543.

[2] M. E. Parente, A. Ochoa Andrade, G. Ares, F. Russo, A. Jiménez-Kairuz, *Int. J. Cosmet. Sci.* **2015**, *37*, 511–518.

[3] E. Pinho, M. Grootveld, G. Soares, M. Henriques, *Crit. Rev. Biotechnol.* **2014**, *34*, 328–337.

[4] M. Mitov, *Foams, Gels, Liquid Crystals, and Other Miracles*, Harvard University Press, Cambridge, MA and London, England, **2012**.

[5] A. Saura-Sanmartin, L. Andreu-Ardil, *Int. J. Mol. Sci.* **2023**, *24*, DOI 10.3390/ijms24054685.

[6] A. Altunbas, D. J. Pochan, *Top. Curr. Chem.* **2012**, *310*, 135–67.

[7] S. Thakur, V. K. Thakur, O. A. Arotiba, in *Hydrogels Recent Adv.* (Eds.: V.K. Thakur, M.K. Thakur), Springer Singapore, Singapore, **2018**, pp. 29–50.

[8] L. Popa, M. V. Ghica, C. E. Dinu-Pîrvu, E.-E. Tudoroiu, in *Hydrogels* (Eds.: L. Popa, M.V. Ghica, C.-E. Dinu-Pîrvu), IntechOpen, Rijeka, **2022**.

[9] S. Mytnyk, **2019**, DOI 10.4233/UUID:E62593A6-5118-4EB7-A638-D4091E6CE6EB.

[10] E. R. Draper, D. J. Adams, *Langmuir* **2019**, acs.langmuir.9b00716.

[11] H. Komatsu, S. Tsukiji, M. Ikeda, I. Hamachi, *Chem. - An Asian J.* **2011**, *6*, 2368–2375.

[12] T. Jungst, W. Smolan, K. Schacht, T. Scheibel, J. Groll, *Chem. Rev.* **2016**, *116*, 1496–1539.

[13] E. Kokkoli, A. Mardilovich, A. Wedekind, E. L. Rexeisen, A. Garg, J. A. Craig, *Soft Matter* **2006**, *2*, 1015–1024.

[14] G. Liu, Q. Yuan, G. Hollett, W. Zhao, Y. Kang, J. Wu, *Polym. Chem.* **2018**, *9*, 3436–3449.

[15] H. Wang, Z. Yang, *Nanoscale* **2012**, *4*, 5259–67.

[16] A. Li, T. Gong, Y. Hou, X. Yang, Y. Guo, *Int. J. Biol. Macromol.* **2020**, *146*, 821–831.

[17] H. Zhang, F. Zhang, R. Yuan, in (Ed.: Y.B.T.-H.B. on N.P. Chen), Elsevier, **2020**, pp. 357–410.

[18] S. Mitura, A. Sionkowska, A. Jaiswal, *J. Mater. Sci. Mater. Med.* **2020**, *31*, 50.

[19] X. Yao, J. Liu, C. Yang, X. Yang, J. Wei, Y. Xia, X. Gong, Z. Suo, *Adv. Mater.* **2019**, *31*, 1903062.

[20] H. Chang, H. Zhao, F. Qu, Z. Yan, N. Liu, M. Lu, Y. Liang, B. Lai, H. Liang, *Sep. Purif. Technol.* **2023**, *308*, 122948.

[21] D. Li, J. Zhang, L. Li, G. Cai, W. Zuo, W. Zhan, P. Wang, Y. Tian, *J. Clean. Prod.* **2022**, *371*, 133650.

[22] V. T. Tran, X. Xu, M. T. I. Mredha, J. Cui, J. J. Vlassak, I. Jeon, *Water Res.* **2018**, *145*, 640–649.

[23] R. Mastrangelo, D. Chelazzi, G. Poggi, E. Fratini, L. P. Buemi, M. L. Petruzzellis, P. Baglioni, *Proc. Natl. Acad. Sci. U. S. A.* **2020**, *117*, 7011–7020.

[24] W. E. Hennink, C. F. van Nostrum, *Adv. Drug Deliv. Rev.* **2012**, *64*, 223–236.

[25] R. A. Wach, H. Mitomo, F. Yoshii, T. Kume, *Macromol. Mater. Eng.* **2002**, *287*, 285–295.

[26] V. Le Sage, V. Lakshminarayanan, E. Mendes, R. Eelkema, J. Van Esch, *Chim. Oggi/Chemistry Today* **2014**, *32*.

[27] T. Xiao, L. Xu, L. Zhou, X.-Q. Sun, C. Lin, L. Wang, *J. Mater. Chem. B* **2019**, *7*, 1526–1540.

[28] S. Strandman, X. X. Zhu, *Gels* **2016**, *2*, DOI 10.3390/gels2020016.

[29] T. Swift, L. Swanson, M. Geoghegan, S. Rimmer, A. V. Dobrynin, M. Rubinstein, F. Liu, M. W. Urban, J. Loiseau, N. Doërr, et al., *Soft Matter* **2016**, *12*, 2542–2549.

[30] E. A. Appel, J. del Barrio, X. J. Loh, O. A. Scherman, *Chem. Soc. Rev.* **2012**, *41*, 6195–6214.

[31] E. Ghanbari, A. Roshanasan, S. J. Picken, J. Van Esch, *From Molecular Assembly to Gelation : What Is Going on behind the Scenes of Supramolecular Gels Formation ? Keywords :*, To Be Submitted, **2023**.

[32] Y. Shao, H. Jia, T. Cao, D. Liu, *Acc. Chem. Res.* **2017**, *50*, 659–668.

[33] J. Maitra, V. K. Shukla, *Am. J. Polym. Sci.* **2014**, *4*, 25–31.

[34] M. L. Pita-López, G. Fletes-Vargas, H. Espinosa-Andrews, R. Rodríguez-Rodríguez, *Eur. Polym. J.* **2021**, *145*, 110176.

[35] B. Jadach, W. Świetlik, A. Froelich, *J. Pharm. Sci.* **2022**, *111*, 1250–1261.

[36] S. M. Mantooth, B. G. Munoz-Robles, M. J. Webber, *Macromol. Biosci.* **2019**, *19*, 1800281.

[37] E. A. Appel, R. A. Forster, M. J. Rowland, O. A. Scherman, *Biomaterials* **2014**, *35*, 9897–9903.

[38] K. Miyamae, M. Nakahata, Y. Takashima, A. Harada, *Angew. Chemie Int. Ed.* **2015**, *54*, 8984–8987.

[39] W. Li, C. Wang, Z. Wang, L. Gou, Y. Zhou, G. Peng, M. Zhu, J. Zhang, R. Li, H. Ni, et al., *ACS Appl. Mater. Interfaces* **2022**, *14*, 25173–25182.

[40] P. H. J. Kouwer, M. Koepf, V. A. A. Le Sage, M. Jaspers, A. M. van Buul, Z. H. Eksteen-Akeroyd, T. Woltinge, E. Schwartz, H. J. Kitto, R. Hoogenboom, et al., *Nature* **2013**, *493*, 651–655.

[41] F. J. Leyva-Jiménez, R. Oliver-Simancas, I. Castangia, A. M. Rodríguez-García, M. E. Alañón, *Food Hydrocoll.* **2023**, *135*, 108124.

[42] A. Luanda, V. Badalamoole, *Int. J. Biol. Macromol.* **2023**, *228*, 794–807.

[43] D. J. Adams, L. M. Mullen, M. Berta, L. Chen, W. J. Frith, *Soft Matter* **2010**, *6*, 1971.

[44] V. Jayawarna, S. M. Richardson, A. R. Hirst, N. W. Hodson, A. Saiani, J. E. Gough, R. V. Ulijn, *Acta Biomater.* **2009**, *5*, 934–943.

[45] J. Boekhoven, M. Koot, T. A. Wezendonk, R. Eelkema, J. H. Van Esch, *J. Am. Chem. Soc.* **2012**, *134*, 12908–12911.

[46] J. Raeburn, G. Pont, L. Chen, Y. Cesbron, R. L?vy, D. J. Adams, *Soft Matter* **2012**, *8*, 1168–1174.

[47] K. J. C. Van Bommel, C. Van Der Pol, I. Muizebelt, A. Friggeri, A. Heeres, A. Meetsma, B. L. Feringa, J. Van Esch, *Angew. Chemie - Int. Ed.* **2004**, *43*, 1663–1667.

[48] Y. E. Shapiro, *Prog. Polym. Sci.* **2011**, *36*, 1184–1253.

[49] K. Brenzinger, *Bchm* **1892**, *16*, 552–588.

[50] R. A. Gortner, W. F. Hoffman, *J. Am. Chem. Soc.* **1921**, *43*, 2199–2202.

[51] C. G. Wolf, E. K. Rideal, *Biochem. J.* **1922**, *16*, 548–555.

[52] F. M. Menger, K. S. Venkatasubban, *J. Org. Chem.* **1978**, *43*, 3413–3414.

[53] F. M. Menger, K. L. Caran, *J. Am. Chem. Soc.* **2000**, *122*, 11679–11691.

[54] F. M. Menger, Y. Yamasaki, K. K. Catlin, T. Nishimi, *Angew. Chemie Int. Ed. English* **1995**, *34*, 585–586.

[55] F. M. Menger, K. L. Caran, *J. Am. Chem. Soc.* **2000**, *122*, 11679–11691.

[56] E. R. Draper, D. J. Adams, *Chem* **2017**, *3*, 390–410.

[57] J. H. Van Esch, *Langmuir* **2009**, *25*, 8392–8394.

[58] K. J. C. Van Bommel, C. Van Der Pol, I. Muizebelt, A. Friggeri, A. Heeres, A. Meetsma, B. L. Feringa, J. Van Esch, *Angew. Chemie - Int. Ed.* **2004**, *43*, 1663–1667.

[59] R. G. Weiss, *J. Am. Chem. Soc.* **2014**, *136*, 7519–7530.

[60] N. Singh, M. Kumar, J. F. Miravet, R. V Ulijn, B. Escuder, *Chem. – A Eur. J.* **2017**, *23*, 981–993.

[61] D. J. Adams, K. Morris, L. Chen, L. C. Serpell, J. Bacsa, G. M. Day, *Soft Matter* **2010**, *6*, 4144.

[62] J. H. Van Esch, B. L. Feringa, *Angew. Chemie - Int. Ed.* **2000**, *39*, 2263–2266.

[63] D. J. Adams, P. D. Topham, *Peptide Conjugate Hydrogelators*, Soft Matter, **2010**.

[64] S. Grigoriou, E. K. Johnson, L. Chen, D. J. Adams, T. D. James, P. J. Cameron, *Soft Matter* **2012**, *8*, 6788.

[65] A. Z. Cardoso, A. E. Alvarez Alvarez, B. N. Cattoz, P. C. Griffiths, S. M. King, W. J. Frith, D. J. Adams, *Faraday Discuss.* **2013**, *166*, 101–116.

[66] A. M. Smith, R. J. Williams, C. Tang, P. Coppo, R. F. Collins, M. L. Turner, A. Saiani, R. V. Ulijn, *Adv. Mater.* **2008**, *20*, 37–41.

[67] M. de Loos, J. H. van Esch, R. M. Kellogg, B. L. Feringa, *Tetrahedron* **2007**, *63*, 7285–7301.

[68] A. Heeres, C. Van Der Pol, M. Stuart, A. Friggeri, B. L. Feringa, J. Van Esch, *J. Am. Chem. Soc.* **2003**, *125*, 14252–14253.

[69] M. De Loos, A. Friggeri, J. Van Esch, R. M. Kellogg, B. L. Feringa, *Cyclohexane Bis-Urea Compounds for the Gelation of Water and Aqueous Solutions*, Org. Biomol. Chem, **2005**.

[70] van Esch JH, B. Feringa, *Angew. Chem. Int. Ed. Engl.* **2000**, *39*, 2263–2266.

[71] K. Yang, Q. Han, B. Chen, Y. Zheng, K. Zhang, Q. Li, J. Wang, *Int. J. Nanomedicine* **2018**, *13*, 2217–2263.

[72] F. M. Menger, Y. Yamasaki, K. K. Catlin, T. Nishimi, *Angew. Chemie Int. Ed. English* **1995**, *34*, 585–586.

[73] L. Li, L. Xie, R. Zheng, R. Sun, *Front. Chem.* **2021**, *9*, DOI 10.3389/fchem.2021.739791.

[74] J. Boekhoven, J. M. Poolman, C. Maity, F. Li, L. Van Der Mee, C. B. Minkenberg, E. Mendes, J. H. Van Esch, R. Eelkema, *Nat. Chem.* **2013**, *5*, 433–437.

[75] P. Ren, J. Li, L. Zhao, A. Wang, M. Wang, J. Li, H. Jian, X. Li, X. Yan, S. Bai, **2020**, DOI 10.1021/acsami.0c03038.

[76] A. Z. Cardoso, A. E. Alvarez Alvarez, B. N. Cattoz, P. C. Griffiths, S. M. King, W. J. Frith, D. J. Adams, *Faraday Discuss.* **2013**, *166*, 101.

[77] R. Li, C. C. Horgan, B. Long, A. L. Rodriguez, L. Mather, C. J. Barrow, D. R. Nisbet, R. J. Williams, *RSC Adv.* **2015**, *5*, 301–307.

[78] C. D. Jones, J. W. Steed, M. A. C. Stuart, J. van der Gucht, M. J. Rosseinsky, J. V. M. Weaver, J. van der Gucht, G. A. G. Cidade, G. D. Stucky, D. E. Morse, et al., *Chem. Soc. Rev.* **2016**, *45*, 6546–6596.

[79] B. Pramanik, S. Ahmed, *Gels* **2022**, *8*, DOI 10.3390/gels8090533.

[80] M. Wallace, A. Z. Cardoso, W. J. Frith, J. A. Iggo, D. J. Adams, *Chem. - A Eur. J.* **2014**, *20*, 16484–16487.

[81] D. J. Cornwell, O. J. Daubney, D. K. Smith, *Stoch. Process. their Appl.* **2016**, *126*, 337–359.

[82] J. Raeburn, B. Alston, J. Kroeger, T. O. McDonald, J. R. Howse, P. J. Cameron, D. J. Adams, S. M. King, R. K. O'Reilly, L. C. Serpell, et al., *Mater. Horiz.* **2014**, *1*, 241–246.

[83] J. Raeburn, A. Zamith Cardoso, D. J. Adams, *Chem. Soc. Rev.* **2013**, *42*, 5143.

[84] J. Raeburn, G. Pont, L. Chen, Y. Cesbron, **2012**, 1168–1174.

[85] B. C. Baker, A. L. Acton, G. C. Stevens, W. Hayes, *Tetrahedron* **2014**, *70*, 8303–8311.

[86] J. Zhong, H. Fu, X. Jia, H. Lou, T. Wan, H. Luo, H. Liu, D. Zhong, X. Luo, *RSC Adv.* **2019**, *9*, 11824–11832.

[87] I. Ziemecka, G. J. M. Koper, A. G. L. Olive, J. H. Van Esch, *Soft Matter* **2013**, *9*, 1556–1561.

[88] D. J. Adams, M. F. Butler, W. J. Frith, M. Kirkland, L. Mullen, P. Sanderson, *Soft Matter* **2009**, *5*, 1856.

[89] C. Tang, A. M. Smith, R. F. Collins, R. V. Ulijn, A. Saiani, *Langmuir* **2009**, *25*, 9447–9453.

[90] C. Tang, R. V. Ulijn, A. Saiani, *Eur. Phys. J. E* **2013**, *36*, DOI 10.1140/epje/i2013-13111-3.

[91] S. Panja, D. J. Adams, *Chem. Soc. Rev.* **2021**, *50*, 5165–5200.

[92] E. R. Draper, L. L. E. Mears, A. M. Castilla, S. M. King, T. O. McDonald, R. Akhtar, D. J. Adams, *RSC Adv.* **2015**, *5*, 95369–95378.

[93] J. M. Poolman, C. Maity, J. Boekhoven, L. Van Der Mee, V. A. A. Le Sage, G. J. M. Groenewold, S. I. Van Kasteren, F. Versluis, J. H. Van Esch, R. Eelkema, *J. Mater. Chem. B* **2016**, *4*, 852–858.

[94] F. Trausel, F. Versluis, C. Maity, J. M. Poolman, M. Lovrak, J. H. Van Esch, R. Eelkema, *Acc. Chem. Res.* **2016**, *49*, 1440–1447.

[95] B. Escuder, in *Supramol. Catal.*, **2022**, pp. 81–92.

[96] W. Fang, Y. Zhang, J. Wu, C. Liu, H. Zhu, T. Tu, *Chem. - An Asian J.* **2018**, *13*, 712–729.

[97] J. Raeburn, T. O. McDonald, D. J. Adams, *Chem. Commun.* **2012**, *48*, 9355.

[98] C. C. Piras, D. K. Smith, *Chem. – A Eur. J.* **2019**, *25*, 11318–11326.

[99] X. Yang, G. Zhang, D. Zhang, *Stimuli Responsive Gels Based on Low Molecular Weight Gelators*, J. Mater. Chem, **2012**.

[100] K. Murata, M. Aoki, T. Suzuki, T. Harada, H. Kawabata, T. Komori, F. Ofaseto, K. Ueda, S. Shinkai, *J. Am. Chem. Soc.* **1994**, *116*, 6664–6676.

[101] J. K. Sahoo, S. K. M. Nalluri, N. Javid, H. Webb, R. V Ulijn, *Chem. Commun.* **2014**, *50*, 5462–5464.

[102] H. Svobodová, V. Noponen, E. Kolehmainen, E. Sievänen, *RSC Adv.* **2012**, *2*, 4985–5007.

[103] Z. Qiu, H. Yu, J. Li, Y. Wang, Y. Zhang, *Chem. Commun.* **2009**, 3342–3344.

[104] S. H. Kim, Y. Sun, J. A. Kaplan, M. W. Grinstaff, J. R. Parquette, *New J. Chem.* **2015**, *39*, 3225–3228.

[105] E. R. Draper, T. O. Mcdonald, D. J. Adams, **2015**, 12827–12830.

[106] J. Raeburn, T. O. McDonald, D. J. Adams, *Chem. Commun.* **2012**, *48*, 9355–9357.

[107] C. Maity, W. E. Hendriksen, J. H. Van Esch, R. Eelkema, *Angew. Chemie - Int. Ed.* **2015**, *54*, 998–1001.

[108] J. Raeburn, A. Z. Cardoso, D. J. Adams, *Chem. Soc. Rev.* **2013**, *42*, 5143–5156.

[109] X. Liu, L. Zhao, F. Liu, D. Astruc, H. Gu, *Coord. Chem. Rev.* **2020**, *419*, DOI 10.1016/j.ccr.2020.213406.

[110] Z. Sun, Z. Li, Y. He, R. Shen, L. Deng, M. Yang, Y. Liang, Y. Zhang, *J. Am. Chem. Soc.* **2013**, *135*, 13379–13386.

[111] X. Yu, L. Chen, M. Zhang, T. Yi, *Low-Molecular-Mass Gels Responding to Ultrasound and Mechanical Stress: Towards Self-Healing Materials*, Chem. Soc. Rev, **2014**.

[112] J. Wu, Q. Tian, H. Hu, Q. Xia, Y. Zou, F. Li, T. Yi, C. Huang, *Chem. Commun.* **2009**, 4100–4102.

[113] V. Nele, C. E. Schutt, J. P. Wojciechowski, W. Kit-Anan, J. J. Doutch, J. P. K. Armstrong, M. M. Stevens, *Adv. Mater.* **2020**, *32*, 1905914.

[114] L. Ling, L. Zhu, Y. Li, C. Liu, L. Cheng, *Front. Bioeng. Biotechnol.* **2021**, *9*, DOI 10.3389/fbioe.2021.703582.

[115] E. K. Johnson, D. J. Adams, P. J. Cameron, *J. Mater. Chem.* **2011**, *21*, 2024–2027.

[116] C. Patterson, B. Dietrich, C. Wilson, A. R. Mount, D. J. Adams, *Soft Matter* **2022**, *18*, 1064–1070.

[117] Z. Sun, Q. Huang, T. He, Z. Li, Y. Zhang, L. Yi, *ChemPhysChem* **2014**, *15*, 2421–2430.

[118] K. J. C. van Bommel, M. C. a Stuart, B. L. Feringa, J. van Esch, *Org. Biomol. Chem.* **2005**, *3*, 2917–20.

[119] M. Lovrak, Strategies Towards Soft Functional Supramolecular Materials, Delft University of Technology, **2018**.

[120] S. Mytnyk, A. G. L. Olive, F. Versluis, J. M. Poolman, E. Mendes, R. Eelkema, J. H. van

Esch, *Angew. Chemie - Int. Ed.* **2017**, *56*, 14923–14927.

[121] J. Poolman, Modular Molecular Gels: Control over Design, Formation and Properties, Delft University of Technology, **2017**.

[122] **2017**, DOI 10.4233/uuid.

[123] M. Lovrak, W. E. J. Hendriksen, C. Maity, S. Mytnyk, V. van Steijn, R. Eelkema, J. H. van Esch, *Nat. Commun.* **2017**, *8*, 15317.

[124] Y. Liu, Y. Cheng, H.-C. Wu, E. Kim, R. V. Ulijn, G. W. Rubloff, W. E. Bentley, G. F. Payne, *Langmuir* **2011**, *27*, 7380–7384.

[125] A. G. L. Olive, N. H. Abdullah, I. Ziemecka, E. Mendes, R. Eelkema, J. H. Van Esch, *Angew. Chemie - Int. Ed.* **2014**, *53*, 4132–4136.

[126] Y. Wang, S. Oldenhof, F. Versluis, M. Shah, K. Zhang, V. van Steijn, X. Guo, R. Eelkema, J. H. van Esch, *Small* **2019**, 1804154.

[127] A. R. Hirst, B. Escuder, J. F. Miravet, D. K. Smith, *Angew. Chemie Int. Ed.* **2008**, *47*, 8002–8018.

[128] A. Z. Cardoso, A. E. Alvarez Alvarez, B. N. Cattoz, P. C. Griffiths, S. M. King, W. J. Frith, D. J. Adams, *Faraday Discuss.* **2013**, *166*, 101–116.

[129] G. Ben Messaoud, P. Le Griel, D. Hermida-Merino, S. L. K. W. Roelants, W. Soetaert, C. V. Stevens, N. Baccile, *Chem. Mater.* **2019**, *31*, 4817–4830.

[130] R. E. Ginesi, N. R. Murray, R. M. Dalgliesh, J. Doutch, E. R. Draper, *Chem. – A Eur. J.* **2023**, *29*, e202301042.

[131] F. Versluis, D. M. van Elsland, S. Mytnyk, D. L. Perrier, F. Trausel, J. M. Poolman, C. Maity, V. A. A. le Sage, S. I. van Kasteren, J. H. van Esch, et al., *J. Am. Chem. Soc.* **2016**, *138*, 8670–8673.

[132] Y. Wang, F. Versluis, S. Oldenhof, V. Lakshminarayanan, K. Zhang, Y. Wang, J. Wang, R. Eelkema, X. Guo, J. H. van Esch, *Adv. Mater.* **2018**, *30*, 1–7.

[133] J. P. Wojciechowski, A. D. Martin, P. Thordarson, *J. Am. Chem. Soc.* **2018**, *140*, 2869–2874.

[134] S. Bai, H. Wang, G. Gu, Y. Gou, X. Zhou, S. Yu, Q. Wang, X. Guo, Y. Wang, *Chem. Eng. J.* **2023**, *475*, 146125.

[135] J. Boekhoven, W. E. Hendriksen, G. J. M. Koper, R. Eelkema, J. H. Van Esch, *Science (80-.).* **2015**, *349*, 1075–1079.

[136] D. J. Cornwell, O. J. Daubney, D. K. Smith, P. M. Gels, *J. Am* **2015**, *137*, 15486–15492.

[137] M. M. Smith, D. K. Smith, *Soft Matter* **2011**, *7*, 4856–4860.

[138] S. Panja, B. Dietrich, A. J. Smith, A. Seddon, D. J. Adams, *ChemSystemsChem* **2022**, *4*, e202200008.

[139] N. Singh, A. Lopez-Acosta, G. J. M. Formon, T. M. Hermans, *J. Am. Chem. Soc.* **2022**, *144*, 410–415.

Chapter 2

Gelation kinetics-structure analysis of pH-triggered low molecular weight hydrogelators

---

Abstract: Properties such as shear modulus, gelation time, structure of supramolecular hydrogels are strongly dependent on self-assembly, gelation triggering mechanism and processes used to form the gel. In our work we extend reported rheology analysis methodologies to pH-triggered supramolecular gels to understand structural insight using a model system based on N-N' Dibenzoyl-L-Cystine pH-triggered hydrogelator and Glucono-δ-Lactone as the trigger. We observed that Avrami growth model when applied to time-sweep rheological data of gels formed at lower trigger concentrations provide estimates of fractal dimension which agree well compared with visualization of the microstructure as seen via Confocal Laser Scanning Microscopy, for a range of gelator concentrations.

This chapter has been published as V. Lakshminarayanan, C. Chockalingam, E. Mendes, J. H. van Esch, *ChemPhysChem* **2021**, DOI 10.1002/CPHC.202100276.

2.1 Introduction

Supramolecular gels formed by the self-assembly of low molecular weight hydrogelators (LMWGs) are an important class of supramolecular materials. With applications ranging from cell culture scaffolds, drug delivery systems, they are emerging as an alternative to their polymer counterparts. [1,2] A number of triggering methods exist to initiate the self-assembly of LMWGs namely temperature, pH, light, sound, chemical fuels, enzymes etc.[2–7] Each of these triggering methods enable to achieve a certain of degree of control and opens up the possibilities to create a different application of supramolecular gels using them. In the context of applications, in order to optimize formulations, it is imperative that the triggering method and processing of LMWGs be related to the material properties that are obtained in gels. Thus, creating a link between gel processing and resulting characteristics is important. Controlled gel processing by temperature programming, solvent switch and addition of additives have been demonstrated to impact structure and properties of organogels. [8–10] Later reports have suggested and encouraged the notion that such ideas may be valid for hydrogels as well. Control over gelation conditions using glucono- δ -lactone (GDL) paved the way to a number of studies investigating the effect of kinetics on mechanical properties of Fmoc-dipeptide hydrogels. [11,12]. Depending on the variant of the gelator chosen, different properties in terms of shear modulus were obtained for the same triggering method. Due to the impact of processing conditions on gel properties, it is important to include gel triggering method in structure-property investigation. Temperature-triggered organogelators have been well studied in this regard and clear structure-property relationships have been developed. [8 -10] However, it is not the case for hydrogelators. In the recent years, considerable attention has been given to pH-triggered supramolecular hydrogels obtained from e.g., dipeptide hydrogelators, sophorolipids due to their versatility. [3,4,28] In this work we investigate the effect of kinetics of pH triggering on the obtained gel properties and microstructure. Already developed structure-property relationships from temperature triggering of organogelators were used to understand if such an approach can be valid for hydrogelators as well. For the sake of simplicity, we used

an off-the-shelf dipeptide gelator (Dibenzoyl-L-Cystine (DBC)) as an acid-triggered hydrogelator, in combination with GDL. [11,13,14]

2.2 Results and Discussion

First, the pH triggering system by GDL hydrolysis was studied to ensure that it could serve as a reliable method for the kinetic studies of gelation. The kinetics of pH change of a 5mM solution of Na_2DBC observed after addition various amounts of GDL is shown in Figure 1. Upon addition of GDL, pH decreases rapidly within the first minute followed by a more gradual change over the course of tens to hundreds of minutes. After a certain time (ca. 100 min), the pH does not change significantly. Increasing the amount of GDL added resulted in a faster decrease in pH and a lower final pH value (measured after 8 hours) (Figure 1A.). We observed that changing the gelator concentration had a minor effect on the observed final pH values as compared to GDL concentrations. Figure 1B shows the average final pH values with errors associated with different gelator concentrations explored in this study (2-20mM) for each given concentration of GDL.

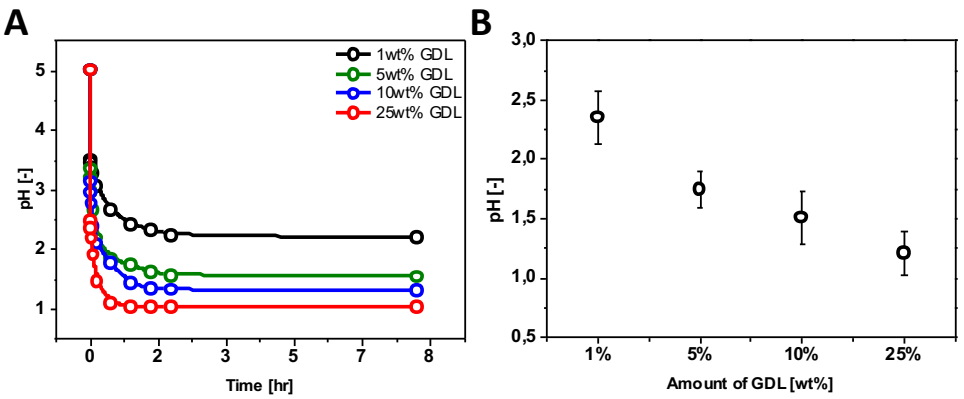

Figure 1. GDL dependence of pH change for the case of 5mM Na2DBC [A]; Final pH values measured after 8 hours from addition of 1wt.% (57 mM), 5wt.% (295 mM), 10wt.% (624 mM) and 25 wt.% (1871 mM) of GDL. The corresponding [GDL]/[Gelator] molar ratios are 11, 59, 125 and 374 respectively, Error bars indicate final pH variation (standard deviation, N = 3) at 5mM gelator concentration.

The data for 2, 10 and 20 mM Na2DBC can be found in Figures S1-S3 of the supplementary information. The variation in end pH values with DBC and GDL concentration is presented in Table S1. The variation in the pH values with gelator concentration can be qualitatively explained by considering the buffer formation by the protonation of DBC salt (Na2DBC). With increase in initial DBC salt concentration, the buffer capacity increases slightly for a given amount of GDL. However, for a fixed amount of DBC salt, increasing the GDL concentration enables the system to overcome the buffer capacity of the DBC buffer resulting in the lowering of the end pH. We want to highlight to the reader that while GDL is a useful tool to control kinetics, it could be challenging in deploying it as a quantitative indicator. To understand if [GDL]/[DBC salt] could be used a quantitative indicator we plotted the end pH at various molar ratios (see Figure S26 in Appendix). The results showed scattering of values leaving us to omit the use of molar ratios as a way of representing the data. We hence continued to use the absolute concentrations to represent data in this work. We next investigated the gelation of DBC in the presence of GDL. It has been reported for DBC that gelation occurs when pH drops below the pKa. [16,17] The gelation occurs via formation of fibres through self-assembly of the gelators. Since the gel formation in our system is coupled to the kinetics of the pH change, a technique that can track a material property that varies as a function of time is required. The dynamic storage and loss moduli (G' & G'') are material properties that are commonly reported for supramolecular gels and rheological techniques are commonly reported to track kinetics of gel formation.[15] Hence, we followed the kinetics of gelation of GDL triggered DBC gels under the rheometer. The results obtained for 5 mM of gelator is given in Figure 2.

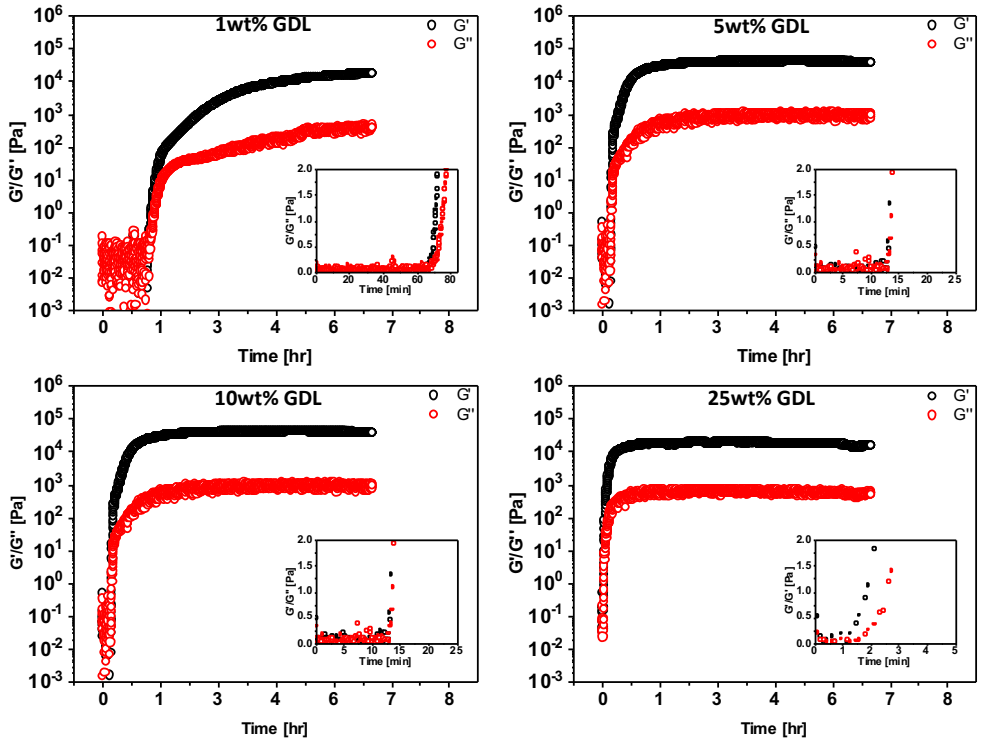

Figure 2. Time evolution of storage modulus (G') and loss modulus (G'') upon addition of different amounts of GDL to 5mM Na_2DBC solution (1wt.% (57 mM), 5wt.% (295 mM), 10wt.% (624 mM) and 25 wt.% (1871 mM) of GDL. The corresponding [GDL]/[Gelator] molar ratios are 11, 59, 125 and 374 respectively). The insets show the early stages of gelation that are used in determining the gel point.

The data for 2,10 and 20 mM gelator can be found in Figures S4-S6 of the supplementary information. As it can be observed in Figure 2 for low GDL concentrations, the observed G' does not start increasing immediately after the addition of GDL. There is a time delay of (lag phase) after which gelation begins and reaches a plateau after sometime (ca. 30min). This is similar to earlier reported work on gelation of LMWG with GDL in the case of Fmoc-dipeptide gelators.[18] The hydrolysis of GDL produces acid that protonates the carboxylate ions of DBC. The protonated DBC (H_2DBC) then proceeds to form a gel via self-assembly. The hydrogen bonding between carboxylic acid groups in the gelator has been found to be crucial in the fibre network formation in this class of gelators.[19] With increasing amounts of added GDL,

the lag phase reduces in time, indicating that self-assembly of gelator molecules happens earlier. At very high concentrations of GDL, pH drops below the pKa (3.58) within the first 30 seconds, enough to initiate the formation of fibres.[17] Gelation is said to have occurred when a fibrous network consisting of entanglements or crosslinks has been formed that begins to offer resistance to the applied shear. Experimentally, this is defined as the point when G' = G''. Recent works on LMWGs have suggested that this definition is only approximate and not binding.[18] For gelation of non-crystalline solids, an accurate method for predicting tgel has been suggested by plotting (s/<tanδ>) vs. time (s – standard deviation in tanδ, tanδ = G''/G') and choosing the value of minimum of this curve.[20] In our efforts to use this method on our data, we observed that the tgel values determined by this method were much larger than experimentally observed. We hence continued with our first choice, and we take the time for gelation (tgel), as the point where G' crosses G''. The time-sweep curves for the remaining gel concentrations and tanδ plots can be found in the supplementary section (see Figures S21 – S24). For a given concentration of gelator, increasing the amount of GDL leads to a decrease in the observed gel point (see Figure 3).

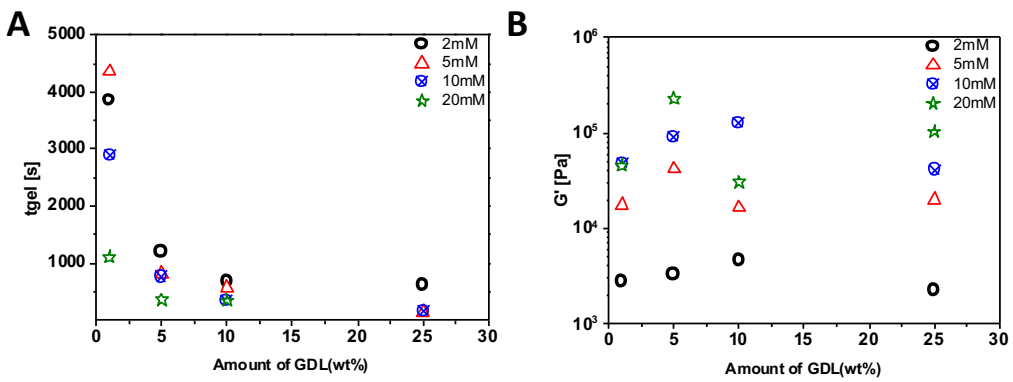

Figure 3. Plots of t_{gel} and plateau modulus ($G'(\infty)$) as function of concentration of GDL (1wt.% (57 mM), 5wt.% (295 mM), 10wt.% (624 mM) and 25 wt.% (1871 mM) of GDL) at various gelator concentrations. Expanded version for Figure 3B available in ESI as Figure S25.

The same trend is observed for the plateau modulus. Faster hydrolysis seems to result in weaker gels, an observation that also has been reported for GDL triggered Fmoc-dipeptide

hydrogels.[21] However, the role of kinetics was not considered to as important as compared to end pH in the case of Fmoc-dipeptide hydrogels.[30] From our observations, there seems to be an optimum (around 5-10% GDL) depending on the gelator concentration where G' achieves a maximum before decreasing further. This is likely linked to a change in the type of network being formed in the gel. In our efforts to investigate this, we took inspiration from earlier reported work on temperature-triggered organogelators whose structure-property relationships have been studied in detail over many years. [10,22,23]. Temperature triggered formation of fibrous organogels from N-lauroyl-L-glutamic acid di-n-butylamide (GP-1) has been investigated by X.Y. Liu and co-workers to develop rheology-based models and analysis in terms of the fractal dimensions of their networks.[22] Their model was based on the Avrami model to describe nucleation and growth of bulk crystals (Eq. 1)

$$\ln[1 - X_{cr}] = -k\left(t - t_{gel}\right)^{D_{f,A}} \quad (1)$$

In equation (1), k is constant, X_{cr} is the crystallinity of the system which is equal to the ratio of volume fraction of crystal material at time t to the volume fraction as $t \to \infty$, and t_{gel} is the time for gelation or gel point as determined by rheology. The authors correlated crystallinity and viscosity by using Einstein's relation to end up with the following relation [23,24]

$$X_{cr}(t) = \frac{\varphi(t)}{\varphi(\infty)} = \frac{\eta_{sp}(t)}{\eta_{sp}(\infty)} = \frac{\eta^*(t) - \eta_0}{\eta^*(\infty) - \eta_0} \quad (2)$$

In (2), $\varphi(t)$ and $\varphi(\infty)$ are the volume fractions at time t and $t \to \infty$ respectively, and $\eta_{sp}(t)$ and $\eta_{sp}(\infty)$ are the corresponding specific viscosities. The complex viscosities $\eta^*(t)$ and η_0 of the system and the solvent, respectively, are related to the complex moduli, $G*$ of the system to give the following final relation

$$X_{cr}(t) = \frac{\varphi(t)}{\varphi(\infty)} = \frac{\eta_{sp}(t)}{\eta_{sp}(\infty)} = \frac{\eta^*(t) - \eta_0}{\eta^*(\infty) - \eta_0} = \frac{G*(t) - G*_0}{G*(\infty) - G*_0} \quad (3)$$

By using (3), the time dependent values of $X_{cr}(t)$ can be obtained from the time evolution of the complex moduli $G*(t)$, which can now be analysed with (1) by plotting

$ln\{-ln[1-X_{cr}(t)]\}$ vs. $ln[t-t_{gel}]\}$ to yield the fractal dimension D_f. For one-dimensional or rod-like growth, two-dimensional or plate-like growth, and 3-dimensional spherical growth, D_f=1,2,3 respectively. The value of D_f indicates the fractal dimension, an indication of self-similarity in the network. By comparing with results from static light scattering data, it has been shown that their method gave very good estimates for the dimensionality of their system. [3,25] In later accounts, another method based on the Dickinson model developed by Terech and co-workers was used instead of the above Avrami relation. [26,27] The reason cited was that the Avrami exponent depends strongly on both crystal growth dimensionality and nucleation mechanism. Furthermore, they introduced a scaling argument into the Dickinson model to create an Extended-Dickinson Model that provided good estimates for dimensionality of the structures when compared against optical microscopy images. The same model was later used to study the effect on confinement on molecular gelation of GP-1 at higher concentrations (3-7 wt.%).[27] In our work, the maximum concentration of gelator was 20mM (ca. 1wt.%). Hence the original Dickinson model which is valid for semi-dilute systems maybe be used to check if it might be applicable. In this model, instead of crystal volume fraction, a gel-volume fraction as defined in previous work is used. [26,27] This volume fraction is directly related to the storage modulus instead of the complex modulus. The final expression is given by equation S1 in the supplementary information (refer Appendix). Therefore, a plot of gel volume fraction vs. the time during the growth phase can be used to extract the exponent from which the fractal dimension can be calculated. From the analysis of rheology data based on the models, we observed that the obtained values are strongly dependent on the region chosen for the fitting process. The regions just after $t > t_{gel}$ have been chosen in the previously reported work. [22,23,27] Since the plots need $t - t_{gel}$ (see Figure 4) the estimates depend on the value of t_{gel}.

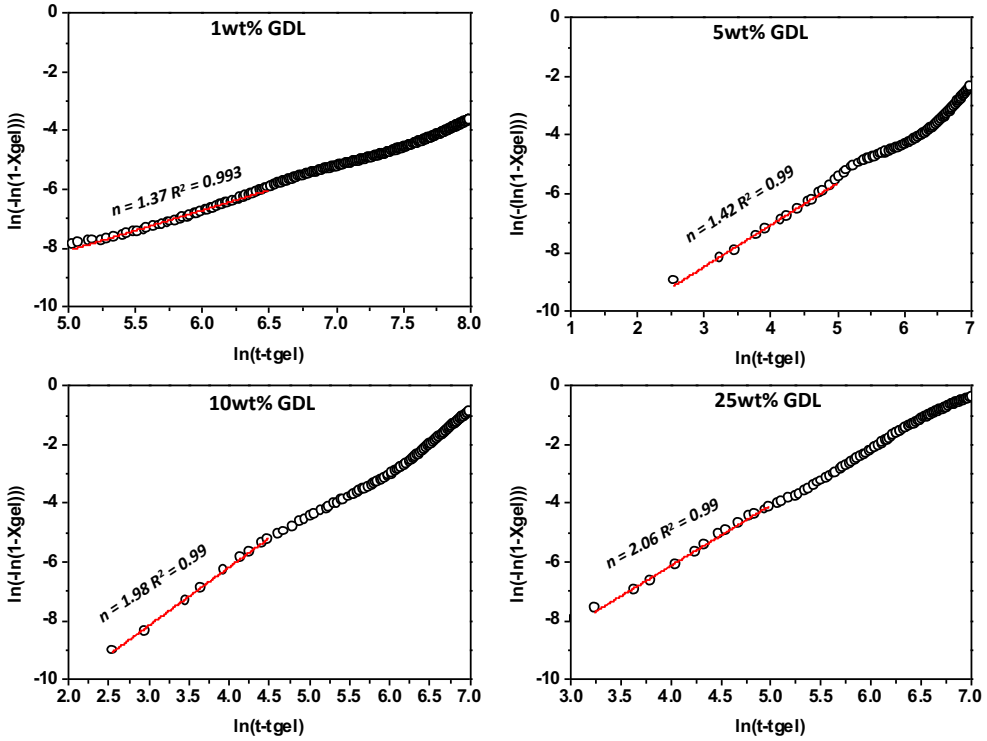

Figure 4. Model fits based on Avrami model for the case of 5mM gelator concentration and different amounts of GDL (1wt.% (57 mM), 5wt.% (295 mM), 10wt.% (624 mM) and 25 wt.% (1871 mM) of GDL). The corresponding [GDL]/[Gelator] molar ratios are 11, 59, 125 and 374 respectively

As mentioned in the methods section, a time delay between vortexing and eventually starting the measurement was observed. This means that the true gelation time is somewhere in the vicinity of the chosen gelation time, that is, early growth stages. We observed that the exponent values obtained from both models do not differ significantly (see Figures 4, S7, S8, S9, S10). However, this leads to different fractal dimensions because the two models have different relationships between exponent and fractal dimension. In the Avrami model exponent 'n' of Figure 4 is directly equal to the fractal dimension $D_{f,A}$ and we see that it increases as the concentration of GDL increases. In the case of the Dickinson model, we observe the opposite trend with $D_{f,D}$ decreasing as the GDL amount is increased (see Figures 5, S11, S12, S13, S14 and Table S3) as also shown from equation S1. This

discrepancy arises from the reciprocal relationship which exists in the Dickinson model. We hence used the Avrami model predictions for further investigation. To reconcile the model predictions visually, we performed confocal microscopy (CLSM) experiments as described in the experimental section and the results are shown in Figure 5.

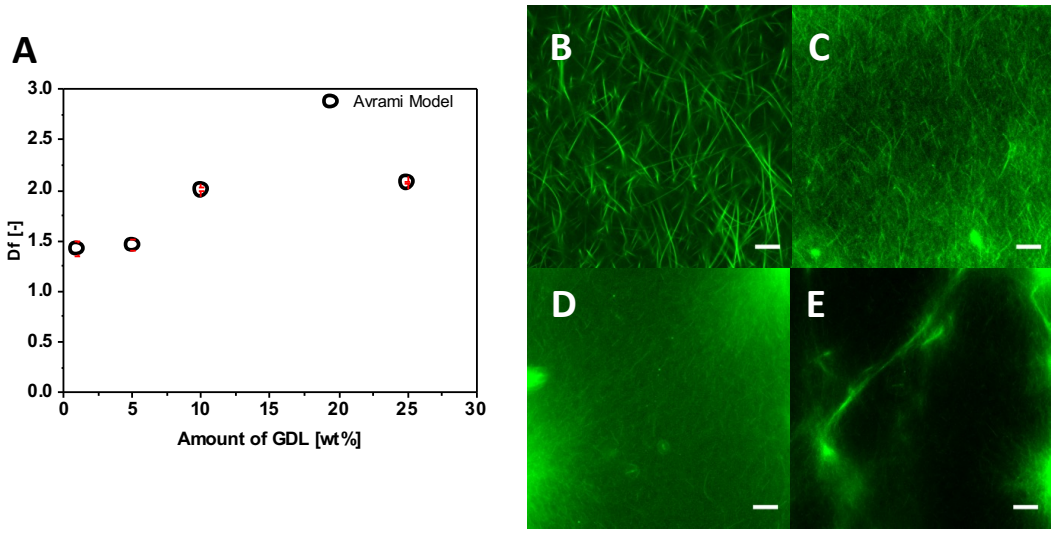

Figure 5. Model predictions for $D_{f,A}$ [A]; False-colour CLSM micrographs showing differences in morphology in hydrogels formed from 5mM of gelator upon addition of 1wt.% (57 mM) [B], 5wt.% (295 mM) [C],10wt.% (624 mM) [D] and 25wt.% (1871 mM) [E] of GDL. The corresponding [GDL]/[Gelator] molar ratios are 11, 59, 125 and 374 respectively. Scale bar is 20µm.

The CLSM micrographs exhibit differences in the morphology of hydrogels (Figure 5, B-E) based on the concentration of GDL. At lower concentrations of GDL, entangled fibrous networks are observed which becomes more inhomogenously distributed at higher concentrations. Similar observations were made with Fmoc-dipeptide hydrogels that were produced by acidification using HCl.[14] A sharp decrease in pH is associated with this microstructure feature. In our system, higher concentrations of GDL cause a rapid reduction of pH which can lead to such microstructural inhomogeneities. Previous work on non-peptide low molecular weight gelators has shown that sharp decrease in pH lead to fibrillar gels with side-branches and spherulites.[28] From the model predictions we see in an increase in $D_{f,A}$ as the concentration of GDL increases. Figure 5A illustrates this for the case of 5mM

of DBC gelator. Similar observations are seen for the case of 2mM, 10mM and 20mM gelators as the concentration of GDL trigger increases (Figures S12A, S13A and S14A in Appendix). From work on pH-triggered self-assembly of sophorolipids, we can see that at high acidification rates, the tendency to side-branch and form spherulites increases leading to weaker gels that are loosely connected. DBC is also known to form spherulites in water when gels produced by cooling down a hot solution were allowed to stand over a long period of time.[29] From confocal micrographs we do see observe the presence of loosely connected spherulites at higher concentrations of GDL (Figures 5D, 5E, S12D, S12E, S13D, S13E, S14C). Correspondingly we do observe an increase in D_f from ca. 1.2 (at 1% GDL) to 1.5 - 3 (at 25% GDL) (see Table S2 in Appendix). From CLSM data, it can be seen that a faster decrease in pH produces more in-homogenous loosely connected structures as opposed to thinner fibres at around 5% GDL. It is known that thinner, homogenously distributed fibres provide more strength to the network.[29] This could explain the apparent increase in storage modulus seen during the rheological characterization. At lower concentrations of GDL, Avrami model predictions indicate that a nearly one dimensional (1D) fibrous structure exists which corroborates well with the CLSM micrographs. With increasing gelator concentration, the Avrami model predicted fractal dimension increases as the driving force (acidification rate) increases. Avrami model considers the network formation to be similar to the process of crystallization which is applicable to DBC since they are known to form crystals in aqueous environments.[31] The Dickinson model developed for weak interacting colloidal aggregation does not provide estimates of fractal dimension that corroborate well with experimental observations made using confocal microscopy. The model assumes that particles and aggregates can be treated as spheres.[32] The aggregates behaving like hard spheres form space-filling structures in a diffusion or reaction limited aggregation mechanisms. The fractal dimension relates to the gelation time with near-infinite gelation times for compact structures (D_f =3). In our systems gelation time is dependent on gelator concentration and trigger concentration. Furthermore, Dickison model does not take any side-branching or interpenetration into account. For these reasons, it is not considered an appropriate model to understand structure-property relationships in pH-triggered LMWG systems despite its

moderate success in organogelator systems. The Avrami model predicted fractal dimensions are consistent with previously reported values for organogelators and chemically triggered systems. [15,22,23] However the transition between nearly 1-D fibres at low trigger concentrations (1% GDL) to loosely connected spherulites at higher trigger concentration (10%,25% GDL) seems to indicate that there is a regime where tendency to side-branch begins to increase. We wonder if there may be a threshold concentration of gelator and trigger which could exist in these systems. However, based on the experimentally studied concentrations, we are unable to draw definitive conclusions at this stage.

2.3 Conclusions

This work shows that mechanical properties of low molecular weight gelators are dependent on kinetics of GDL hydrolysis, an observation that differs from previous work on Fmoc-di peptide gelators and more in line with sophorolipids. [28,30] Rheology analysis using Avrami based kinetic-fibre branching models developed for organogelators give a good indication of fractal dimensions for pH-triggered LMWGs such as DBC when acidified using a trigger such as GDL. Through careful experimental design with smaller steps in trigger and gelator concentration, it would be possible to explore the transition between 1-D fibres to networks with side-branches and spherulites. This would enable us to precisely control the morphology of gel networks which could be valuable for applications in cell culturing, tissue engineering where morphology of scaffolds can have an impact on cell proliferation and differentiation.[1]

2.4 Experimental Section

2.4.1 Materials and Methods

2.4.1.1 Safety & Hazards

This work was carried out in a Chemistry lab with personal protective equipment such as lab coat and safety eyewear. Powdered solid materials were handled with care to avoid accidental inhalation and nasal irritation. Exercise caution while handling chemicals and handle them as per the safety protocols of your laboratory.

2.4.1.2 Gelator and pH triggering agents

N-N' Dibenzoyl-L-cystine (98%), Nile red (9-(Diethylamino)-5H-benzo[a]phenoxazin-5-one), and Sodium Hydroxide were purchased from Sigma-Aldrich and used without further purification. Glucono-δ-lactone (99%) was purchased from Alfa Aesar and used without further purification.

2.4.1.3 Production of hydrogels

Neutralized DBC salt (Na2DBC) stock solutions were first prepared fresh by preparing a solution from a weighted amount of the free acid gelator (H2DBC) and the corresponding volume of a 1M NaOH stock solution containing two equivalents of base. The mixture was vortexed to ensure complete dissolution of the gelator. The pH was then measured to and found to be around 4 – 5. Variance across batches was tested and found to be small (4.81 ± 0.68). To prepare the hydrogels, measured quantities of GDL (in the form of a powder) were added to Na2DBC solutions and vortexed briefly and allowed to set. The dissolution of GDL is faster than its hydrolysis and this results in a gradual decrease in pH which eventually leads to gel formation.14

2.4.1.4 pH measurements

All pH measurements were carried out using a Metrohm 744 pH meter at 25◦C after calibrating using standard pH buffers at pH 1.61, 4 and 7.

2.4.1.5 Rheological Characterisation

Oscillatory rheology measurements were performed on an AR-G2 strain-controlled rheometer (TA instruments) using a 40mm stainless steel plate-plate geometry. The temperature was maintained at 25 ± 0.2◦C. A known amount of GDL was put in a 2mL vial with an easy open cap. Measured quantity of DBC salt solution was aspirated in a 1000 µL micropipette and added to the vial. After a quick vortexing, the solution was casted on to the bottom plate of the rheometer. A short time delay of 6 seconds was observed between vortexing, to casting and lowering of the top plate to the bottom plate. A solvent trap filled

with water or hexadecane was used to prevent drying of the formed hydrogels. Time evolution of storage (G') and loss modulus (G'') was followed at 1 Hz and 0.05% strain. This is a commonly used setting for measuring gels formed from LMWGs.15 To be thorough, the LVER (Linear Viscoelastic region) was confirmed at these settings via frequency and strain sweeps (Figures S15 - S18 in Appendix). To allow comparison across different samples, a constant gap of about 770 ± 10 μm was maintained. Rheology measurements which were used to estimate fractal dimension were carried out in triplicate.

2.4.1.6 Confocal Laser Scanning Microscopy (CLSM)

Morphology visualization of hydrogels was performed using a Zeiss LSM 710 confocal laser. Nile red was used as the staining agent to track DBC gel fibres.16 The hydrogel samples were prepared by mixing 40 μL of 5mM Nile Red in 95% pure ethanol to a weighed amount of GDL along with a predetermined volume of Na2DBC solution and MilliQ water as required for a certain hydrogel concentration in a 1ml vial. The final concentration of Nile red in this solution was 25 μM. The solution was then vortexed for 30 seconds to ensure complete dissolution of GDL. 80 μL of this solution was pipetted out and placed in a chamber made of glass slide (2 x 2 cm) and an inert rubber gasket which was again sealed with a second glass side. The slides were mounted on the stage of the microscope. CLSM micrographs of the hydrogels were obtained using a laser beam at 514 nm and oil immersion 40X Zeiss objective.

References

[1] V. Le Sage, V. Lakshminarayanan, E. Mendes, R. Eelkema, J. Van Esch, *Chim. Oggi/Chemistry Today* **2014**, *32*.

[2] A. Friggeri, B. L. Feringa, J. van Esch, *J. Control. Release* **2004**, *97*, 241–248.

[3] E. R. Draper, L. L. E. Mears, A. M. Castilla, S. M. King, T. O. McDonald, R. Akhtar, D. J. Adams, *RSC Adv.* **2015**, 95369–95378.

[4] E. R. Draper, E. G. B. Eden, T. O. McDonald, D. J. Adams, *Nat. Chem.* **2015**, *7*, 848–852.

[5] G. Cravotto, P. Cintas, *Chem. Soc. Rev.* **2009**, *38*, 2684.

[6] J. Boekhoven, A. M. Brizard, K. N. K. Kowlgi, G. J. M. Koper, R. Eelkema, J. H. van Esch, *Angew. Chemie* **2010**, *122*, 4935–4938.

[7] D. J. Cornwell, D. K. Smith, *Mater. Horizons* **2015**, *2*, 279–293.

[8] J.-L. Li, R.-Y. Wang, X.-Y. Liu, H.-H. Pan, *J. Phys. Chem. B* **2009**, *113*, 5011–5015.

[9] J. L. Li, X. Y. Liu, *Adv. Funct. Mater.* **2010**, *20*, 3196–3216.

[10] J. L. Li, X. Y. Liu, C. S. Strom, J. Y. Xiong, *Adv. Mater.* **2006**, *18*, 2574–2578.

[11] E. R. Draper, L. L. E. Mears, A. M. Castilla, S. M. King, T. O. McDonald, R. Akhtar, D. J. Adams, *RSC Adv.* **2015**, *5*, 95369–95378.

[12] D. J. Adams, M. F. Butler, W. J. Frith, M. Kirkland, L. Mullen, P. Sanderson, *Soft Matter* **2009**, *5*, 1856.

[13] F. M. Menger, K. L. Caran, *J. Am. Chem. Soc.* **2000**, *122*, 11679–11691.

[14] D. J. Adams, M. F. Butler, W. J. Frith, M. Kirkland, L. Mullen, P. Sanderson, *Soft Matter* **2009**, *5*, 1856.

[15] J. Boekhoven, J. M. Poolman, C. Maity, F. Li, L. van der Mee, C. B. Minkenberg, E. Mendes, J. H. van Esch, R. Eelkema, *Nat. Chem.***2013**, *5*, 433–7.

[16] J. Boekhoven, W. E. Hendriksen, G. J. M. Koper, R. Eelkema, J. H. van Esch, *Science (80-.).* **2015**, *349*.

[17] J. P. Wojciechowski, A. D. Martin, P. Thordarson, *J. Am. Chem. Soc.* **2018**, *140*, 2869–2874.

[18] A. Z. Cardoso, A. E. Alvarez Alvarez, B. N. Cattoz, P. C. Griffiths, S. M. King, W. J. Frith, D. J. Adams, *Faraday Discuss.* **2013**, *166*, 101.

[19] F. M. Menger, Y. Yamasaki, K. K. Catlin, T. Nishimi, *Angew. Chemie Int. Ed. English* **1995**, *34*, 585–586.

[20] E. Rudé Payró, J. Llorens Llacuna, *J. Non. Cryst. Solids* **2006**, *352*, 2220–2225.

[21] A. Z. Cardoso, A. E. Alvarez Alvarez, B. N. Cattoz, P. C. Griffiths, S. M. King, W. J. Frith, D. J. Adams, *Faraday Discuss.* **2013**, *166*, 101.

[22] X. Y. Liu, P. D. Sawant, *Appl. Phys. Lett.* **2001**, *79*, 3518–3520.

[23] X. Y. Liu, K. Maiwa, K. Tsukamoto, *J. Chem. Phys.* **1997**, *106*, 1870–1879.

[24] A. Einstein, *Ann. Phys.* **1906**, *324*, 371–381.

[25] D. J. Adams, M. F. Butler, W. J. Frith, M. Kirkland, L. Mullen, P. Sanderson, *Soft Matter* **2009**, *5*, 1856.

[26] R.-Y. Wang, P. Wang, J.-L. Li, B. Yuan, Y. Liu, L. Li, X.-Y. Liu, *Phys. Chem. Chem. Phys.* **2013**, *15*, 3313–9.

[27] Y. Liu, W.-J. Zhao, J.-L. Li, R.-Y. Wang, *Phys. Chem. Chem. Phys.* **2015**, *17*, 8258–65.

[29] C. G. Wolf, E. K. Rideal, *Biochem. J.* **1922**, *16*, 548–555.

[28] G. Ben Messaoud, P. Le Griel, D. Hermida-Merino, S. L. K. W. Roelants, W. Soetaert, C. V. Stevens, N. Baccile, *Chem. Mater.* 2019, *31*, 4817–4830.

[30] A. Z. Cardoso, A. E. Alvarez Alvarez, B. N. Cattoz, P. C. Griffiths, S. M. King, W. J. Frith, D. J. Adams, *Faraday Discuss.* **2013**, *166*, 101–116.

[31] F. M. Menger, Y. Yamasaki, K. K. Catlin, T. Nishimi, *Angew. Chemie Int. Ed. English* **1995**, *34*, 585–586.

[32] E. Dickinson, J. Chem. Soc. - Faraday Trans. 1997, 93, 111–114.

Appendix - Supporting Information

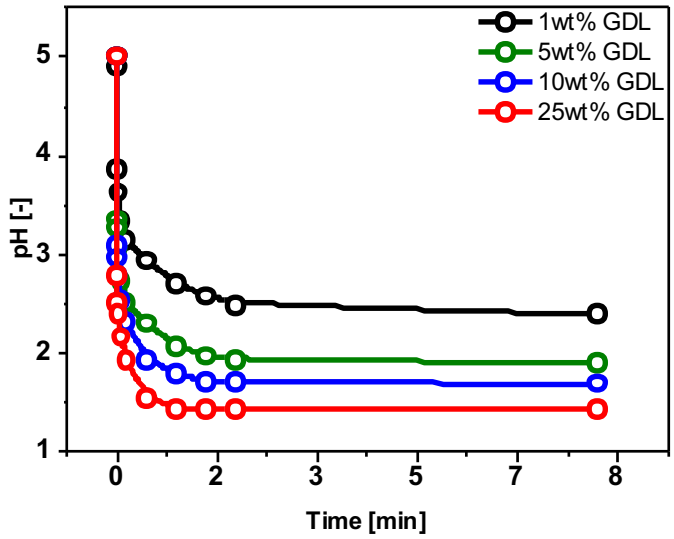

Figure S1. pH profiles upon GDL addition for the case of 2mM Na_2DBC at 1wt.% (57 mM), 5wt.% (295 mM), 10wt.% (624 mM) and 25 wt.% (1871 mM) of GDL. The corresponding [GDL]/[Gelator] molar ratios are 28, 148, 312 and 935 respectively.

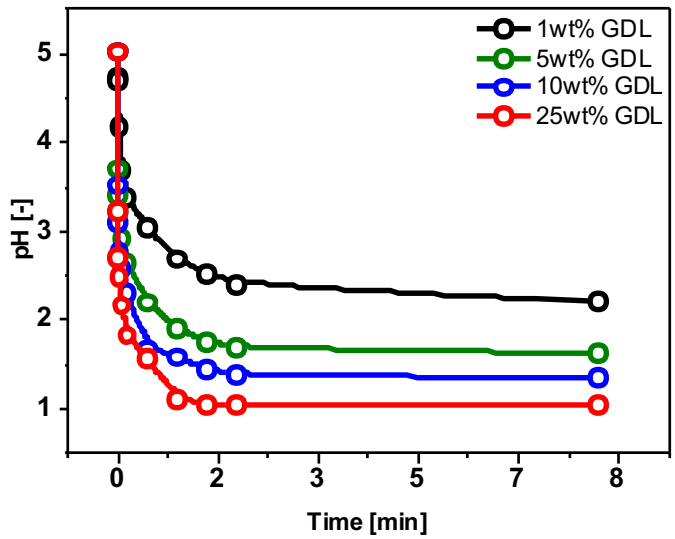

Figure S2. pH profiles upon GDL addition for the case of 10mM Na_2DBC at 1wt.% (57 mM), 5wt.% (295 mM), 10wt.% (624 mM) and 25 wt.% (1871 mM) of GDL. The corresponding [GDL]/[Gelator] molar ratios are 5.7, 29, 62 and 187 respectively.

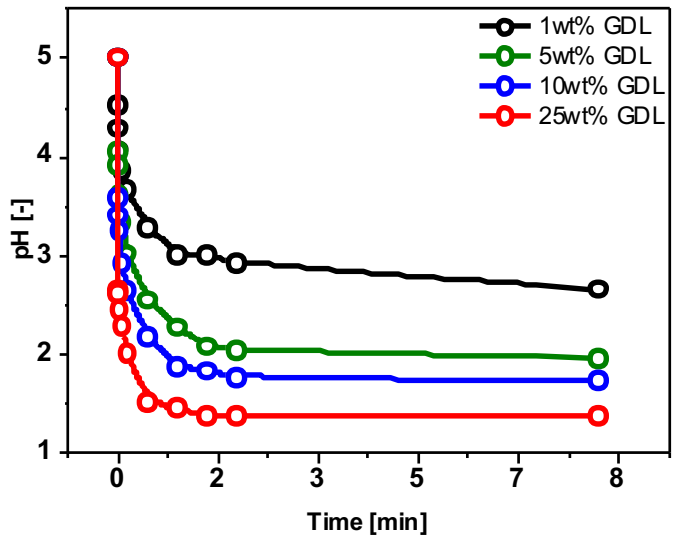

Figure S3. pH profiles upon GDL addition for the case of 20mM Na_2DBC at 1wt.% (57 mM), 5wt.% (295 mM), 10wt.% (624 mM) and 25 wt.% (1871 mM) of GDL. The corresponding [GDL]/[Gelator] molar ratios are 2.8, 15, 31 and 93 respectively.

Table S1. End pH (measured after 8 hours) at different gelator concentrations for 1wt.% (57 mM), 5wt.% (295 mM), 10wt.% (624 mM) and 25 wt.% (1871 mM) of GDL. Molar ratios ([GDL]/[Gelator]) provided in parenthesis ()

GDL (wt.%)	2mM Na_2DBC	5mM Na_2DBC	10mM` Na_2DBC	20mM Na_2DBC	Mean pH	Std.Dev
1	**2.38** (28)	**2.19** (11)	**2.19** (5.7)	**2.65** (2.8)	**2.35**	**0.22**
5	**1.89** (148)	**1.54** (59)	**1.61** (29)	**1.95** (15)	**1.74**	**0.16**
10	**1.68** (312)	**1.3** (125)	**1.34** (62)	**1.72** (31)	**1.51**	**0.22**
25	**1.42** (935)	**1.03** (374)	**1.02** (187)	**1.36** (93)	**1.20**	**0.18**

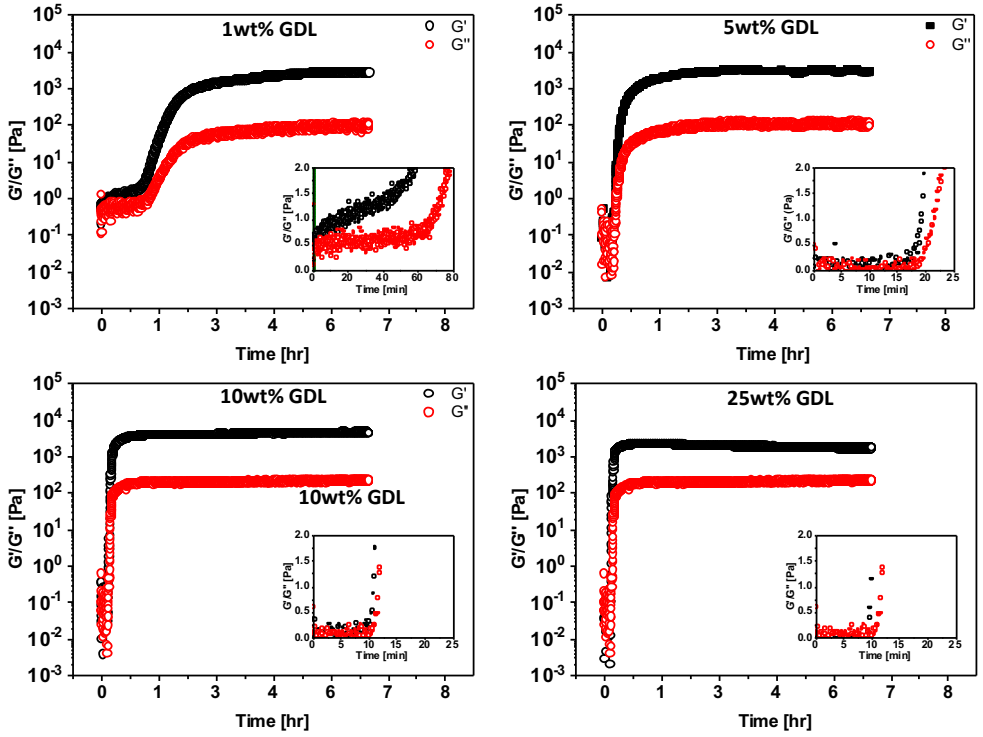

Figure S4. Time evolution of storage and loss moduli at GDL hydrolysis conditions for gelator concentration = 2mM 1wt.% (57 mM), 5wt.% (295 mM), 10wt.% (624 mM) and 25 wt.% (1871 mM) of GDL. The corresponding [GDL]/[Gelator] molar ratios are 28, 148, 312 and 935 respectively.

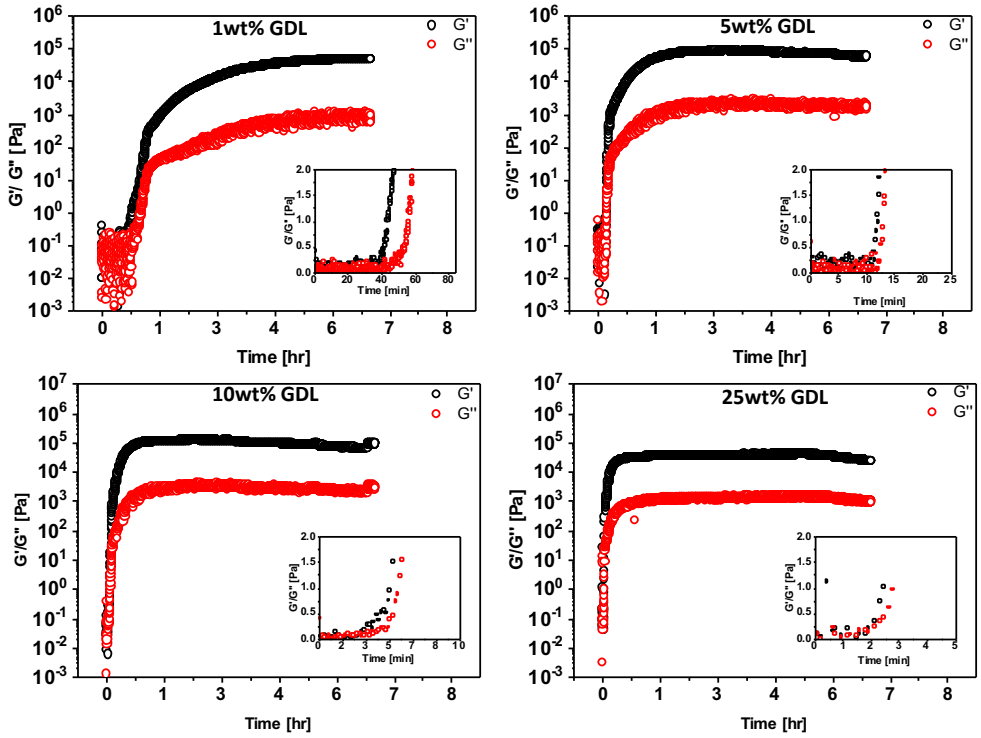

Figure S5. Time evolution of storage and loss moduli at GDL hydrolysis conditions for gelator concentration = 10mM and 1wt.% (57 mM), 5wt.% (295 mM), 10wt.% (624 mM) and 25 wt.% (1871 mM) of GDL. The corresponding [GDL]/[Gelator] molar ratios are 5.7, 29, 62 and 187 respectively.

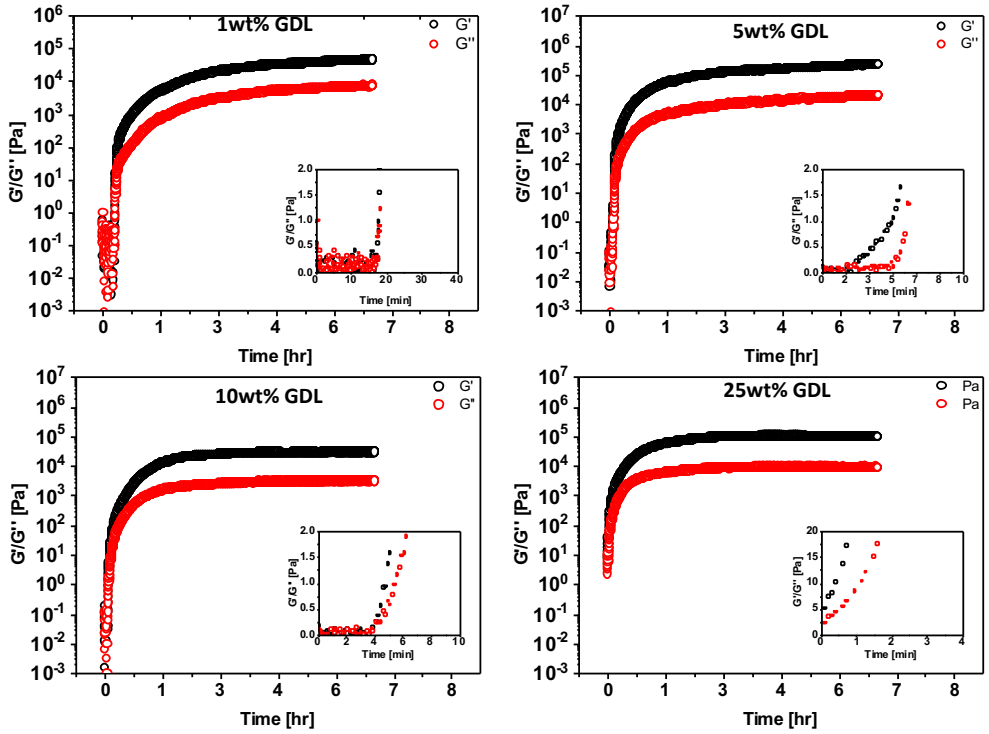

Figure S6. Time evolution of storage and loss moduli at GDL hydrolysis conditions for gelator concentration = 20mM and 1wt.% (57 mM), 5wt.% (295 mM), 10wt.% (624 mM) and 25 wt.% (1871 mM) of GDL. The corresponding [GDL]/[Gelator] molar ratios are 2.8, 15, 31 and 93 respectively.

Dickinson Model – Equation S1

$$\ln\left[\frac{G'^{(t)} - G'^{(0)}}{G'^{(\infty)} - G'^{(0)}}\right] \propto \frac{3 - D_{f,D}}{D_{f,D}} \ln\left(t - t_{gel}\right)$$

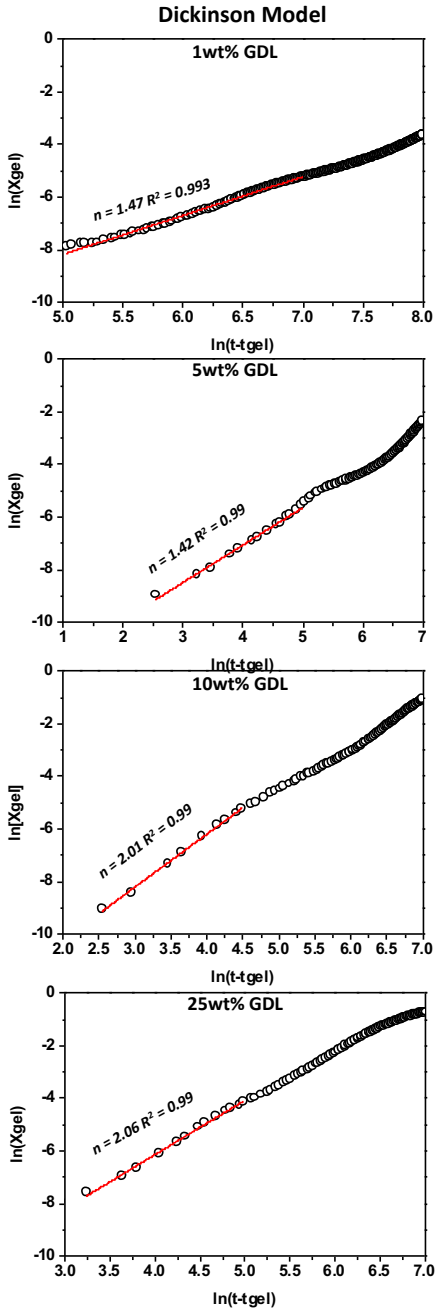

Figure S7. Model fits based on Dickinson model for case of 5mM gelator concentration and 1wt.% (57 mM), 5wt.% (295 mM), 10wt.% (624 mM) and 25 wt.% (1871 mM) of GDL. The corresponding [GDL]/[Gelator] molar ratios are 11, 59, 125 and 374 respectively).

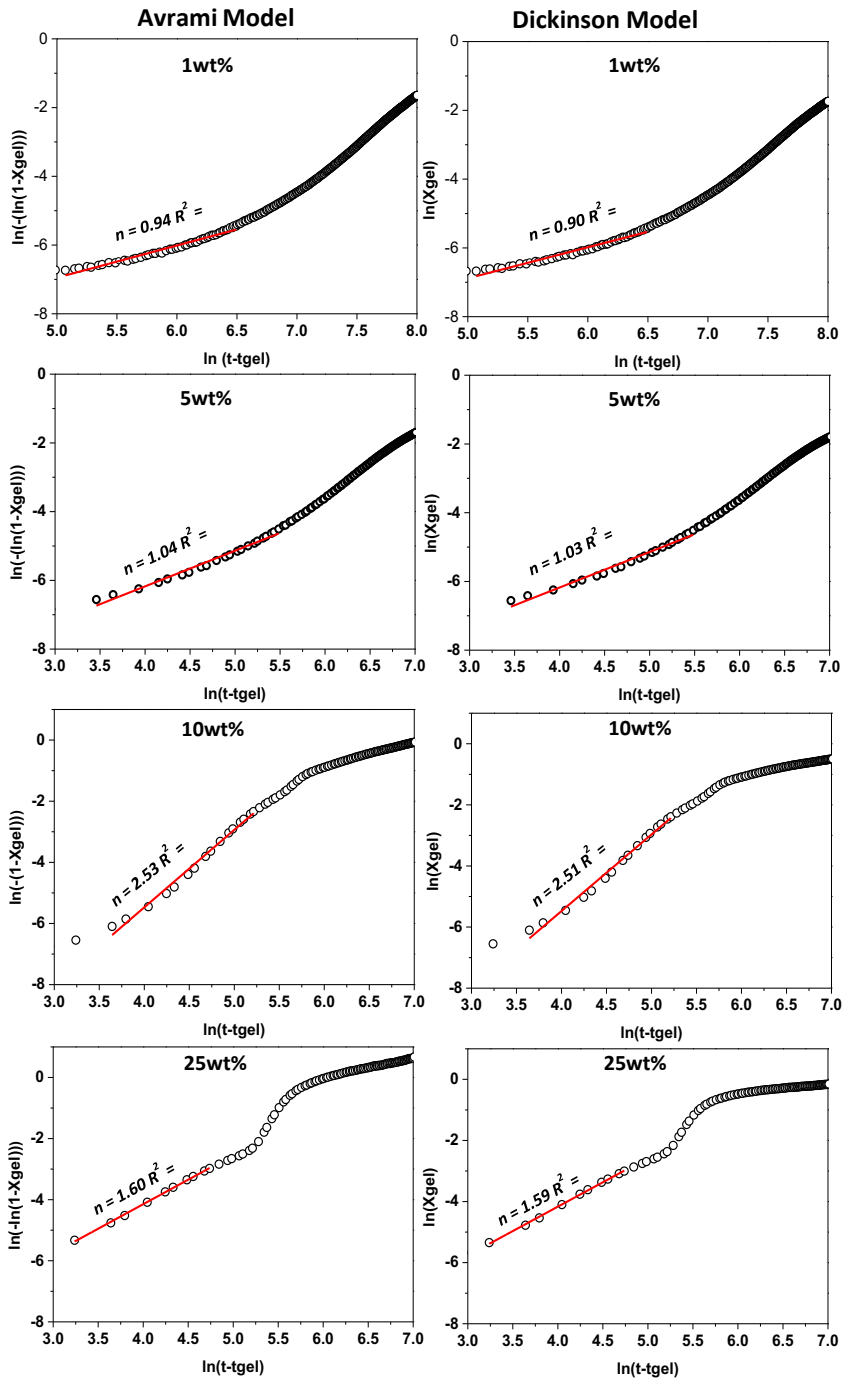

Figure S8. Model fits based on Avrami and Dickinson models for case of 2mM gelator concentration and 1wt.% (57 mM), 5wt.% (295 mM), 10wt.% (624 mM) and 25 wt.% (1871 mM) of GDL. The corresponding [GDL]/[Gelator] molar ratios are 28, 148, 312 and 935 respectively.

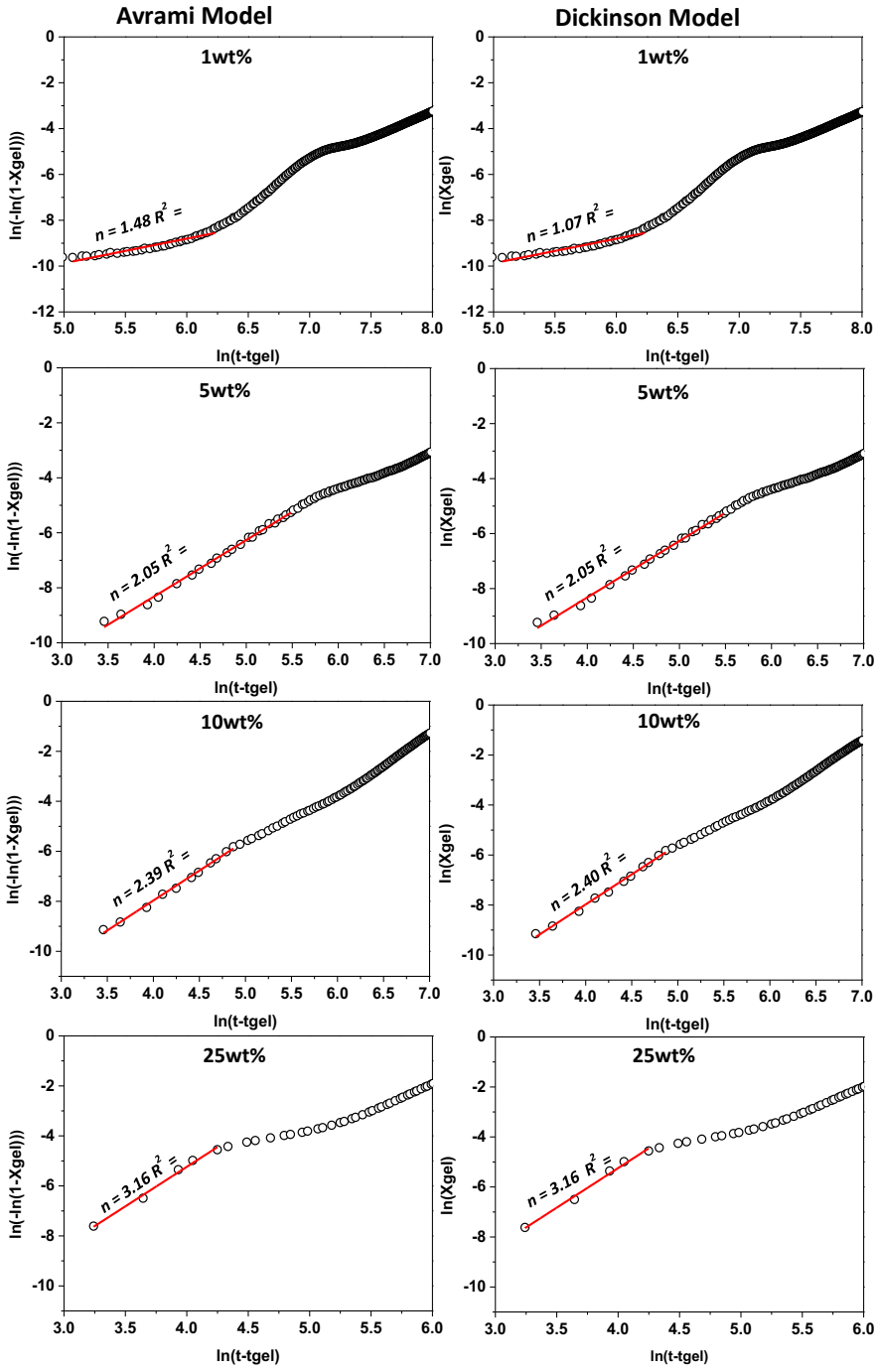

Figure S9. Model fits based on Avrami and Dickinson models for case of 10mM gelator concentration and 1wt.% (57 mM), 5wt.% (295 mM), 10wt.% (624 mM) and 25 wt.% (1871 mM) of GDL. The corresponding [GDL]/[Gelator] molar ratios are 5.7, 29, 62 and 187 respectively.

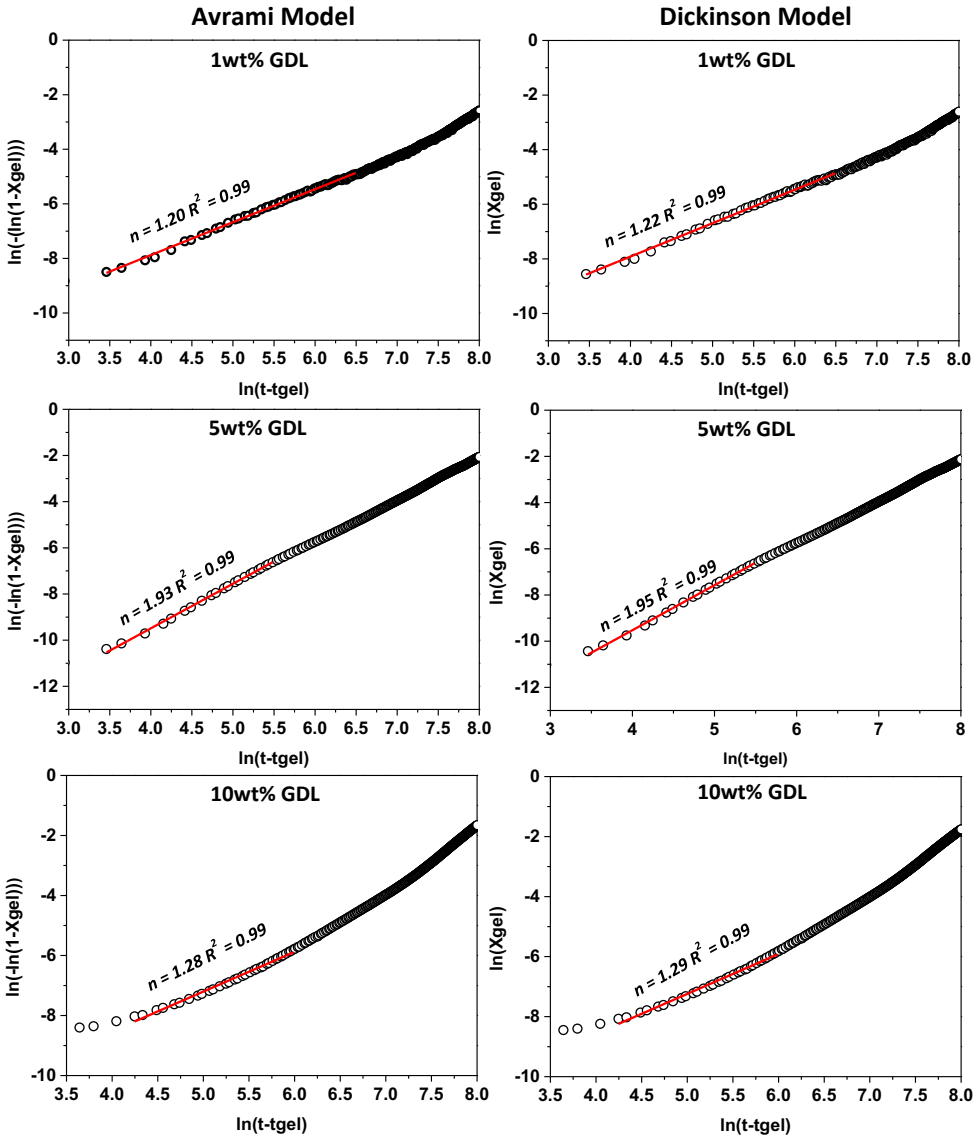

Figure S10. Model fits based on Avrami and Dickinson models for case of 20mM gelator concentration 1wt.% (57 mM), 5wt.% (295 mM) and 10wt.% (624 mM) of GDL. The corresponding [GDL]/[Gelator] molar ratios are 2.8, 15 and 31 respectively.

Table S2. Fitting values for Avrami fits for different region selected in x-axis

Sample Code	Region	n	Pearson r	adjusted r-square
2mM 1%	5 - 6.5	0.936	0.985	0.971
2mM 1%	5 - 7.0	1.254	0.979	0.959
5mM 1%	5 - 6.5	1.375	0.993	0.987
5mM 1%	5 - 7.0	1.475	0.996	0.993
10mM 1%	5 - 6.5	1.483	0.952	0.904
10mM 1%	5 - 6.25	1.072	0.966	0.931
20mM 1%	3.5 - 7.0	1.192	0.998	0.997
20mM 1%	3.5 - 6.5	1.207	0.998	0.997
2mM 5%	3.5 - 6.0	1.228	0.987	0.973
2mM 5%	3.5 - 5.5	1.036	0.991	0.981
5mM 5%	2.5 - 5.25	1.5	0.995	0.99
5mM 5%	2.5 - 5.0	1.421	0.996	0.992
10mM 5%	3.5 - 5.5	2.049	0.998	0.996
10mM 5%	3.5- 5.25	2.037	0.997	0.994
20mM 5%	3.0 - 6.0	1.892	0.999	0.998
20mM 5%	3.0 - 5.5	1,931	0.999	0.998
2mM 10%	3.5 - 5.25	2.534	0.994	0.988
2mM 10%	3 - 4.5	1.718	0.986	0.968
5mM 10%	2.5 - 4.5	1.989	0.999	0.998
5mM 10%	2.5 - 4.25	2.015	0.999	0.997
10mM 10%	3.5 - 4.85	2.394	0.997	0.995
10mM 10%	3.5 - 4.5	2.244	0.997	0.994
20mM 10%	4.25 - 6	1.323	0.995	0.991
20mM 10%	4.0 - 6.0	1.288	0.994	0.988
2mM 25%	3.25 - 5.0	1.569	0.999	0.998
2mM 25%	3.25 - 4.75	1.604	0.999	0.998
5mM 25%	3.0 - 5.0	2.067	0.998	0.996
5mM 25%	3.0 - 4.75	2.084	0.997	0.994
10mM 25%	3.25 - 4.0	3.298	0.996	0.989
10mM 25%	3.25 - 4.25	3.16	0.996	0.989
20mM 25%	-	-		

Table S3. Fitting values for Dickinson fits for different region selected in x-axis

Sample Code	Selection	n	Pearson r	adjusted r-square
2mM 1%	5 - 6.5	0.903	0.985	0.969
2mM 1%	5 - 7.0	1.209	0.978	0.957
5mM 1%	5 - 6.5	1.375	0.994	0.987
5mM 1%	5 - 7.0	1.475	0.996	0.993
10mM 1%	5 - 6.5	1.48	0.952	0.904
10mM 1%	5 - 6.25	1.069	0.966	0.93
20mM 1%	3.5 - 7.0	1.204	0.998	0.997
20mM 1%	3.5 - 6.5	1.223	0.998	0.997
2mM 5%	3.5 - 6.0	1.223	0.987	0.974
2mM 5%	3.5 - 5.5	1.033	0.991	0.981
5mM 5%	2.5 - 5.15	1.505	0.995	0.99
5mM 5%	2.5 - 5.0	1.426	0.996	0.992
10mM 5%	3.5 - 5.5	2.051	0.998	0.996
10mM 5%	3.5 - 5.25	2.039	0.997	0.994
20mM 5%	3.0 - 6.0	1.908	0.999	0.998
20mM 5%	3.0 - 5.5	1.948	0.999	0.998
2mM 10%	3.5 - 5.25	2.507	0.995	0.989
2mM 10%	3 - 4.5	1.715	0.986	0.968
5mM 10%	2.5 - 4.5	2.012	0.999	0.997
5mM 10%	2.5 - 4.25	2.041	0.998	0.997
10mM 10%	3.5 - 4.85	2.402	0.997	0.995
10mM 10%	3.5 - 4.5	2.255	0.997	0.994
20mM 10%	4.25 - 6	1.328	0.995	0.991
20mM 10%	4.0 - 6.0	1.294	0.994	0.989
2mM 25%	3.25 - 5.0	1.558	0.999	0.998
2mM 25%	3.25 - 4.75	1.597	0.999	0.998
5mM 25%	3.25 - 5.0	2.066	0.998	0.996
5mM 25%	3.25 - 4.75	2.084	0.997	0.994
10mM 25%	3.25 - 4.0	3.303	0.996	0.989
10mM 25%	3.25 - 4.25	3.165	0.996	0.989
20mM 25%	-	-	-	-

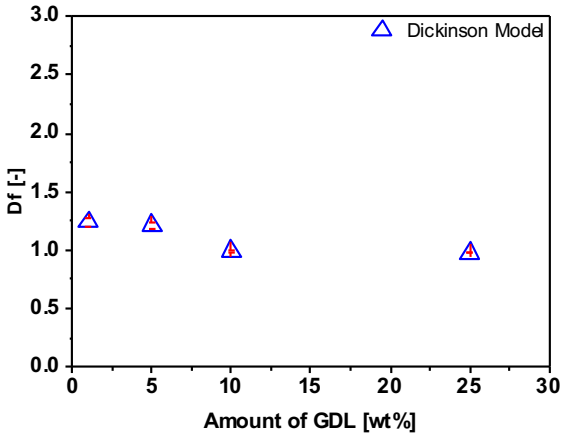

Figure S11. Model predictions for D_f from Dickinson model in hydrogels formed from 5mM of gelator at various amounts of GDL (1wt.% (57 mM), 5wt.% (295 mM), 10wt.% (624 mM) and 25 wt.% (1871 mM)). The corresponding [GDL]/[Gelator] molar ratios are 11, 59, 125 and 374 respectively.

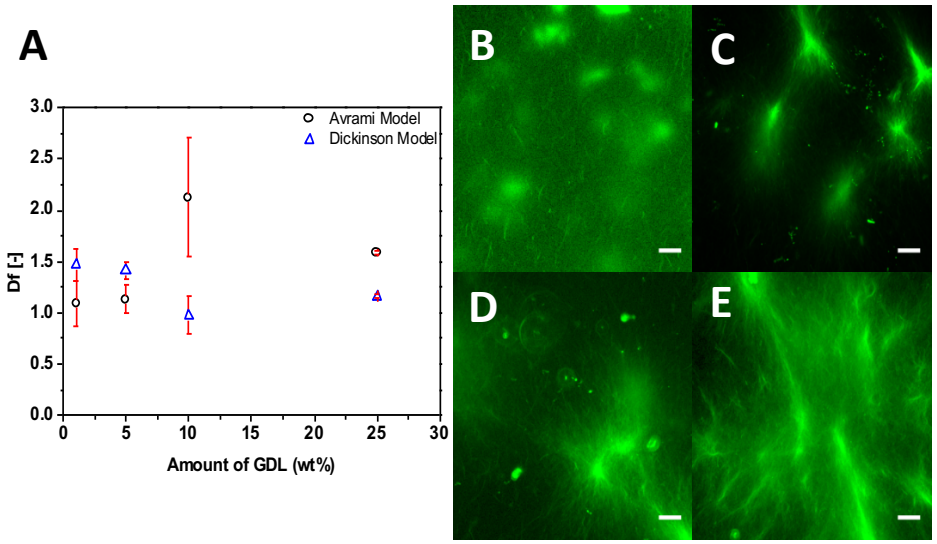

Figure S12. Model predictions for D_f from Avrami and Dickinson models[A]; False-colour CLSM micrographs showing difference in morphology in hydrogels formed from 2mM of gelator upon addition of 1wt.% (57 mM) [B], 5wt.% (295 mM) [C],10wt.% (624 mM) [D] and 25wt.% (1871 mM) [E] of GDL. The corresponding [GDL]/[Gelator] molar ratios are 28, 148, 312 and 935 respectively. Scale bar is 20µm.

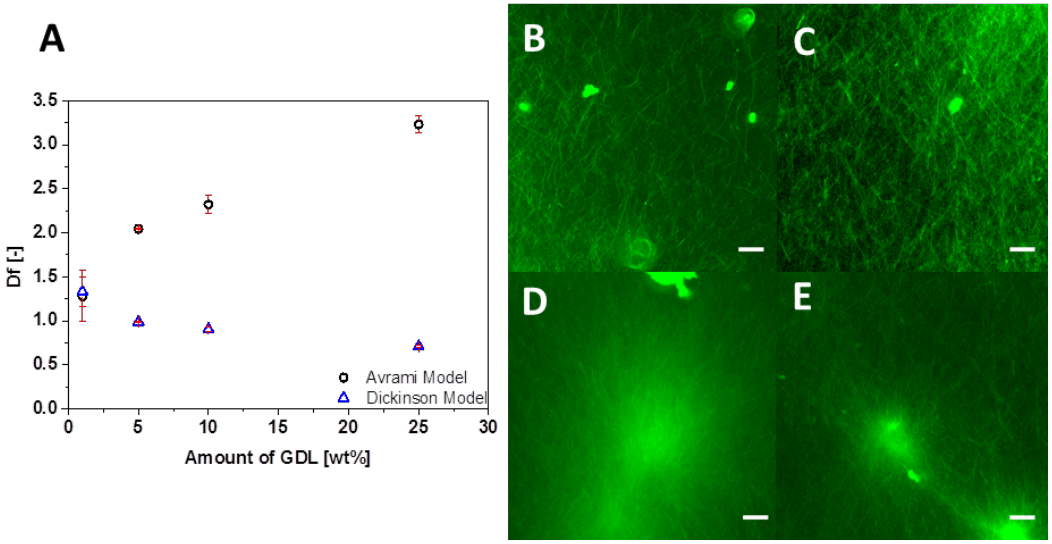

Figure S13. Model predictions for D_f from Avrami and Dickinson models [A]; False-colour CLSM micrographs showing difference in morphology in hydrogels formed from 10mM of gelator upon addition of 1wt.% (57 mM) [B], 5wt.% (295 mM) [C],10wt.% (624 mM) [D] and 25wt.% (1871 mM) [E] of GDL. . The corresponding [GDL]/[Gelator] molar ratios are 5.7, 29, 62 and 187 respectively. Scale bar is 20µm.

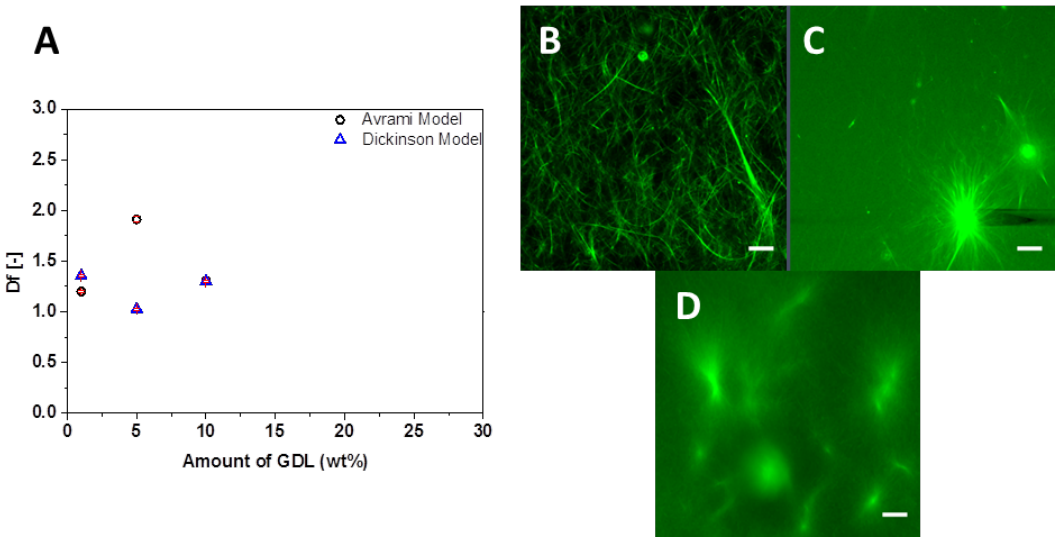

Figure S14. Model predictions for D_f from Avrami and Dickinson models [A]; False-colour CLSM micrographs showing difference in morphology in hydrogels formed from 10mM of gelator upon addition of 1wt.% (57 mM) [B], 5wt.% (295 mM) [C] and 10wt.% (624 mM) [D] of GDL. The corresponding [GDL]/[Gelator] molar ratios are 2.8, 15 and 31 respectively. Scale bar is 20µm.

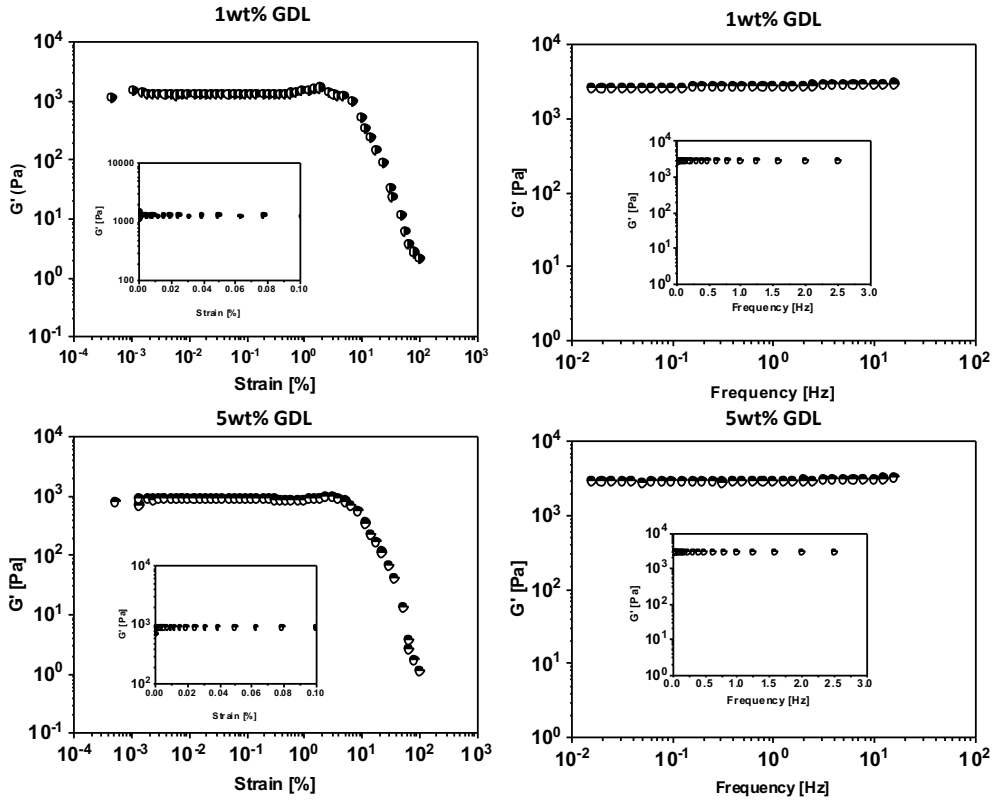

Figure S15. Strain and frequency sweeps at gelator concentration of 2mM and 1wt.% (57 mM) and 5wt.% (295 mM) of GDL. The corresponding [GDL]/[Gelator] molar ratios are 28 and 148 respectively.

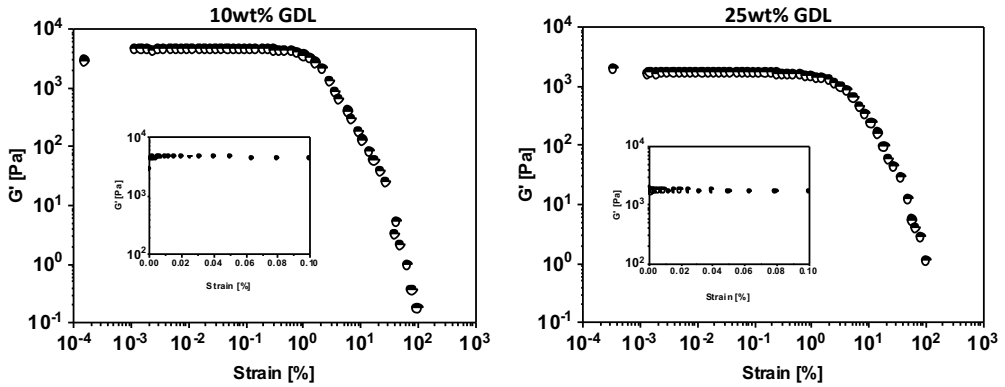

Figure S16.More strain sweeps at gelator concentration = 2mM and 10wt.% (624 mM), 25wt.% (1871 mM) of GDL. The corresponding [GDL]/[Gelator] molar ratios are 312 and 935 respectively.

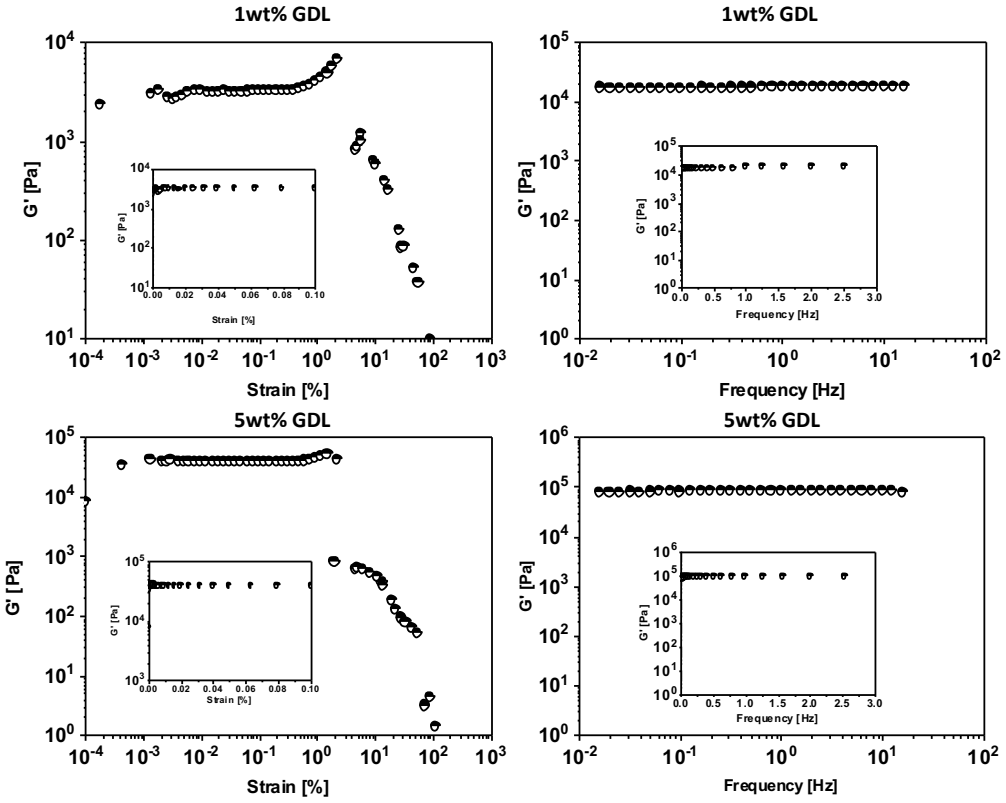

Figure S17. Strain and frequency sweeps at gelator concentration = 5mM and 1wt.% (57 mM) and 5wt.% (295 mM) of GDL. The corresponding [GDL]/[Gelator] molar ratios are 11 and 59 respectively.

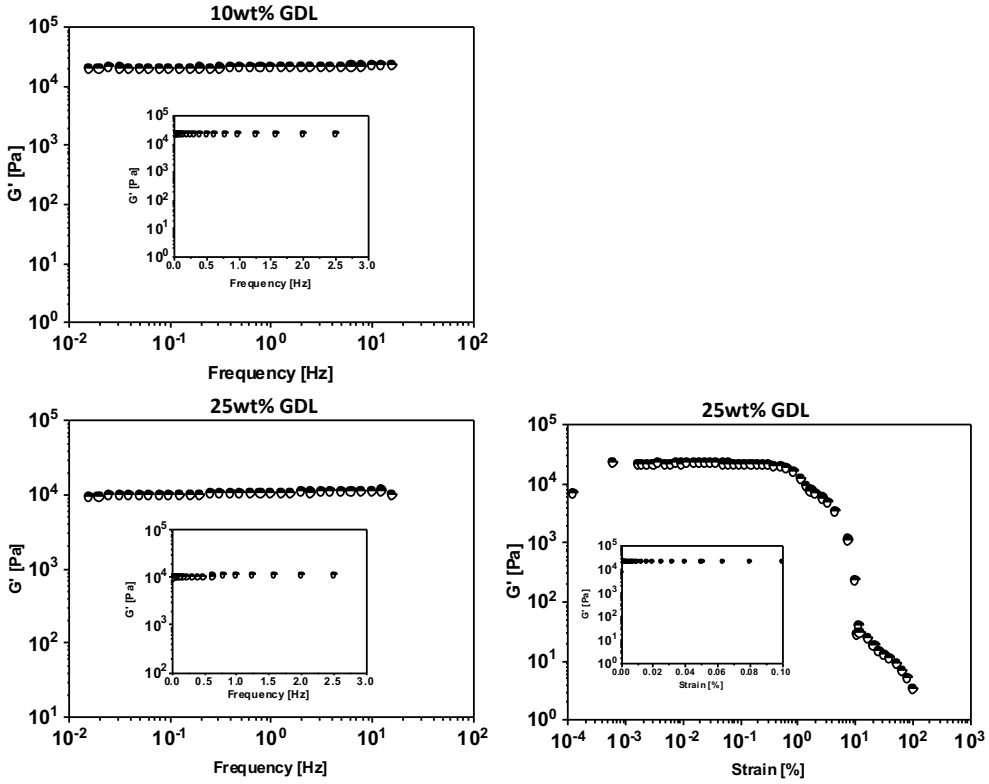

Figure S18.More strain and frequency sweeps at gelator concentration = 5mM and 10wt.% (624 mM), 25wt.% (1871 mM) of GDL. The corresponding [GDL]/[Gelator] molar ratios are 125 and 374 respectively.

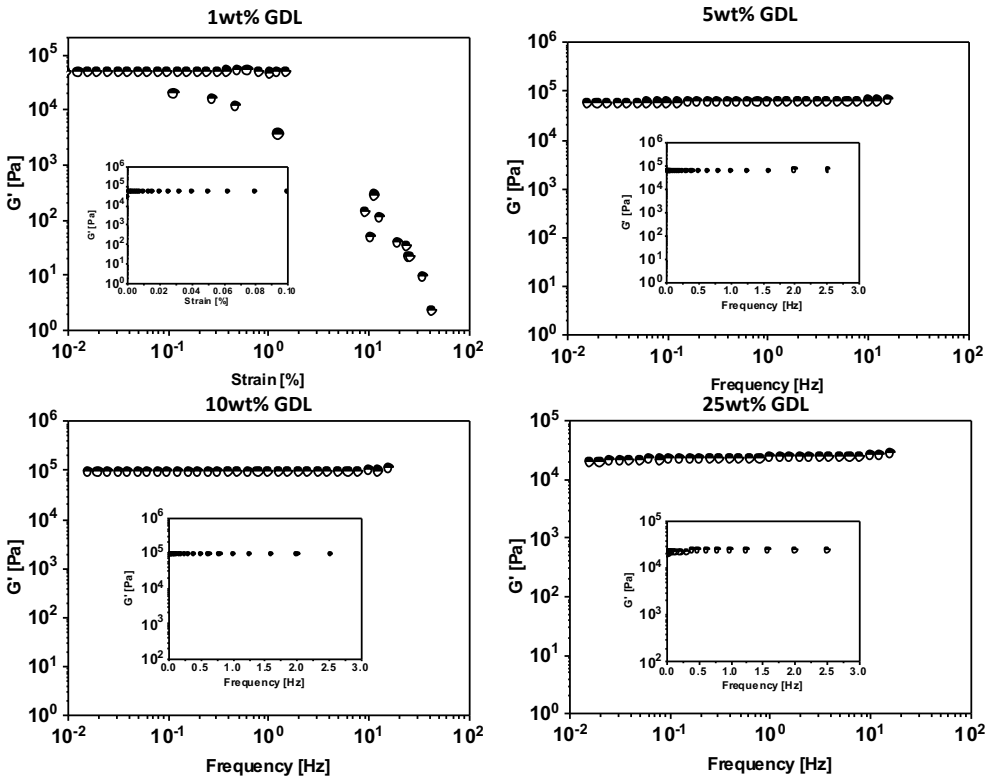

Figure S19. Strain and Frequency Sweeps at gelator concentration = 10mM and 1wt.% (57 mM), 5wt.% (295 mM), 10wt.% (624 mM), 25wt.% (1871 mM) of GDL. The corresponding [GDL]/[Gelator] molar ratios are 5.7, 29, 62 and 187 respectively.

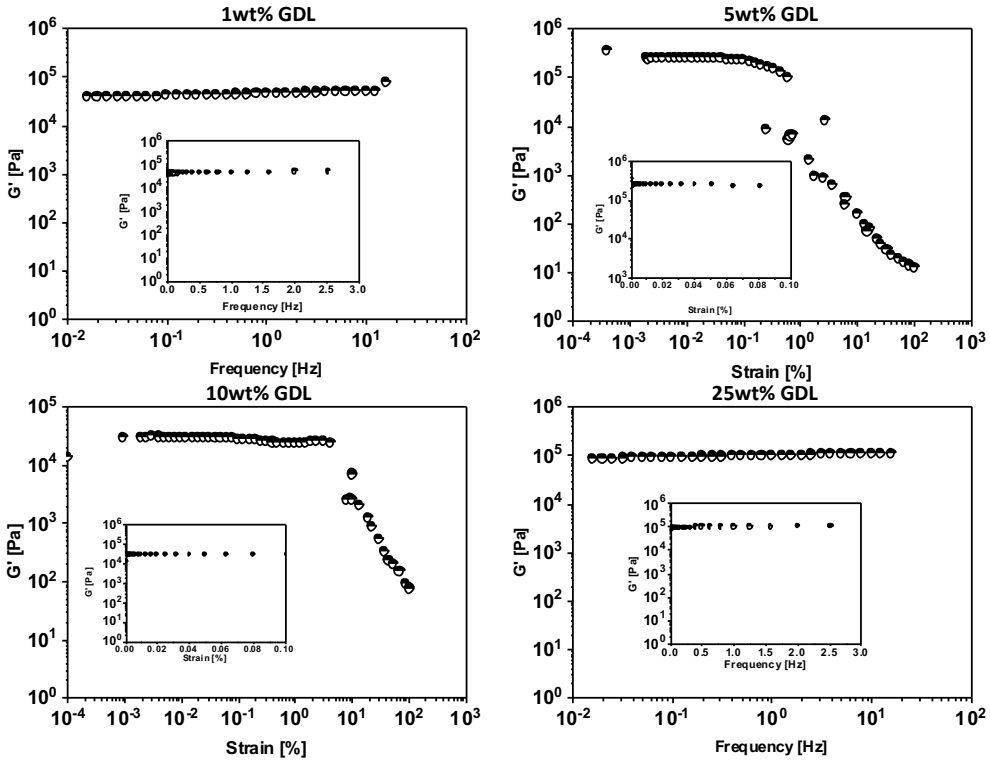

Figure S20. Strain and Frequency Sweeps at gelator concentration = 20mM and 1wt.% (57 mM), 5wt.% (295 mM), 10wt.% (624 mM), 25wt.% (1871 mM) of GDL. The corresponding [GDL]/[Gelator] molar ratios are 2.8, 15, 31 and 93 respectively.

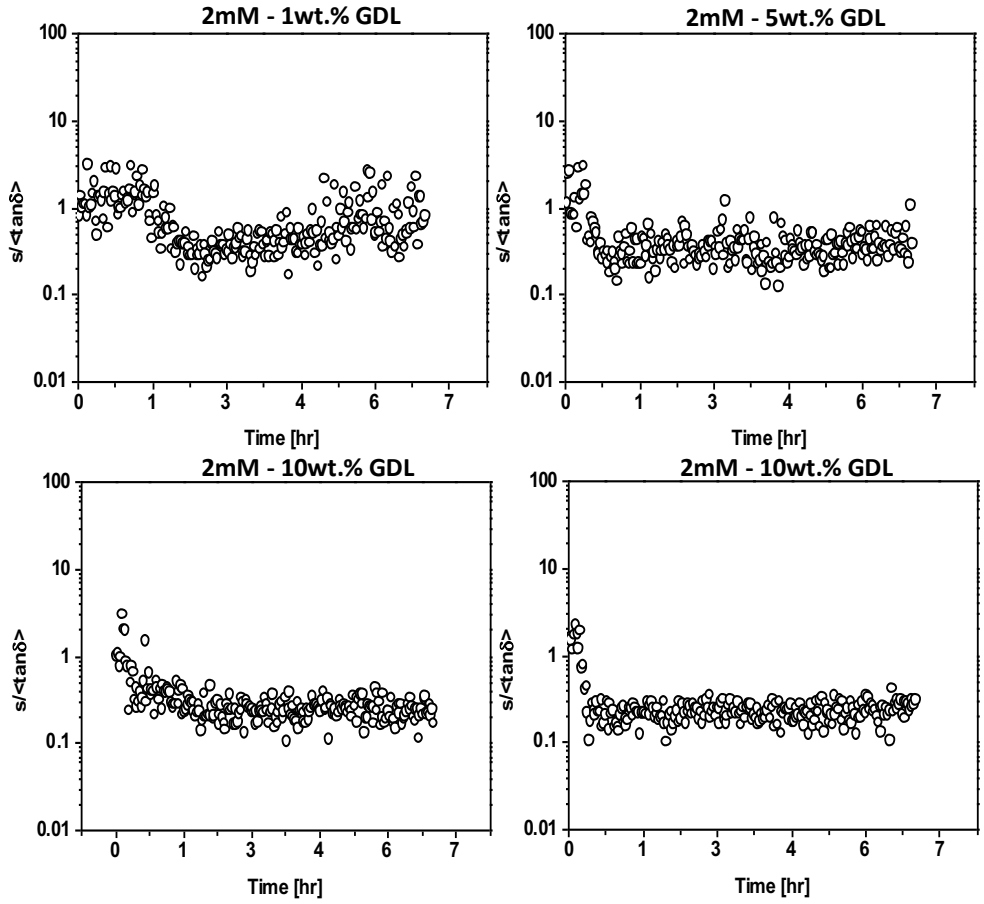

Figure S21. Tanδ analysis for data obtained at a gelator concentration of 2mM and 1wt.% (57 mM), 5wt.% (295 mM), 10wt.% (624 mM), 25wt.% (1871 mM) of GDL. The corresponding [GDL]/[Gelator] molar ratios are 28, 148, 312 and 935 respectively.

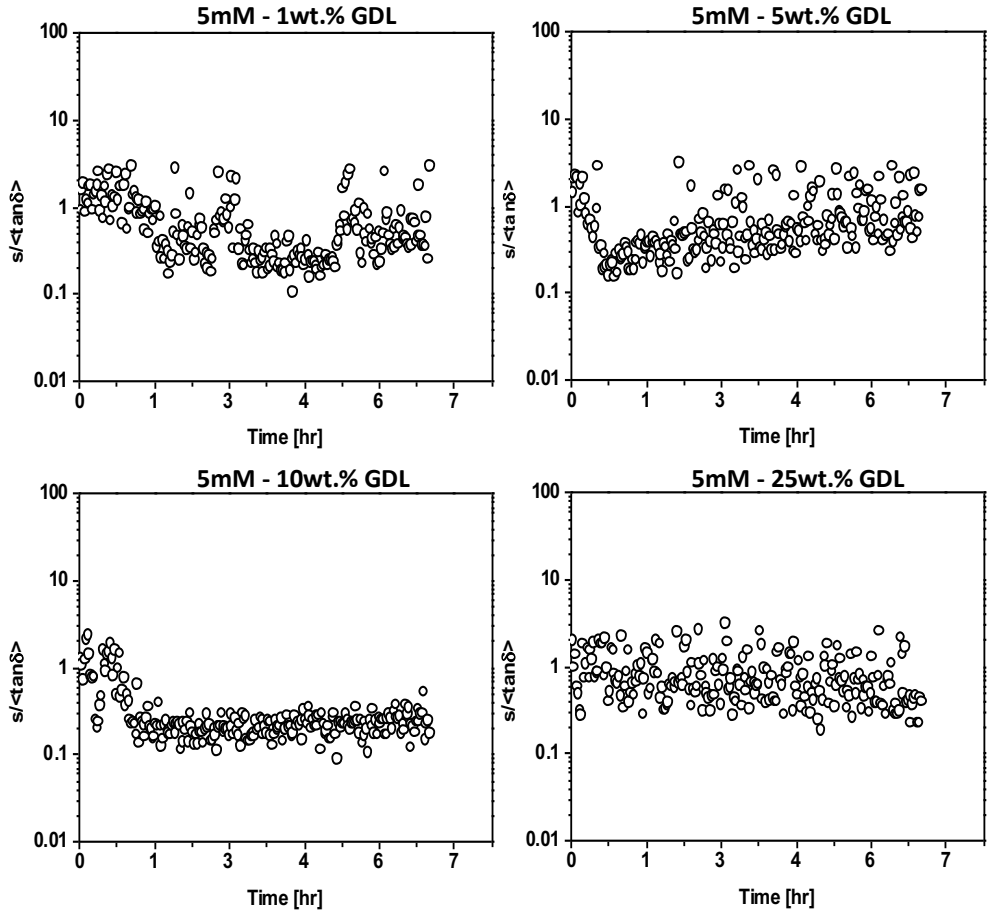

Figure S22. Tanδ analysis for data obtained at a gelator concentration of 5mM and 1wt.% (57 mM), 5wt.% (295 mM), 10wt.% (624 mM), 25wt.% (1871 mM) of GDL. The corresponding [GDL]/[Gelator] molar ratios are 11, 59, 125 and 374 respectively.

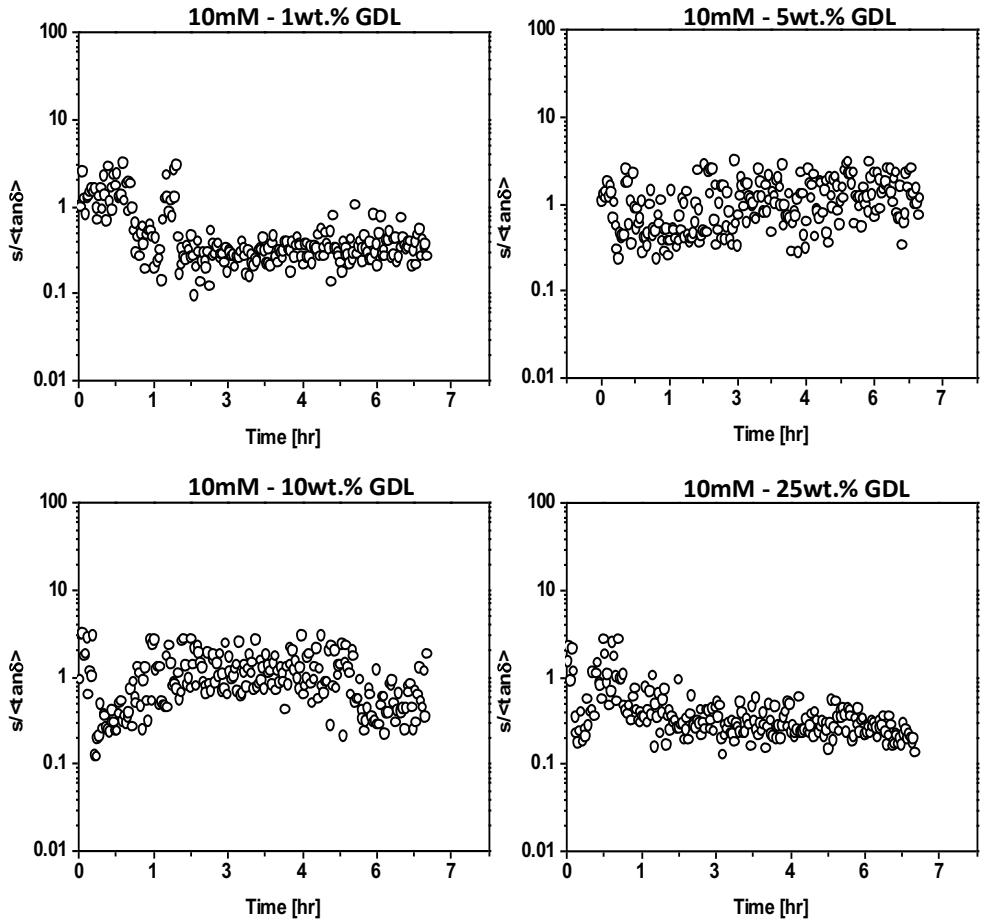

Figure S23. Tanδ analysis for data obtained at a gelator concentration of 10mM and 1wt.% (57 mM), 5wt.% (295 mM), 10wt.% (624 mM), 25wt.% (1871 mM) of GDL. The corresponding [GDL]/[Gelator] molar ratios are 5.7, 29, 62 and 187 respectively.

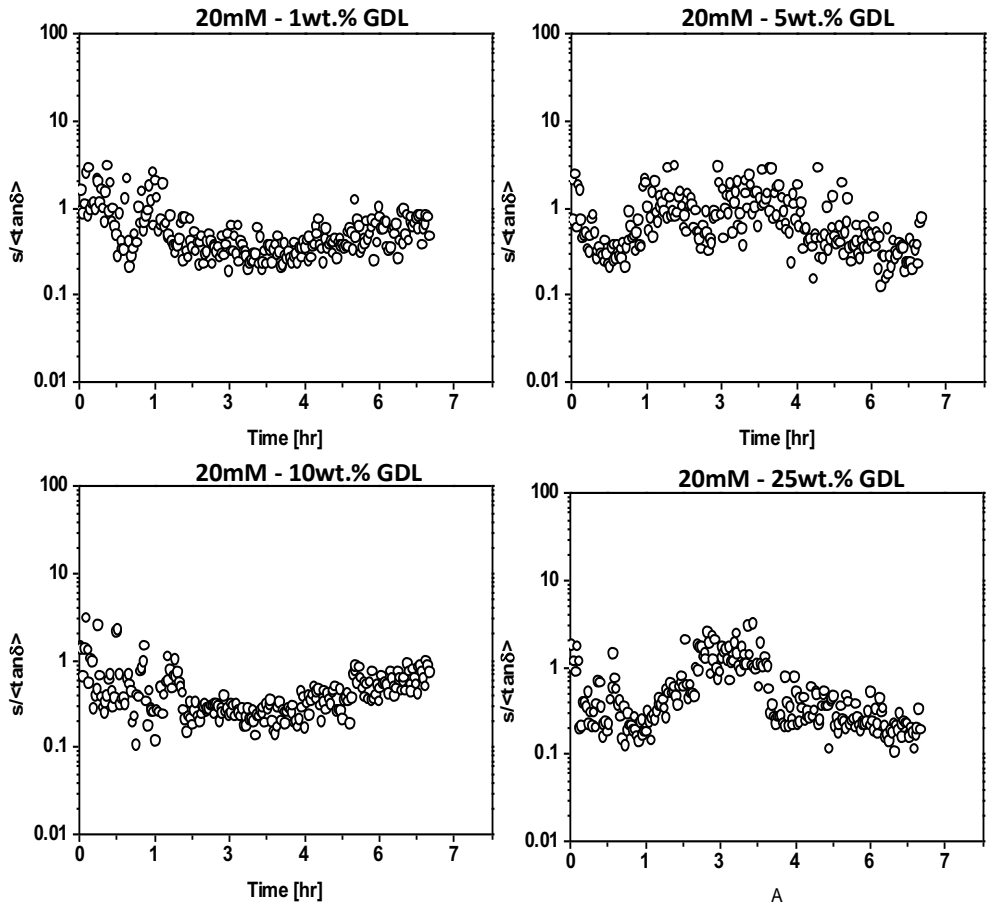

Figure S24. Tanδ analysis for data obtained at a gelator concentration of 20mM and 1wt.% (57 mM), 5wt.% (295 mM), 10wt.% (624 mM), 25wt.% (1871 mM) of GDL. The corresponding [GDL]/[Gelator] molar ratios are 2.8, 15, 31 and 93 respectively.

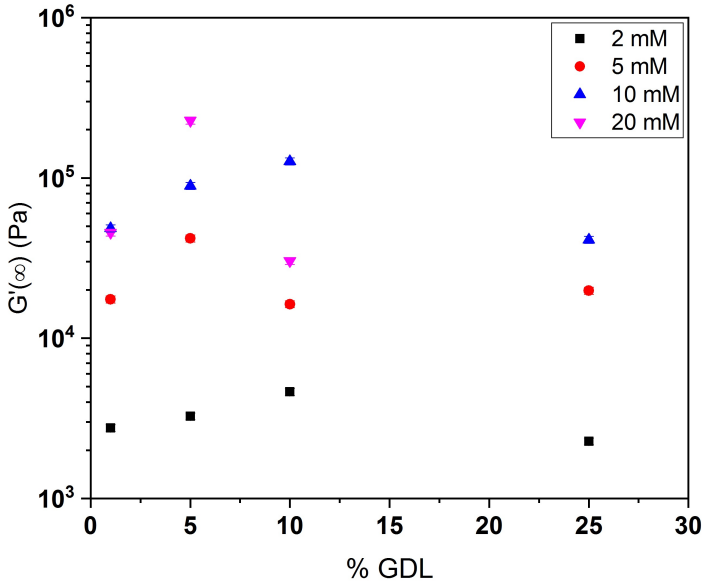

Figure S25. Plot of plateau modulus (G'(∞)) at various gelator (DBC) and trigger (GDL) concentrations (1wt.% (57 mM), 5wt.% (295 mM), 10wt.% (624 mM), 25wt.% (1871 mM))

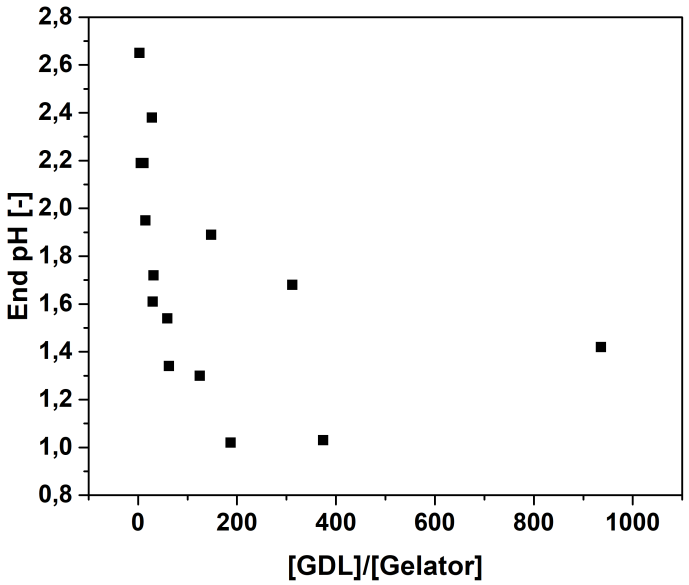

Figure S26. Plot of End pH at various [GDL]/[Gelator] molar ratios (GDL - 1wt.% (57 mM), 5wt.% (295 mM), 10wt.% (624 mM), 25wt.% (1871 mM), Gelator – 2mM, 5mM, 10mM, 20mM)

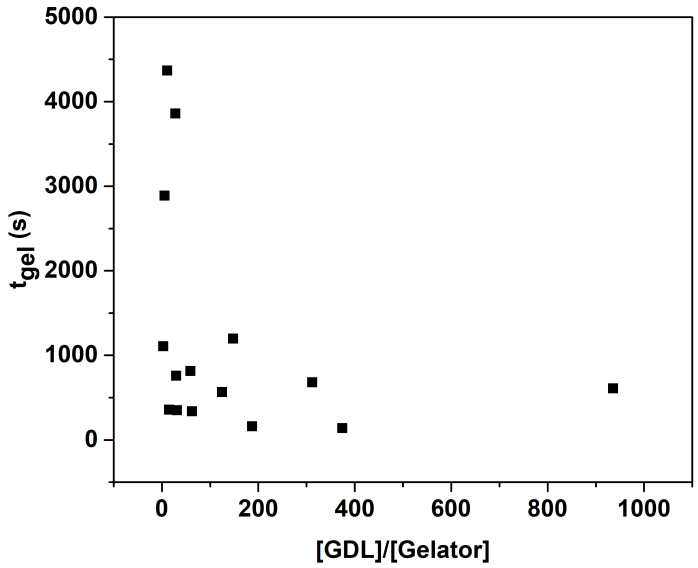

Figure S27. Plot of t_{gel} at various [GDL]/[Gelator] molar ratios (GDL - 1wt.% (57 mM), 5wt.% (295 mM), 10wt.% (624 mM), 25wt.% (1871 mM), Gelator – 2mM, 5mM, 10mM, 20mM)

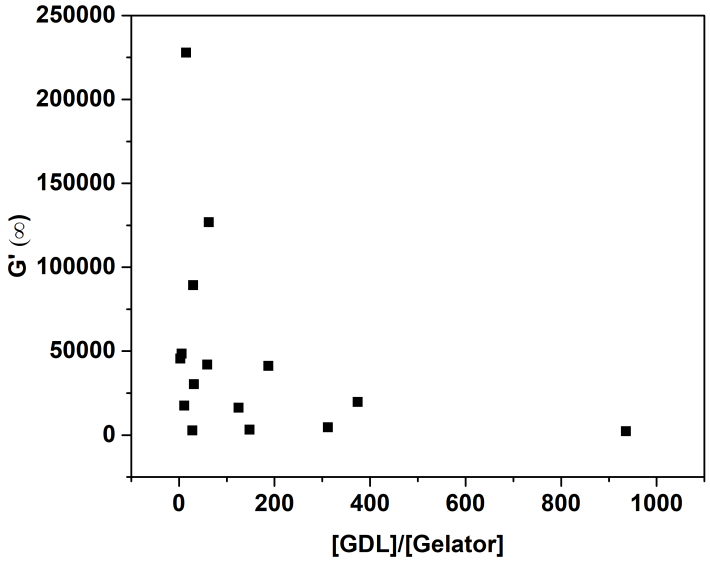

Figure S28. Plot of plateau modulus (G'(∞)) at various [GDL]/[Gelator] molar ratios (GDL - 1wt.% (57 mM), 5wt.% (295 mM), 10wt.% (624 mM), 25wt.% (1871 mM), 25wt.% (1871.2 mM), Gelator – 2mM, 5mM, 10mM, 20mM)

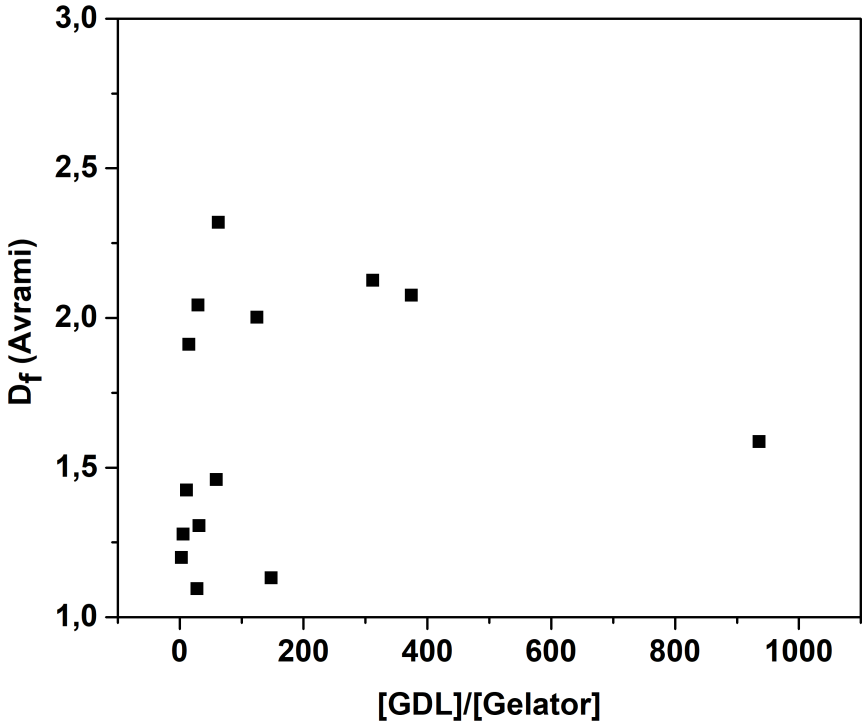

Figure S29. Plot of D_f (avrami) at various [GDL]/[Gelator] molar ratios (GDL - 1wt.% (57 mM), 5wt.% (295 mM), 10wt.% (624 mM), 25wt.% (1871 mM), Gelator – 2mM, 5mM, 10mM, 20mM)

Chapter 3

Random graph model for sparse supramolecular networks of self-assembled low molecular weight gelators

---

Abstract: *Gels are large network-like arrangements of molecules that exhibit special physical properties such as viscoelasticity, shape memory, self-healing, thanks to their underlying network structure. Unlike conventional covalently-bonded polymer gels, supramolecular gelation is yet to be comprehensively understood owning to the variety of triggering mechanisms and diversity of gelator molecular species. This work is an early attempt to study supramolecular gelation of Dibenzoyl-L-Cystine (DBC) that is triggered by hydrolysis of Glucono-delta-lactone (GDL) by means of experimental observations and a dynamic network model with two types of bonds. Several parameters, such as the gelation time, gel fraction at equilibrium, and network density, were predicted by the model, among which the gelation time was experimentally following the gelation through rheology. The model predictions are in agreement with experimental data. We also theoretically demonstrate how such a modelling approach enables experimentalists to rapidly screen through the parameter space of formulations. We believe this approach is useful for researchers working to create supramolecular gels with desired properties for drug delivery, tissue engineering, and cell culturing among several other applications.*

3.1 Introduction

Supramolecular hydrogels formed out of Low Molecular Weigh Hydrogelators are gaining a lot of attention in the last several years due to the diversity of molecular motifs, triggers, tuneable properties and potential applications.[1] Over the years, researchers have also tried to study the self-assembly of these gelators.[2] For pH-triggered LMWHs, it has been shown that the there is a role of kinetics on the homogeneity, mechanical properties and hence microstructure of formed hydrogels.[3,4] Recently in our work on gelation-kinetics and structure analysis, rheology time sweep data was used to compare existing fibre branching models that were developed for temperature triggered formation of organogels for pH-triggered LMWHs.[5] Despite the understanding generated over the years in the field, development of predictive models that can predict gelation or gel properties has only started recently. Molecular dynamics (MD) simulations and density functional theory (DFT) calculations have been carried out in a number of LMWG systems to understand self-assembly and calculate solubility parameters that are important to understand in the context of gelation.[6,7] These methods are useful as virtual microscopes to be able to visualize early stages of in the aggregation of LMWH or LMWG systems. Recently, Berry et.al reported on the first successful predictive models of gelation properties of mono/dipeptide based LMWHs.[8] Using Quantitative structure–property relationships that link measured properties to compound chemical structure and combining with machine learning methods (Support Vector Machines (SVM), Random Forests (RF), k nearest neighbours (kNN), Neural Networks (NN), Partial Least Squares (PLS), Naïve Bayesian (NB) and C5.0., they were able to create a model that could predict with good accuracy if a given molecule would gelate or not.[8] Very recently in 2020, Alonso et.al reported a model combining MD and machine learning that could predict whether a urea-based gelator would gelate, precipitate or solubilize in a given solvent (organic or water). They also compared their work with earlier on MD simulations by Boutellier, Tuttle and Ulijn, Adams and Berry and argued that their model is the first computational model that can predict gelation of urea-based gelators and can help in the discovery of new gelators without laborious efforts or difficult coarse-gained models.[9] These reports show that the field of predictive modelling in LWMH is young and

inviting more contributions. Moreover MD simulations are computationally expensive and applicability of these models to other gelator systems would need dedicated simulation models.[9] We wondered if there is a way to model LMWH supramolecular hydrogels in a manner similar to recently developed models for linear polymerization.[10–12]

Conventional linear polymers are long chains made of many repeated units that are connected by strong covalent bonds, whereas as supramolecular hydrogels such as those formed out of LMWHs make use of weaker, reversible interactions that hold the chains together. Such a reversibility of bonds requires revision of the modelling approaches that have been successful in the context of conventional polymers: not many existing polymer models can easily adopt the growth mechanisms of reversible supramolecular polymerization, which means that bonds may form and dissociate. In fact, modelling the reversible assembly of linear fibrils is already a challenge.[13–15] If fibrils are short or comprise an overcrowded system, jamming of fractal or cylindrical colloids can be a good approximation for supramolecular microstructure formation.[16–19] The complexity of the conventional linear polymerisation derives from the underlying reaction scheme: typically, a polymer product forms due to interplay of many coupled chemical reactions.[11] Modelling of polymer networks is therefore notoriously difficult as networks are hard to deconstruct into separate chemical species.[10,11] LMWH based supramolecular hydrogels have a gel network that could be composed of 1-dimensional or crystalline structures with different interactions.[5,20–22]

Unlike polymeric networks, supramolecular networks are formed based on different mechanisms. The current understanding is that there are two main growth mechanisms that yield linear supramolecular fibres. The first, known as ***isodesmic growth***, occurs when the strength of interactions between monomers in the polymer chains is unaffected by the length of the chain. The second process known as ***nucleation-elongation*** — occurs in the growth of `ordered' supramolecular polymers, such as those that form helices. This involves two distinct phases of self-assembly: a slow nucleation phase followed by a more rapid

growth phase: once a stable nucleus is formed, further monomer addition becomes favourable and the polymer growth accelerates.

Gelation constitutes one more important point in which conventional polymers and supramolecular polymers are essentially different. Conventional polymer gels stem from hyper-branched polymers, cross-linked networks or inter-entangled systems of polymer rings, and in a specially designed system, formed from exclusively linear chains, whereas purely linear supramolecular polymers often exhibit a gel-like behaviour in experiments[23,24] We use the term supramolecular polymer to refer to a non-covalently former 1-D fibre chain reminiscent of a liner polymer chain. More over LMWH hydrogel networks as mentioned before can composed of 1-D fibres of crystalline structures. In our work on gelation kinetics and structure analysis for a pH-triggered supramolecular gelator, we have shown that dimensionality as represented by fractal dimension is varies with trigger concentration.[5] A more 1-D network fractality was obtained at lower trigger concentrations for a given gelator concentration. This means that by controlling the kinetics of gel formation, we could have scenarios whereas LWMH network could be represented as a linear supramolecular polymer which forms an entangled network forming a gel. In modelling polymeric systems, recently an approach has emerged which treats a polymer as an infinite graph with nodes or vertices used to represent the topology evolution during polymerization. [25] The model was later used to also understand transitions into gel regime with good agreement with results from stochastic Monte-Carlo simulations.[26] The model was later extended to hyperbranched polymers as well.[27] In all of these models, the approach has been to decouple kinetics of the chemical reactions from the topology formation. .[11,28–30] In this work, an early first attempt is made to model supramolecular gelation of LMWHs using a random graph model. The gel-like behaviour is attempted to be explained by introducing a network model with two types of reversible bonds: strong non-covalent bonds arising between monomers within the same chain, and weak inter-chain bonds that may temporarily associate separate chains into higher order clusters, or even, a fully connected network. Even if the random contacts between the chains are very short-lived, we show that as the length of the chains

increases with time, the total number of contacts becomes sufficient to keep the whole system dynamically connected. On the whole this work is an early attempt at a model for sparse supramolecular networks by combining the principles of dynamic and multiplex networks.[12,31]

In this work, we study a commonly reported low molecular weight hydrogelator, N-N'-Dibenzoyl-L-Cystine (DBC) (See Fig 1a) that forms supramolecular gel fibres in the presence of an acid (see Fig 1c).[21,32,33] For the acidification process, we chose the hydrolysis of Glucono-delta-lactone (GDL)(See Fig 1a.) since the reaction kinetics has already been well studied and reported and leads to a well-controlled and homogeneous acidification of the system[34,35]. In the rest of the paper, we introduce the modelling approach in three stages: Firstly, we identify all chemical species that are relevant to DBC-GDL gelation. Secondly, we develop and experimentally validate a reaction kinetic model that captures the concentration profiles for these species in DBC-GDL system. Thirdly, we apply the random graph concept and reconstruct global network properties from a given profile of network fragments. We then proceed to validating the gelation time with rheological measurements and discuss how the global properties of the network depend on the initially chosen model parameters, that is the concertation of DBC and weight fraction of GDL.

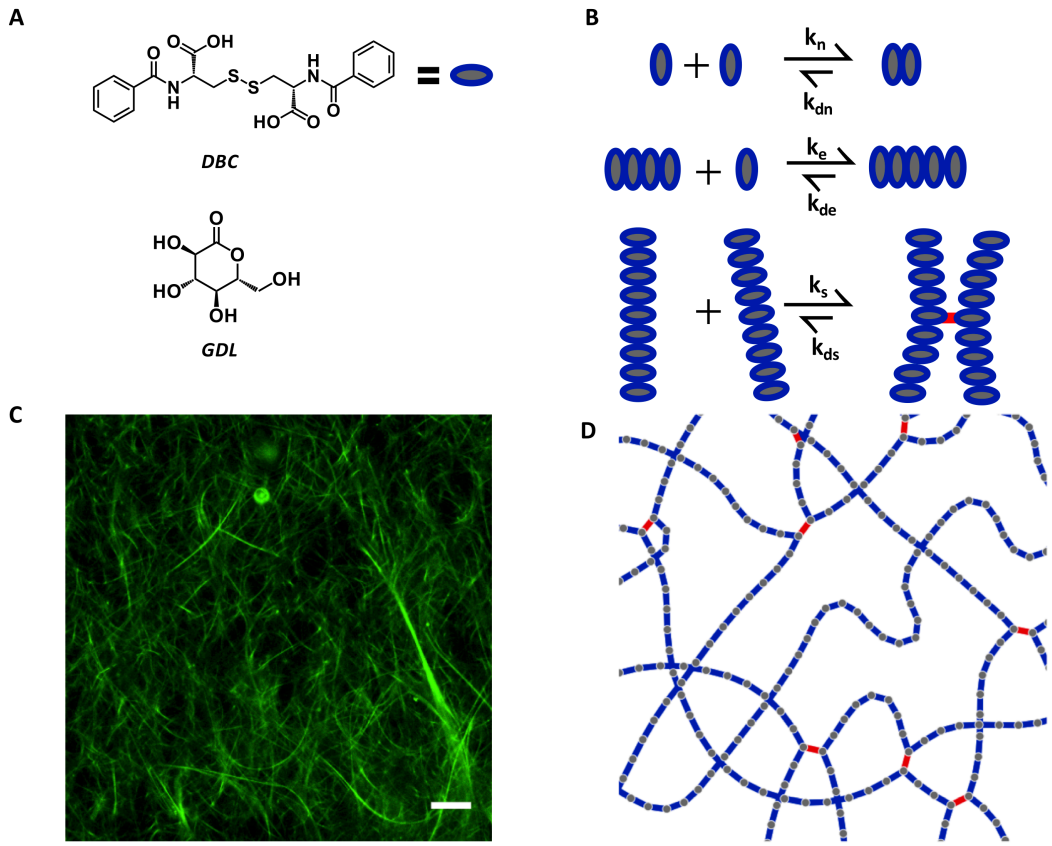

Figure 1. Molecular structure of N-N' Dibenzoyl-L-Cystine (DBC), supramolecular hydrogelator used in this study [A]; Structure of Glucono-δ-Lactone (GDL), acid trigger used in this study control gelation of DBC [A]; Schematic of the model involving nucleation, propagation and association (weak interaction) [B]; Confocal Laser Scanning Microscopy micrograph of DBC network ([DBC] = 20mM, [GDL] = 1 wt.%) [C]; Conceptual network topology obtained from monomer species as proposed in the model [D].

Figure 1B shows a depiction of a possible supramolecular polymerization and gelation of 1-D fibres from LMWHs. However, it is known that LWMHs gel networks consists of fibre bundles as observed in certain gelator systems through sophisticated visualization techniques such as stochastic reconstruction microscopy (STORM).[36] However it is very

challenging to model the bundling of fibres. In this early attempt, the bundling of fibres is considered a fast reaction and not rate-limiting.

3.2 Materials & Methods

3.2.1 Materials

Dibenzoyl-L-Cystine (DBC) (98%, Sigma Aldrich), Glucono-1,5-lactone (GDL) (99%, Alfa Aesar). Salt Na_2-DBC was prepared according to protocols published in earlier work[37]

3.2.2 Na_2-DBC protocol of preparation

Sodium Salt of the gelator was prepared by titrating acidified gelator against 0.1 M NaOH (1:2 molar ratio). The solution contained neutralized and non-neutralized was passed through an Acrodisc syringe filter (0.2 μm, PTFE membrane) to remove any possible impurities and non-neutralized gelator which was present as white precipitate in the solution. The resulting clear solution was checked for turbidity and freeze dried under vacuum to yield a white flaky powder which was used for further experiments.

3.2.3 pH measurements

3.2.3.1 GDL hydrolysis in the absence of gelator

pH measurements were carried out using a Metrohm 744 pH meter at 25°C after three-point calibration. A glass beaker filled with appropriate amount of demineralized water was placed on magnetic stirring plate and the pH probe was inserted. Accurate amounts of GDL were weighed and kept separately in folded papers. A magnetic stir bar was added and the water was kept under stirring. Care was taken to ensure that the stir bar was away from the probe since that would affect the measured pH value. The pH value prior to GDL addition was recorded. In a swift move, the GDL was transferred from the weighing paper into the beaker. An automated program (LabView, National Instruments) was used to record the value of pH every second. The measurements were carried out for a minimum of 8 hours till a maximum of 13 hours.

3.2.3.2 GDL hydrolysis in the presence of DBC

A 40mM stock of Na_2DBC solution was prepared by dissolving the appropriate amount of salt in demineralized water. Dilutions were prepared from this stock solution for all experiments. 1mL of Na_2DBC solution was transferred to a vial. A small magnetic stir bar was added. The solution was then placed on magnetic stir plate. Due to the small volumes of solutions, a minitrode, pH mini electrode (Hamilton Company) was used for the pH measurements. The pH mini electrode was gently immersed in the solution and kept at a safe distance from the rotating magnetic stirrer. The pH value prior to the addition of GDL was recorded. Accurate amounts of GDL were weighed and kept separately in folded papers. In a swift move, the GDL was transferred from the weighing paper into the vial. An automated program (LabView, National Instruments) was used to record the value of pH every second under stirring. The measurements were carried out for a minimum of 8 hours till a maximum of 13 hours.

3.2.4 Rheology

Oscillatory rheology measurements were performed using an AR-G2 strain-controlled rheometer (TA instruments) using a 40mm stainless steel plate-plate geometry. The temperature was maintained at 25 ± 0.2°C. Measured amounts of GDL were added to 1 mL of Na_2DBC solution of appropriate concentration, swiftly vortexed and cast on the bottom of the rheometer. The top plate was already lowered very close to the bottom plate so as to prevent delay in setup time. Once the solution is cast, the plate is further lowered to entrap it between the two plates. Once the solution was entrapped between the two plates with no air bubbles, a solvent trap filled with water or hexadecane was placed to prevent drying. Time sweep measurements were carried out at 1 Hz and 0.05% strain.

3.3 Results & Discussion

3.3.1 The Model

Firstly, we consider a reaction kinetic model for all chemical species that are relevant to DBC-GDL gelation. These species include low molecular species: water, hydroxide, GDL, gluconic

acid, etc., but also, specially designed species that characterise the network of weakly interacting chains: depending on where a monomer appears in the fibre network, we will refer to it as to a different species, see Figure 1b,d. Namely, we distinguish between free monomers M_0, nucleus N, monomers that are at the end of a chain $M_{1,0}$ (i.e. having one strongly bonded neighbour), monomers that are in the middle of a chain $M_{2,0}$ (i.e. having two strongly bonded neighbours), and monomers that are in the middle of a chain and are also weakly interacting with another chain $M_{2,1}$ (having two strongly bonded neighbours and a weakly bonded one). The rate equations for the low molecular species are given in supplementary information. The following tables summarizes the participating reactions in the supramolecular gelation model and the DBC-GDL system respectively.

Table 1. Participating reactions in the supramolecular gelation model

Mechanism	Reaction	Tag
Nucleation	$M_0 + M_0 \underset{k_{dn}}{\overset{k_n}{\rightleftharpoons}} N$	E1
Elongation	$M_0 + N \underset{k_d}{\overset{k_a}{\rightleftharpoons}} M_{10} + M_{20}$ $M_{10} + M_0 \underset{k_d}{\overset{k_a}{\rightleftharpoons}} M_{10} + M_{20}$	E2a, E2b
Weak interaction	$M_{20} + M_{20} \underset{k_{ds}}{\overset{k_s}{\rightleftharpoons}} 2M_{21}$	E3
Mass Balance	$M = M_{00} + 2N + M_{10} + M_{20} + M_{21}$	E4

Table 2. Reactions participating in the gelation of DBC in the presence of GDL.

Equation	Rate expression	Rate constant values	Tag
$H_2O \underset{k_{-1}}{\overset{k_1}{\rightleftharpoons}} H^+ + OH^-$	$R_1=k_1$ $R_{-1}=k_{-1}[H^+][OH^-]$	$k_1 = 1 \times 10^{-3}\ Ms^{-1}$ [27] $k_{-1} = 1 \times 10^{11} M^{-1}s^{-1}$	E5
$GDL \underset{k_{-2}}{\overset{k_2}{\rightleftharpoons}} GA$	$R_2 =$ $(k_2+k_H[H^+])[GDL]$ $R_{-2}= k_{-2}[GA]$	$k2 = 4 \times 10^{-5}\ s^{-1}$ [*] $k_H = 4.7 \times 10^{-2}\ M^{-1}s^{-1}$ [28,29] $k_{-2} = 8 \times 10^{-6}\ s^{-1}$	E6
$GA \underset{k_{-3}}{\overset{k_3}{\rightleftharpoons}} G^- + H^+$	$R_3=k_3[GA]$ $R_{-3}=k_{-3}[G^-][H^+]$	$k_3 = 2.5 \times 10^2\ s^{-1}$ $k_{-3} = 1 \times 10^6\ M^{-1}s^{-1}$ [28,29]	E7
$DBC^{2-} + 2H^+ \underset{k_{-4}}{\overset{k_4}{\rightleftharpoons}} DBCH_2$	$R_4 = k_4\ [DBC^{2-}][H^+]^2$ $R_{-4} = k_{-4}[DBCH_2]$	$k_4 = 1 \times 10^6\ M^{-1}s^{-1}$ [**] $K_4 = k_4/k_{-4} = 3.16 \times 10^4$ [27] $k_{-4} = 31.645\ M^{-1}s^{-1}$	E8

The rate equations for the network species are designed in accordance with nucleation-elongation mechanism. Figure 1b illustrates how the standard nucleation-elongation steps (Equations E1 and E2 in Table 1) is combined with a reaction step allowing a weak interaction between chains, Equation E3 in Table 1. All the reactions have conventional rates, with the only exception of the reverse reactions in reaction E2b, in which the rates are proportional to:

$$r_1(t) = \frac{\left[\mathrm{M}_{10}\right]_t}{2\left[\mathrm{M}_{20}\right]_t + \left[\mathrm{M}_{10}\right]_t} \quad \text{(E9)}$$

$$r_2(t) = \frac{\left[\mathrm{M}_{20}\right]_t}{2\left[\mathrm{M}_{20}\right]_t + \left[\mathrm{M}_{10}\right]_t} \quad \text{(E10)}$$

$$r_1(t)+r_2(t)=1 \tag{E11}$$

Here, factors r_2, r_1 are the probabilities that a terminal unit, $\mathrm{M}_{1,0}$ is preceded by respectively N or $\mathrm{M}_{2,0}$ Therefore, the reaction mechanism as presented in Table 1, corresponds to the following system of ordinary differential equations written for the network species:

$$\frac{d}{dt}\left[\mathrm{M}_0\right]_t = k_4\left[\mathrm{DBC}^{2-}\right]_t\left[\mathrm{H}^+\right]_t^2 - k_{-4}\left[\mathrm{M}_0\right]_t - k_n\left[\mathrm{M}_0\right]_t^2 + k_{dn}\left[\mathrm{N}\right] - k_a\left[\mathrm{M}_0\right]\left[\mathrm{N}\right] + r_2 k_d\left[\mathrm{M}_{10}\right]^2\left[\mathrm{M}_{20}\right] - k_a\left[\mathrm{M}_{10}\right]\left[\mathrm{M}_0\right] + k_d\left[\mathrm{M}_{10}\right]\left[\mathrm{M}_{20}\right] \tag{E12}$$

$$\frac{d}{dt}[\mathrm{N}]_t = k_n\left[\mathrm{M}_0\right]_t^2 - k_{dn}[\mathrm{N}]_t - k_a[\mathrm{N}]_t\left[\mathrm{M}_0\right]_t + k_d r_1(t)\left[M_{10}\right]_t \tag{E13}$$

$$\frac{d}{dt}\left[\mathrm{M}_{10}\right]_t = k_a\left[\mathrm{N}\right]_t\left[\mathrm{M}_0\right]_t - k_d r_1(t)\left[M_{10}\right]_t \tag{E14}$$

$$\frac{d}{dt}\left[\mathrm{M}_{20}\right]_t = k_a\left[\mathrm{M}_{10}\right]_t\left[\mathrm{M}_0\right]_t - 2k_s\left[\mathrm{M}_{20}\right]_t^2 + k_u\left[\mathrm{M}_{21}\right]_t - k_d r_2(t)\left[\mathrm{M}_{10}\right]_t \tag{E15}$$

$$\frac{d}{dt}\left[\mathrm{M}_{21}\right]_t = 2k_s\left[\mathrm{M}_{20}\right]_t^2 - k_u\left[\mathrm{M}_{21}\right]_t \tag{E16}$$

Having concentration of species, and allows one to compute various properties of the network topology by treating these concentrations as the degree distribution of a random graph. Note that this random graph has two types of edges, and therefore, it is a bi-coloured graph or a so called two-layer multiplex network.

3.3.2 Distance between crossing points

Having concentration of species M_{10}, M_{20} and M_{21} allows one to compute the probability that a chain contains a sequence with a given pattern.[38] Suppose one chooses a M_{21} monomer at random. The probability p that the monomer next to it in the chain is M_{20} and the probability q that the next monomer is M_{21} are given by

$$p = \frac{2[\mathrm{M}_{20}]}{[\mathrm{M}_{10}] + 2[\mathrm{M}_{20}] + 2[\mathrm{M}_{21}]} \tag{E17}$$

$$q = \frac{2[\mathrm{M}_{21}]}{[\mathrm{M}_{10}] + 2[\mathrm{M}_{20}] + 2[\mathrm{M}_{21}]} \tag{E18}$$

Here the weight 2 indicates the intrachain functionality of the monomer species. By iterating this reasoning one obtains the probability that an n-monomer sequence of M_{20} is followed by M_{21} as a geometric distribution $p^n q$. Hence, the expected number of consecutive M_{20} monomers between two M_{21} is given by:

$$E[n] = \sum_{n=0}^{\infty} n p^n q = \frac{qp}{(p-1)^2} = \frac{4[\mathrm{M}_{21}][\mathrm{M}_{20}]}{([\mathrm{M}_{10}] + 2[\mathrm{M}_{21}])^2}. \tag{E19}$$

3.3.3 Phase Transition

As follows from the results on random coloured (coloured meaning that there are different type of interacting monomers) networks[12] that the network percolates if

$$\mu_{11}^2(t) - 4\mu_{01}(t)\mu_{10}(t) + 2\mu_{02}(t)\mu_{10}(t) + 2\mu_{01}(t)\mu_{20}(t) - \mu_{02}(t)\mu_{20}(t) > 0 \tag{E20}$$

where $\mu_{i,j}$ are moments of the degree distribution of the underlying random graph. In this work, the moments at time t are derived from the concentrations of the different monomer species:

$$\mu_{11}(t) = [M_{2,1}]_t \tag{E21}$$

$$\mu_{01}(t) = [M_{2,1}]_t \tag{E22}$$

$$\mu_{10}(t) = [M_{1,0}]_t + 2[M_{2,0}]_t + 2[M_{2,1}]_t \tag{E23}$$

$$\mu_{02}(t) = [M_{2,1}]_t \tag{E24}$$

$$\mu_{20}(t) = [M_{1,0}]_t + 4[M_{2,0}]_t + 4[M_{2,1}]_t \tag{E25}$$

By substituting (E23) into (E20) one obtains:

$$4[M_{21}]_t > [M_{10}]_t. \tag{E26}$$

Initially, when all the chains are linear, the concentration of M_{21} is much smaller then M_{10} and therefore, the criterion (E26) does not hold. This means that the system is below the critical or percolation threshold concentration. Therefore, from the modelling perspective, the gel point is defined as time $t = t_{\mathrm{gel,m}}$ at which

$$4[M_{21}]_t - [M_{10}]_t = 0 \qquad \text{(E27)}$$

3.3.4 DBC – GDL Reaction Scheme

The following is the set of participating reactions with the corresponding rate constants.

Table 3. Reactions participating in the gelation of DBC in the presence of GDL.

Equation	Rate expression	Rate constant values
$H_2O \underset{k_{-1}}{\overset{k_1}{\rightleftharpoons}} H^+ + OH^-$	$R_1=k_1$ $R_{-1}=k_{-1}[H^+][OH^-]$	$k_1 = 1 \times 10^{-3}\ Ms^{-1}$ [27] $k_{-1} = 1 \times 10^{11} M^{-1}s^{-1}$
$GDL \underset{k_{-2}}{\overset{k_2}{\rightleftharpoons}} GA$	$R_2 = (k_2+k_H[H^+])[GDL]$ $R_{-2}= k_{-2}[GA]$	$k2 = 4 \times 10^{-5}\ s^{-1}$ [*] $k_H = 4.7 \times 10^{-2}\ M^{-1}s^{-1}$ [28,29] $k_{-2} = 8 \times 10^{-6}\ s^{-1}$
$GA \underset{k_{-3}}{\overset{k_3}{\rightleftharpoons}} G^- + H^+$	$R_3=k_3[GA]$ $R_{-3}=k_{-3}[G^-][H^+]$	$k_3 = 2.5 \times 10^2\ s^{-1}$ $k_{-3} = 1 \times 10^6\ M^{-1}s^{-1}$ [28,29]
$DBC^{2-} + 2H^+ \underset{k_{-4}}{\overset{k_4}{\rightleftharpoons}} DBCH_2$	$R_4 = k_4\,[DBC^{2-}][H^+]^2$ $R_{-4} = k_{-4}[DBCH_2]$	$k_4 = 1 \times 10^6\ M^{-1}s^{-1}$ [**] $K_4 = k_4/k_{-4} = 3.16 \times 10^4$ [27] $k_{-4} = 31.645\ M^{-1}s^{-1}$

Rate constants form literature are referenced. The rate constants marked with asterisks were found by fitting the model to the pH profiles in the pure GDL system [*] and GDL-DBC system [**].

3.3.5 pH kinetics due to GDL hydrolysis

First, we investigated the hydrolysis of GDL in the absence of the LMWG DBC. GDL is a known acidifier and has been extensively used in the studies to control gelation of food and soft materials.[39–42]The dissolution of GDL is faster than its hydrolysis and hence effects a gradual pH change in the system. GDL hydrolyses to form gluconic acid. It is known that GDL hydrolysis kinetics is affected by the nature of solvent (acidic, alkaline, neutral).[43–45] Since the solutions were prepared in demineralized water which has a pH < 7 due to presence of dissolved carbon dioxide, the hydrolysis kinetic expressions that take into the presence of acid was used in modelling the reactions. The reaction equations and corresponding rate expressions are given in Table 2. Figure 2 shows the pH drop in the GDL solution due to hydrolysis as function of GDL concentration. Initially, the pH drops very rapidly (inset) followed by a gradual change (time > 1-5 min) which equilibrates after 8 hours. To be thorough, the pH was monitored for up to 13 hours, but no significant change was observed after 8 hours. With increase in the GDL concentration, two noticeable effects occur: the rate of pH drop increases and the end pH decreases. This is due to the accelerated forward reaction (as seen from the rate expressions) and higher equilibrium concentration of gluconic acid. It can be seen from Figure 2 that the mode predictions (solid line) are in agreement with experimental data (open symbols). The final rate constants for the low molecular species model were obtained after optimization as shown in Table 2.

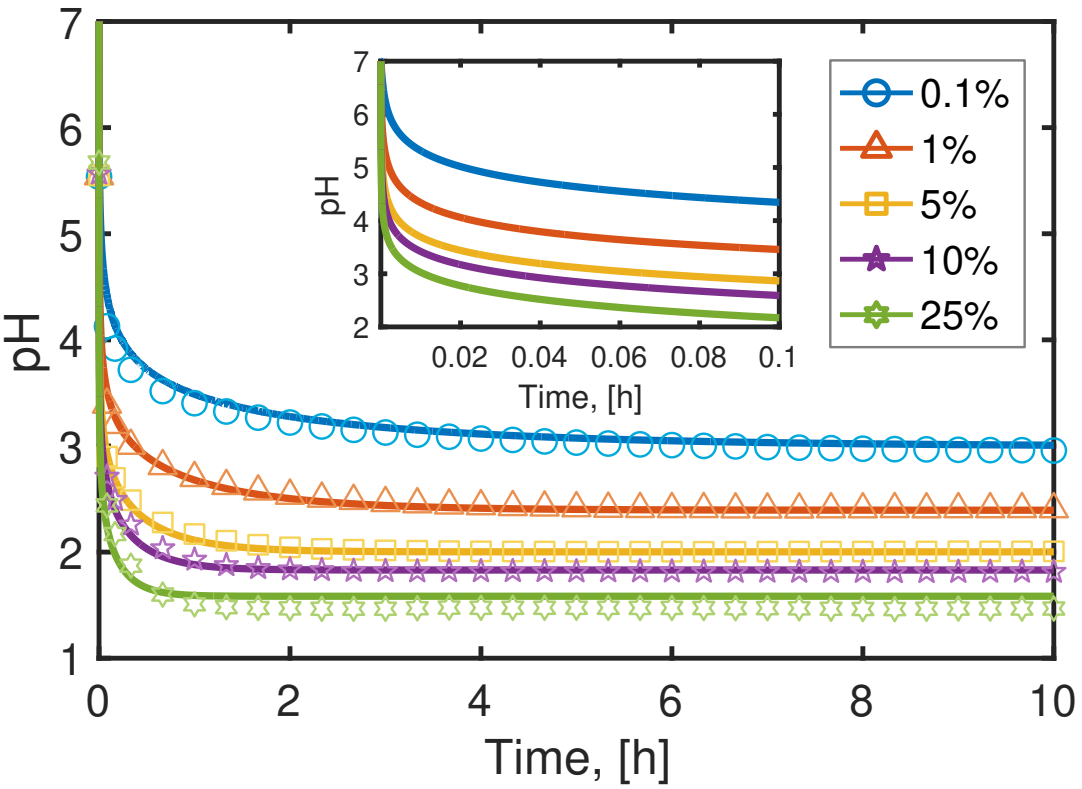

Figure 2. Experimental data (symbols) and model (solid lines) for hydrolysis of pure GDL at different concentrations. The inset zooms in to emphasise how rapid is the initial drop of pH.

3.3.6 pH kinetics in the presence of DBC

Following the good agreement of experimental data with model predictions for pH, we investigated the pH-kinetics of GDL hydrolysis in the presence of DBC. It is known Once pH drops below pK_a of DBC fibre, network formation and eventually gelation begins to occur. The experiments were setup in the manner described in the experimental section and graphs that show variation of pH over time were obtained. Figures 3A – 3D shows the variation in pH profiles at different GDL concentrations. It follows from the results that the model prediction resembles the experimental data. The pH profiles for other concentrations can be found in the supporting information (see Appendix).

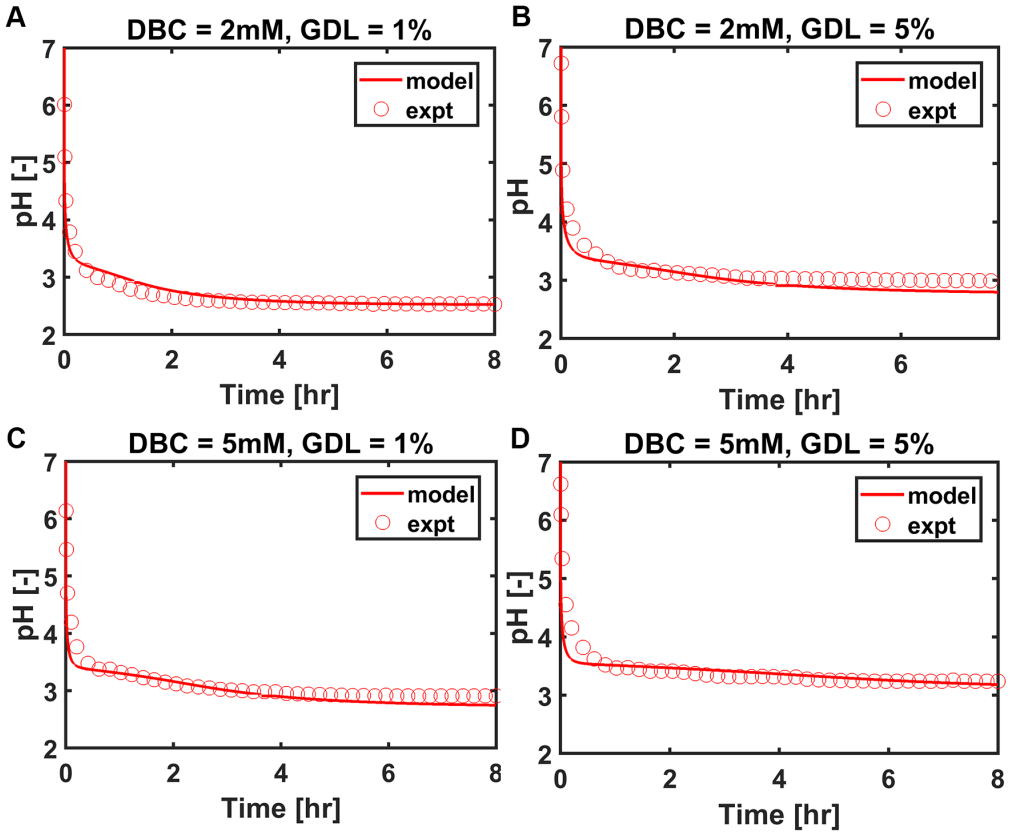

Figure 3. Experimental data (red open circles) and model (red solid lines) pH kinetics of the DBC – GDL system at different concentrations, A) [DBC] = 2mM, [GDL] = 1%; B) [DBC] = 2mM, [GDL] = 5%; C) [DBC] =5mM, [GDL] = 1%; D) [DBC] = 5mM, [GDL] = 5%. GDL % are in wt.%.

3.3.7 Model prediction of gel fraction and gelation times

Having optimized the reaction rate constants for the hydrolysis of GDL and formation of the protonated gelator from the deprotonated precursor, the next step was inclusion of nucleation, elongation and weak interactions. This would account for the formation of gel from the protonated gelator monomer. Dynamic viscosity was measured in order to experimentally track the gelation process. This technique has proven to be successful in characterization of pH-triggered supramolecular gels. One of the parameters associated with gelation is the gelation time, which can be experimentally defined as the time when storage (G') modulus is greater than loss modulus (G''). This definition has been used

without much dispute over the years. In our work, we used this definition in order to obtain experimental gelation times. Figure 4B shows the method employed to obtain gelation time from rheological data. It can be seen that there is a moment when there is sudden increase in storage modulus. This abrupt change was also observed in the modelled gel fractions (Figure 4c) respectively. Figure 4d presents a colormap for gelation times for various combinations DBC and GDL concentrations. The black zone indicates the region where there is no gel, which indicates short segments/fibres which are part of the sol. To evaluate the model, experimental gelation times were compared with model predicted values for four concentrations of DBC as shown in Fig. 5. The experiments were done in triplicate to capture experimental error. It can be seen that the model is in agreement with the experimental data. The deviations between experimental trials may be the result of experimental errors involved in sample weighing, solution preparation, casting and measuring the rheometer plates.

Table 3. Rate constant values for the participating reactions in supramolecular gelation

Mechanism	Reaction	Tag	Values
Nucleation	$M_0 + M_0 \underset{k_{dn}}{\overset{k_n}{\rightleftharpoons}} N$	E1	k_n=10.59 k_{-dn} = 8.33 x 10^{-6}
Elongation of N	$M_0 + N \underset{k_d}{\overset{k_a}{\rightleftharpoons}} M_{10} + M_{20}$ $M_{10} + M_0 \underset{k_d}{\overset{k_a}{\rightleftharpoons}} M_{10} + M_{20}$	E2	K_a = 3.2 x 10^5 k_d < 1 x 10^{-20}
Weak interaction	$M_{20} + M_{20} \underset{k_{ds}}{\overset{k_s}{\rightleftharpoons}} 2M_{21}$	E3	k_s = 177.83 k_{ds} =9.64 x 10^3

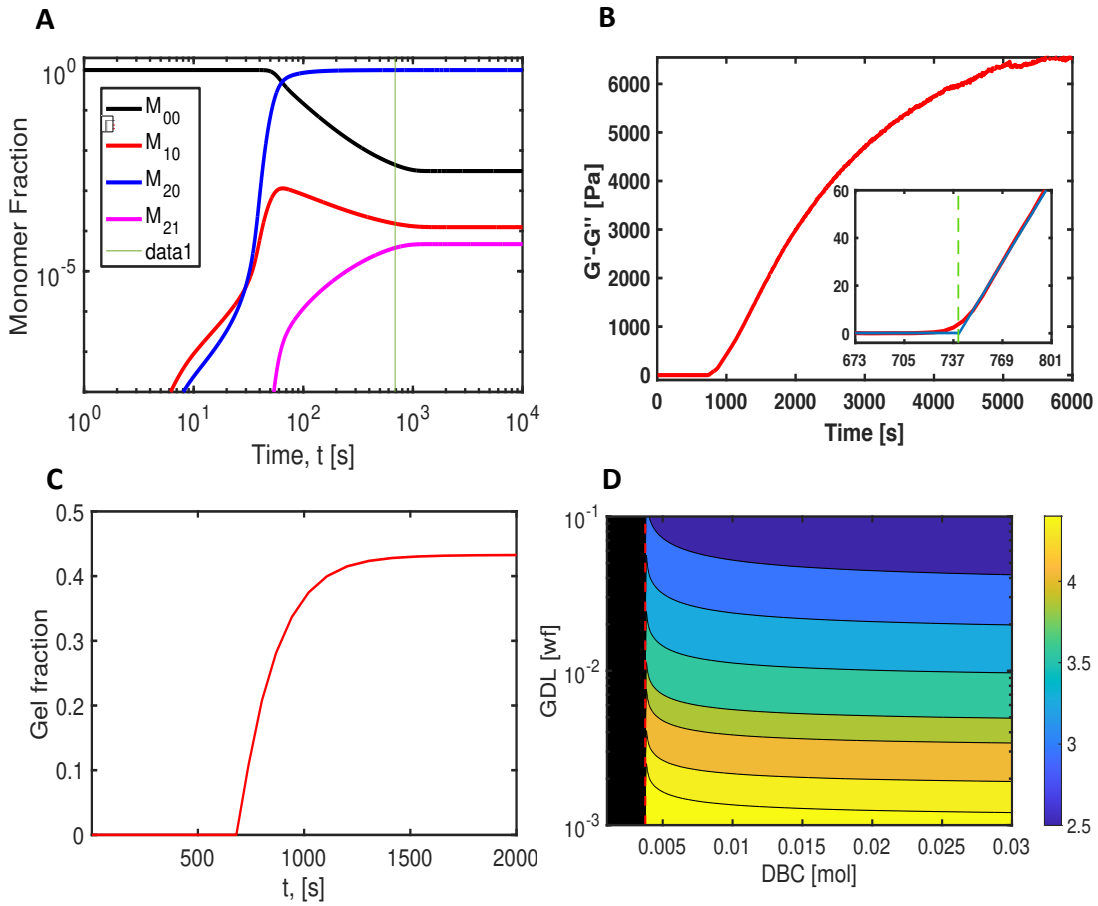

Figure 4. (A) Evolution of monomer species in time as produced by the model for DBC= 0.002M, and weight fraction of GDL 1%. The dashed guideline indicates the critical point. (B) The slope of experimentally measured time series for G'-G'' for the same conditions as in (A) is analysed with change-point detection algorithm to retrieve the moment in time at which gelation starts, i.e., G' starts to exceed G". *Inset*: a zoom in around the critical point shows a discontinuous change of the slope. The gel fraction as predicted by the model (C) passes through second order phase transition at the same time point as the divergence of G'-G'' in (B). (D) The gelation time strongly depends on the concentrations of both GDL and DBC. The black region in (D) indicates the domain where the system equilibrates without reaching the stage of gelation.

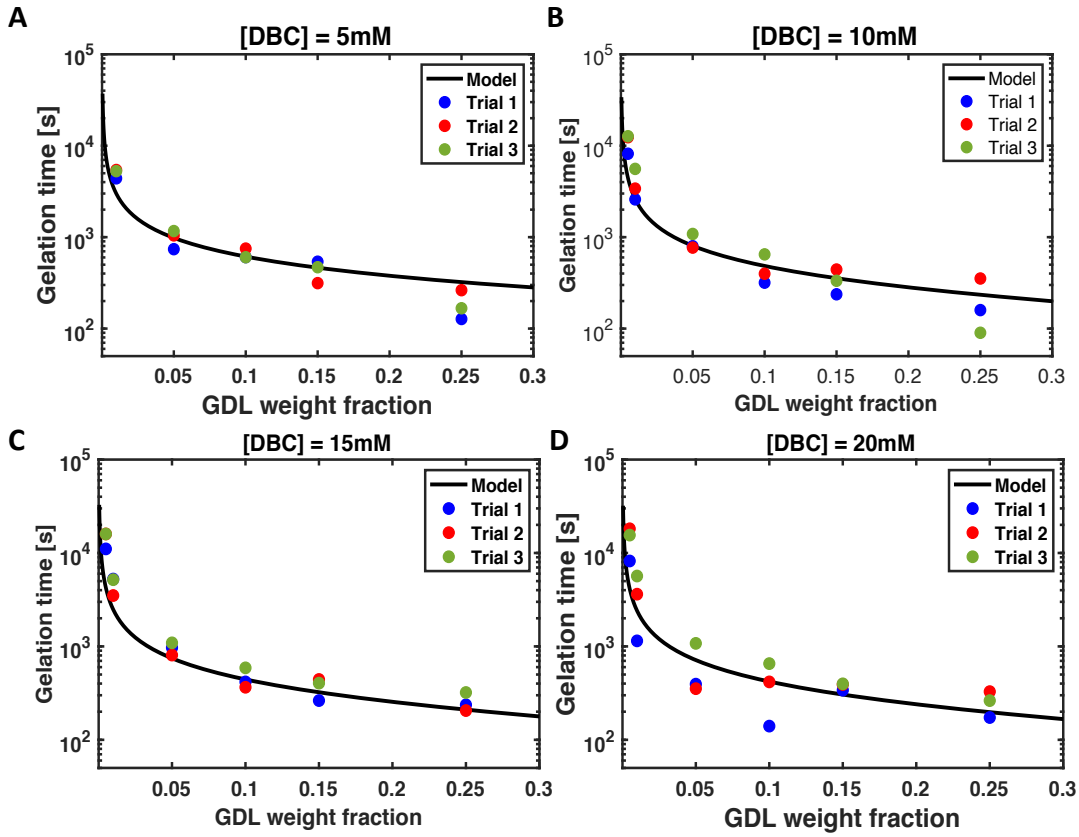

Figure 5. The time until the onset of gelation as predicted by the model [black solid line] is compared with experimental values from three independent trials [blue – trial 1, red – trial 2, green – trial 3] and four different DBC concentrations [A – 5mM, B – 10mM, C – 15mM, D – 20mM].

3.3.8 Model parameter space

A mathematical model for supramolecular gelation allows one, with relatively small efforts, to scan through the whole parameter space and find the combinations of optimal concentrations of DBC/GDL that suit various purposes. In this work the parameters that can be independently controlled are the initial concentrations of DBC and the weight fraction of GDL, as these two quantities are free to be chosen by the designer of the experiment. As shown in Fig. 4d, one has a control over the time it takes to form gel, wherein larger concentrations of both, GDL and DBC, promote faster gelation with GDL being the dominant

factor. Some combinations of the initial concentrations of GDL and DBC do not lead to gelation at all. In fact, the parameter space is partitioned by a line of critical points:

$$[DBC]_{critical} = 0.055 f_{GDL}^{0.2}$$

where f_{GDL} denotes the initial weight fraction of GDL. Therefore, the critical gelator concentration $[DBC]_{critical}$ is not constant but features a weak dependence on the weight fraction of GDL, which is indicated by a small fractional exponent: 0.20. The pre-exponential factor and exponent were obtained from the model when fitted with experimental data from pH and rheology measurements.

The equilibrium, as shown in Fig. 6a, typically occurs an order of magnitude in time later then gelation, and, as shown in Fig. 6b, the equilibrium gel fraction may settle anywhere between 0 and 100%. The precise gel fraction at equilibrium is predominantly defined by the initial concentration of DBC. If this value is lower than $[DBC]_{critical}$ gelation does not occur at all, and we observe second-order phase transition at $[DBC]_{critical}$ having critical exponent 1, see Fig. 6d. The mathematical model also gives insight into the internal structure of the gel. The density of the fibber network as measured by the expected distance between contact points, see Fig. 6c, depends on concentrations of DBC and GDL, with GDL capable to significantly manipulate the network density. The later relationship may be exploited for designing supramolecular fibre gels with desired elastic properties.

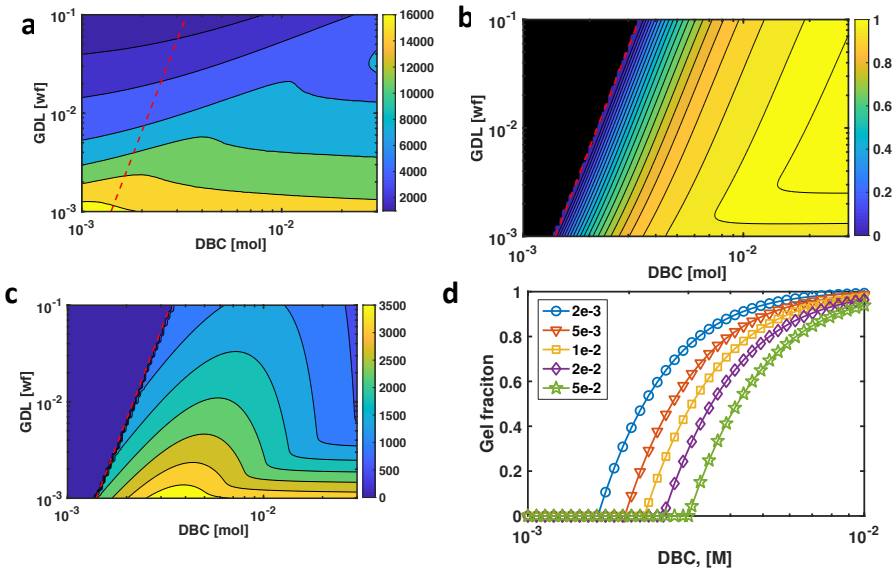

Figure 6. Parameter space in terms of DBC/GDL concentrations. The time (seconds) until equilibration (a), the equilibrium gel fraction (b), and the density of the network as measured by number of units between points of contact between fibres (c) all depend on the initial concentrations of DBC and GDL. (d) The gel fraction at the equilibrium exhibits the second order phase transition having critical exponent 1, as discussed in Supplementary Materials. The weight fraction of GDL is indicated in the legend. The dashed line in (a, b ,c) indicates these critical points in the parameter space.

3.3.9 Conclusions

In this work we have showed that a random graph network model can be used to predict macroscopic properties, such as gelation time, of supramolecular gels produced by the self-assembly of low molecular weight hydrogelators from initial concentrations of the gelator and the triggering agent. Importantly our network model requires two types of connections, which means that, unlike conventional gels, the soft matter networks have the multiplex structure. The DBC – GDL system has proven to be a good model system to validate this model with fair agreement between model predicted values for pH and gelation time and experimental data. This model can be implemented by researchers in academia and industry after adjusting for the kinetics involved in their system to rapidly screen formulations while developing applications for drug delivery, tissue engineering, cell culturing.[46]

References

[1] V. Le Sage, V. Lakshminarayanan, E. Mendes, R. Eelkema, J. Van Esch, *Chim. Oggi/Chemistry Today* **2014**, *32*.

[2] E. R. Draper, D. J. Adams, *Chem* **2017**, *3*, 390–410.

[3] D. J. Adams, M. F. Butler, W. J. Frith, M. Kirkland, L. Mullen, P. Sanderson, *Soft Matter* **2009**, *5*, 1856.

[4] A. Z. Cardoso, A. E. Alvarez Alvarez, B. N. Cattoz, P. C. Griffiths, S. M. King, W. J. Frith, D. J. Adams, *Faraday Discuss.* **2013**, *166*, 101–116.

[5] V. Lakshminarayanan, C. Chockalingam, E. Mendes, J. H. van Esch, *ChemPhysChem* **2021**, DOI 10.1002/CPHC.202100276.

[6] S. M. Hashemnejad, M. M. Huda, N. Rai, S. Kundu, *ACS Omega* **2017**, *2*, 1864–1874.

[7] R. Van Lommel, L. A. J. Rutgeerts, W. M. De Borggraeve, F. De Proft, M. Alonso, *Chempluschem* **2020**, *85*, 267–276.

[8] J. K. Gupta, D. J. Adams, N. G. Berry, *Chem. Sci.* **2016**, *7*, 4713–4719.

[9] R. Van Lommel, J. Zhao, W. M. De Borggraeve, F. De Proft, M. Alonso, *Chem. Sci.* **2020**, *11*, 4226–4238.

[10] I. Kryven, J. Duivenvoorden, J. Hermans, P. D. Iedema, *Macromol. Theory Simulations* **2016**, *25*, 449–465.

[11] Y. Orlova, I. Kryven, P. D. Iedema, *Comput. Chem. Eng.* **2018**, *112*, 37–47.

[12] I. Kryven, *Nat. Commun.* **2019**, *10*, 404.

[13] F. Oosawa, M. Kasai, *J. Mol. Biol.* **1962**, *4*, 10–21.

[14] T. P. J. Knowles, C. A. Waudby, G. L. Devlin, S. I. A. Cohen, A. Aguzzi, M. Vendruscolo, E. M. Terentjev, M. E. Welland, C. M. Dobson, *Science* **2009**, *326*, 1533–7.

[15] L. Nicoud, S. Lazzari, D. Balderas Barragán, M. Morbidelli, *J. Phys. Chem. B* **2015**, *119*, 4644–4652.

[16] N. Javid, S. Roy, M. Zelzer, Z. Yang, J. Sefcik, R. V. Ulijn, *Biomacromolecules* **2013**, *14*, 4368–4376.

[17] I. Kryven, S. Lazzari, G. Storti, *Macromol. Theory Simulations* **2014**, *23*, 170–181.

[18] S. Lazzari, L. Nicoud, B. Jaquet, M. Lattuada, M. Morbidelli, *Adv. Colloid Interface Sci.* **2016**, *235*, 1–13.

[19] A. R. Hirst, I. A. Coates, T. R. Boucheteau, J. F. Miravet, B. Escuder, V. Castelletto, I. W. Hamley, D. K. Smith, *J. Am. Chem. Soc.* **2008**, *130*, 9113–9121.

[20] K. A. Houton, K. L. Morris, L. Chen, M. Schmidtmann, J. T. A. Jones, L. C. Serpell, G. O. Lloyd, D. J. Adams, *Langmuir* **2012**, *28*, 9797–9806.

[21] F. M. Menger, Y. Yamasaki, K. K. Catlin, T. Nishimi, *Angew. Chemie Int. Ed. English* **1995**, *34*, 585–586.

[22] F. M. Menger, K. L. Caran, *J. Am. Chem. Soc.* **2000**, *122*, 11679–11691.

[23] J. Boekhoven, J. M. Poolman, C. Maity, F. Li, L. Van Der Mee, C. B. Minkenberg, E. Mendes, J. H. Van Esch, R. Eelkema, *Nat. Chem.* **2013**, *5*, 433–437.

[24] R. K. Das, V. Gocheva, R. Hammink, O. F. Zouani, A. E. Rowan, *Nat Mater* **2015**, *advance on*, DOI 10.1038/nmat4483.

[25] I. Kryven, P. D. Iedema, *Macromol. Theory Simulations* **2014**, *23*, 7–14.

[26] I. Kryven, P. D. Iedema, *Chem. Eng. Sci.* **2015**, *126*, 296–308.

[27] I. Kryven, P. D. Iedema, *Polymer (Guildf).* **2013**, *54*, 3472–3484.

[28] I. Kryven, *Phys. Rev. E* **2016**, *94*, 012315.

[29] V. Schamboeck, I. Kryven, P. D. Iedema, *Macromol. Theory Simulations* **2017**, *26*, 1700047.

[30] I. Kryven, *J. Math. Chem.* **2018**, *56*, 140–157.

[31] V. Schamboeck, P. D. Iedema, I. Kryven, *Sci. Rep.* **2019**, *9*, 2276.

[32] F. M. Menger, K. L. Caran, *J. Am. Chem. Soc.* **2000**, *122*, 11679–11691.

[33] J. P. Wojciechowski, A. D. Martin, P. Thordarson, *J. Am. Chem. Soc.* **2018**, *140*, 2869–2874.

[34] K. Kovacs, R. E. McIlwaine, S. K. Scott, A. F. Taylor, *J. Phys. Chem. A* **2007**, *111*, 549–551.

[35] S. K. S. and A. F. T. Klara Kovacs, Rachel E. McIlwaine, “pH oscillations and bistability in the methylene glycol–sulfite–gluconolactone reaction,” DOI

10.1039/b704407kcan be found under http://www1.chem.leeds.ac.uk/AFT/pdf/PCCP.pdf, **2007**.

[36] H. Cox, P. Georgiades, H. Xu, T. A. Waigh, J. R. Lu, *Biomacromolecules* **2017**, *18*, 3481–3491.

[37] V. Lakshminarayanan, L. Poltorak, D. Bosma, E. J. Sudholter, J. van Esch, E. Mendes, *Chem. Commun.* **2019**, DOI 10.1039/C9CC04238E.

[38] I. Kryven, Y. R. Zhao, K. B. McAuley, P. Iedema, *Chem. Eng. Sci.* **2018**, *177*, 491–500.

[39] D. J. Adams, M. F. Butler, W. J. Frith, M. Kirkland, L. Mullen, P. Sanderson, *Soft Matter* **2009**, *5*, 1856.

[40] E. R. Draper, L. L. E. Mears, A. M. Castilla, S. M. King, T. O. McDonald, R. Akhtar, D. J. Adams, *RSC Adv.* **2015**, *5*, 95369–95378.

[41] V. Chardot, S. Banon, M. Misiuwianiec, J. Hardy, *J. Dairy Sci.* **2010**, *85*, 8–14.

[42] D. J. Cornwell, O. J. Daubney, D. K. Smith, *Stoch. Process. their Appl.* **2016**, *126*, 337–359.

[43] D. T. Sawyer, J. B. Bagger, *J. Am. Chem. Soc.* **1959**, *81*, 5302–5306.

[44] Y. Pocker, E. Green, *J. Am. Chem. Soc.* **1973**, *95*, 113–119.

[45] Y. Pocker, E. Green, *J. Am. Chem. Soc.* **1974**, *96*, 166–173.

[46] V. Le Sage, V. Lakshminarayanan, E. Mendes, R. Eelkema, J. Van Esch, *Chim. Oggi/Chemistry Today* **2014**, *32*, 62–66.

Appendix – Supporting Information

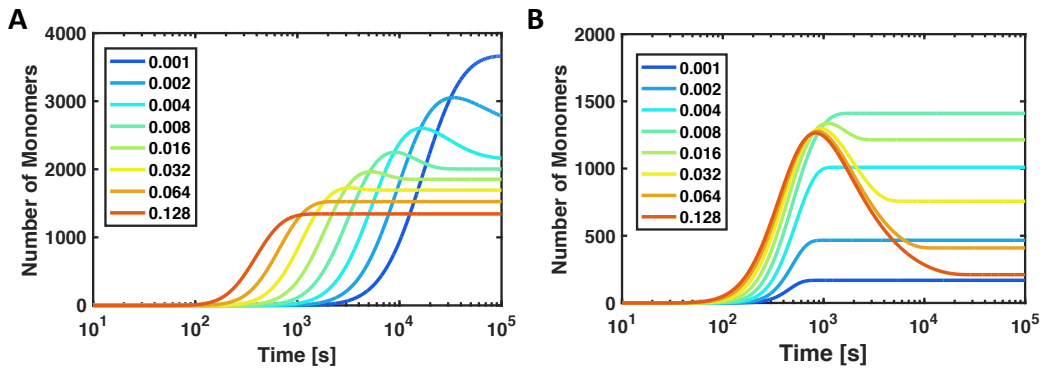

Figure S1. The number of units between contact points for weight fraction of GDL (0.1 wt.%) and DBC varying as indicated in the legend. (B) Number of units between contact points for [DBC] = 1mM and the weight fraction of GDL varying as indicated in the legend.

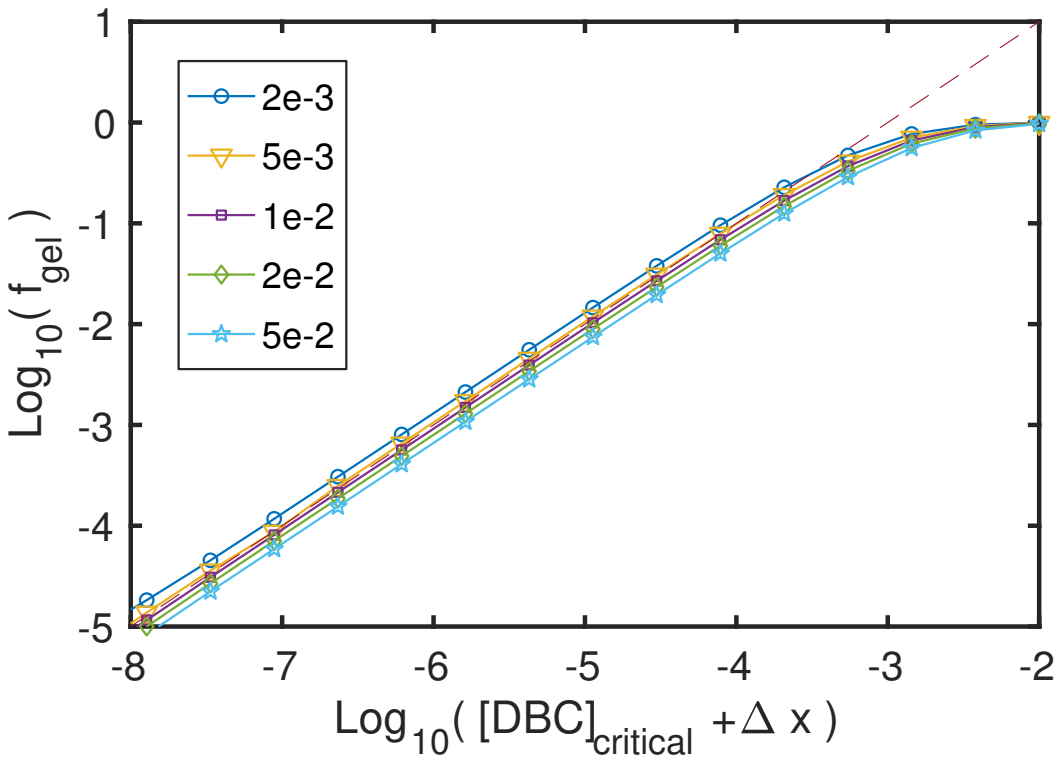

Figure S2. The critical exponents at the phase transition for several weight fractions of GDL, as indicated in the legend, is one

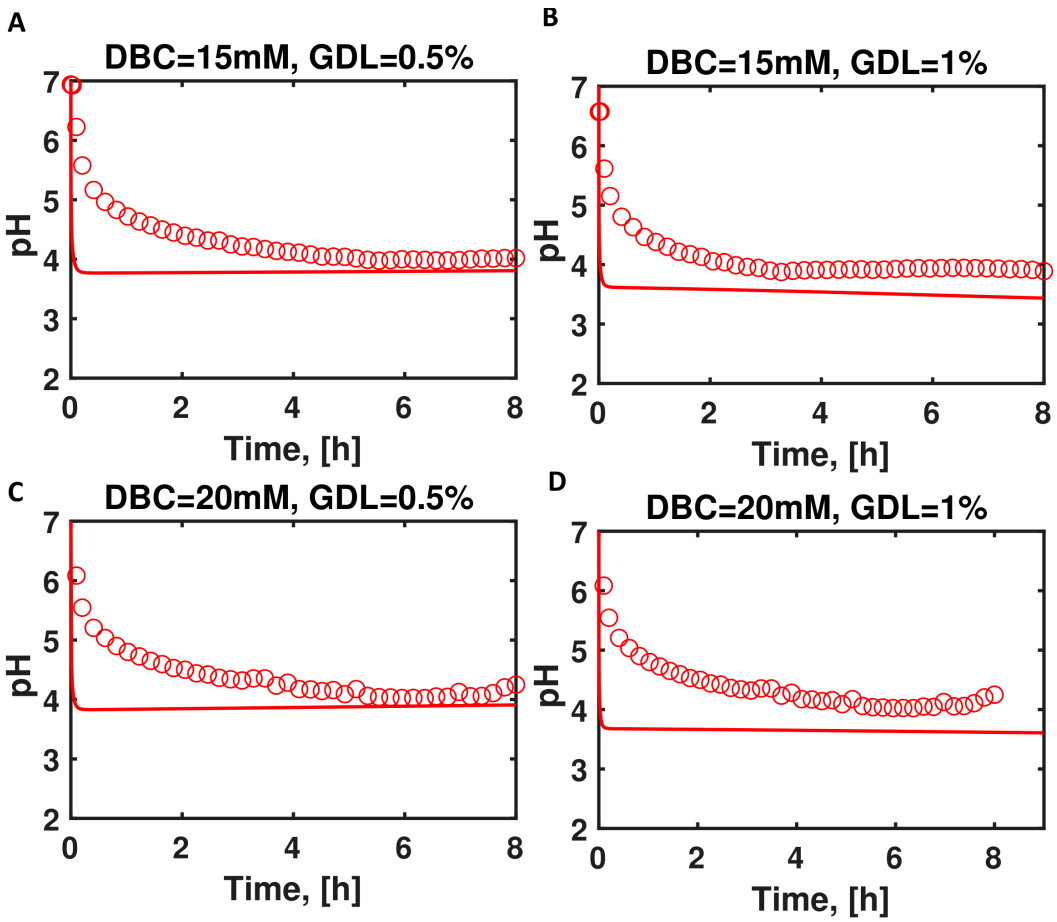

Figure S3. Experimental data (red open circles) and model (red solid lines) pH kinetics of the DBC – GDL system at different concentrations, A) [DBC] = 15mM, [GDL] = 0.5%; B) [DBC] = 15mM, [GDL] = 1%; C) [DBC] =20mM, [GDL] = 0.5%; D) [DBC] = 20mM, [GDL] = 1%. GDL % are wt.%.

Chapter 4

Electrochemically assisted hydrogel deposition, shaping and detachment

Abstract: *This work describes a facile approach allowing controlled deposition and controlled detachment of Dibenzoyl-L-Cystine (DBC) based hydrogel over a conducting support. The method itself is an electrochemically assisted approach, where the water oxidation at the electrode surface results in a local pH drop inducing DBC gelation and hydrogel formation. We have comprehensively described the possibility of the hydrogel shaping by alternating the anodic deposition potential, DBC concentration and finally the working electrode geometry. The latter includes macro-electrodes in a form of platinum discs having diameter equal to 200 and 500 µm; hexagonal arrays of circular platinum microelectrodes with a diameter of a single electrode equal to 5 or 10 µm and custom-made platinum microelectrodes, having the shape of circles, triangles and squares, that are used to shape the microgels. Over the course of our work, we were able to define the conditions to form a number of different hydrogel shapes such as: (i) flat and planar deposits; (ii) hemispherical deposits with an oxygen bubble pocket; (iii) spongy hydrogel structures or (iv) hemispherical micro-cups build from radially oriented DBC fibres directionally growing from the support. Furthermore, we were also able to remotely form and then detach the hydrogel deposit in the initial formulation solution using only an electrochemical trigger. Our work represents a solid proof of concept and opens a number of new avenues for the electrochemically assisted soft matter formulation down to micrometre scale.*

This chapter has been published as V. Lakshminarayanan, L. Poltorak, E. J. R. Sudhölter, E. Mendes, J. van Esch, *Electrochim. Acta* **2020**, *350*, DOI 10.1016/j.electacta.2020.136352.

4.1 Introduction

Supramolecular hydrogelators and their resulting hydrogels are being reported for a wide variety of applications including, but not limited to, cell culturing, tissue engineering, microfluidics, drug delivery, injectable therapeutics.[1] Structuring hydrogels is a necessity for the above-mentioned applications since when properly designed, these could encapsulate or interact with living matter or define the material properties.[2] A number of strategies to produce and structure supramolecular hydrogelators have been reported in the past two decades. These can be grouped based on the trigger used in the formation of the hydrogels, e.g. by heat,[3] light,[4] catalysis[5,6]] or pH gradients.[7,8] The local pH modulation can be triggered by means of hydrolysis[9,10] or electrochemically controlled redox reactions.[11–17] Among the acid triggers, glucono-δ-lactone (GDL) and acid hydrides have been used to control pH through hydrolysis. The resulting gradual change was used to control mechanical properties and gel homogeneity.[9,10,18]

Electrochemically triggered or assisted deposition of materials is a methodology where electrochemically formed species interact with a precursor present in the electrode vicinity with the ultimate goal to control the amount, shape, size, structure, topology or actuation of a modifier residing at the electrode surface. A whole range of different arrangements were employed over last years. (i) Electrochemically assisted deposition can be controlled with sacrificial metallic electrodes. Here, the anodic dissolution of the electrode allows for the formation of metal cations that are further employed in a deposition process. Formation of porous metal-organic frameworks[19,20] or surface modification using Cu^{+} catalysed azide-alkyl Huisgen cycloadditions (copper catalysed click chemistry reaction)[21] were accomplished within such a scenario. (ii) Another type of an assisted deposition involves the electrochemical conversion where produced species catalyse the deposit formation. The electrochemical reduction of Cu^{2+} to Cu^{+} or Fe^{3+} to Fe^{2+} was used to control click chemistry reactions with the goal to pattern surfaces with scanning electrochemical microscopy probes [21–23] Similar mechanisms were extensively studied and used in the electrochemical atom transfer radical polymerisation (eATRP) reactions where Cu^{2+} is reduced to Cu^{+} which further

catalyse polymer elongation[24–27]. (iii) Local change of the pH at the electrode surface is the following option giving possibility to control the surface decoration. Electrochemically controlled sol – gel process of silica, where both silane hydrolysis and the resulting silanol condensation are pH dependent reactions, is a very elegant example allowing for silica formation at the electrode surface. For instance, mesoporous silica films, with a high range symmetry of perpendicularly oriented silica pores were formed by simply reducing water (and NO_3^-) in the presence of cetyltrimethylammonium surfactant self-assembling at the electrode surface.[11,28–30]

Electrochemically assisted reactions can also be used to control hydrogel deposition. Up to now, only a few works related to the electro-addressing of acid triggered supramolecular hydrogelators proved the possibility to control formation, mechanical properties and composition (more than one gelator type present) of obtained hydrogels.[31,32] In the group of Payne, the simple two electrode configuration was used to deposit polysaccharide chitosan at the gold electrodes upon cathodic potential application.[33] This work was further extended to electrochemically controlled polysaccharide formation – disintegration using elongated Au electrodes.[31] Other work suggests the use of electro-addressing of low molecular weight gelators (LMWG) as a method to produce a temporary scaffold to template hydrogel formation based on temperature triggered biopolymer gelators.[12] Similarly, the carbazole-amino acid LMWG was first self-assembled at the electrode surface (pH drop induced by the oxidation of hydroquinone) followed by its polymerization.[34] In another example, the coumarin-dipeptide gel precursor was electrochemically deposited at the transparent electrode surface (again using electrochemical hydroquinone oxidation to yield protons) forming a gel that was further strengthen by photo-dimerization.[35] Palleau *et al*. showed that hydrogels in liaison with an electrochemical trigger can be used to induce soft material actuation,[36] while Kaniewska *et al*. combined QCM, voltammetry and impedimetric measurements to study a responsive hydrogel exposed to different pH and temperature values.[37] Some examples describe hydrogels used for electroanalysis, as for instance an iron based metal-organic gel used for thrombin detection,[38] polyvinyl

alcohol/polyacrylamide based hydrogels for urea sensing[39] or chitosan/gelatin modified scanning electrochemical microscopy probes for “in air” surface analysis.[40,41] It is however unclear how much one can control structure in electrochemically addressed self-assembling hydrogelating platforms. Also, it is unclear and unexplored what are the possible shapes and deposition limitations. Finally, the so far produced gels were crude and could not be detached electrochemically from the electrode without dissolving them.

Recently, we showed for the first time that pH gradients produced by electrochemical water splitting by Pt NP catalysts can be used to produce micro-shaped supramolecular hydrogels.[32] In this work we introduce a straightforward shaping methodology allowing the control of the topological properties of the electrochemically formed hydrogel deposits. Electrochemically Triggered Hydrogel Formation (ETHF) is based on electrochemically build pH gradients that trigger DBC gelation at the electrode surface. We found that the formation of unique and novel hydrogel topologies can be controlled with the help of (i) the shape and (ii) the size of the platinum electrodes. For the latter, downscaling the electroactive surface area to micrometre levels affected the geometry of the diffusion zones (transition from a linear to a hemispherical diffusion regime)[42,43] which could be visualized with resulting electrogenerated hydrogel hemispherical deposits. Interestingly, formation of oxygen bubbles during the electrochemical water splitting reaction also contributed to hydrogel engineering as pressurized pockets were entrapped within the hydrogel framework. Electrochemically formed hydrogel can retain the shape of the electroactive surface as shown with different shapes (circles, triangles and squares) produced via a photolithographic approach. Great potential and versatility of the method is proved as formed hydrogel deposits can be removed from the electrode surface (at optimized conditions), via controlled electrochemical means. To summarize, the novelty of our method originates from the diversity of unique shapes that could be created using electrochemically triggered pH gradients. Furthermore, the fact of remotely and electrochemically controlled hydrogel formation followed by detachment by simple switch between anodic and cathodic potential is unique.

We foresee that our method can be applied to a wide range of acid-triggered gelators, which together with further miniaturization, facile detachment of formed gel structures through electro-addressing and the possibility to vary the constitution of the gelating solution open a number of new applied avenues that we plan to pursue in the future.

4.2 Materials and Methods:

4.2.1 Materials

Gallium-Indium eutectic (Ga-In, >99%, Alfa Aesar), Sodium Nitrate ($NaNO_3$, 98.5%, Sigma Aldrich), Sodium Chloride (NaCl, 99%, Sigma Aldrich), Hydrochloric Acid (HCl, 1M, Sigma Aldrich), Sodium Hydroxide (NaOH, 1 M, Sigma Aldrich), Dibenzoyl-L-Cystine (DBC, 98%, Sigma Aldrich) were used as received. Sodium Salt of the gelator was prepared by titrating acidified gelator against 0.1 M NaOH (1:2 molar ratio). The solution containing neutralized and non-neutralized gelator was passed through an Acrodisc syringe filter (0.2 µm, PTFE membrane) to remove any possible impurities in a form of the non-neutralized gelator, which were present as white precipitate in the solution. The resulting clear solution was checked for turbidity and freeze dried under vacuum to yield a white flaky powder which was used for further experiments.

4.2.2 Electrodes preparation and electrochemical measurements

Pt electrodes with diameter equal to 200 µm and 500 µm were self-made. First, thick wall glass capillaries were closed on one end using a Bunsen burner and vacuum pump. Short pieces of Pt wire with corresponding diameter were then placed into the capillary. Heating the closed end of the capillary, with suction supplied from the open side, allowed the wire entrapment within the glass insulation. The excess of glass above the wire was removed. Next, the surface of the electrode was smoothened by fine polishing. The back contact was a tinned copper wire connected to the Pt with the help of Ga-In eutectic. To prevent liquid metal flowing out of the electrode, the open end of the glass tube was sealed with silicone acetate sealant. Unless otherwise stated, for all electrochemical experiments we used the

EmStat3+ Blue potentiostat from PalmSens working in a three-electrode configuration. The counter electrode was a platinum wire, whereas the Ag/AgCl was used as the reference electrode.

Microelectrodes in a form of thin film electrodes were ordered or custom made by Micrux. Electrodes with smallest dimensions had circular shape (with diameter of a single electrode equal to 5 µm or 10 µm) and were arranged in a hexagonal array. The pore centre–to –centre distance (spacing factor) was equal to 50 µm (for the array with a single electrode diameter equal to 5 µm) and 100 µm (for the array with a single electrode diameter equal to 10 µm) and was large enough to avoid overlap of hemispherical diffusion zones for experimental time scales. Some of the custom-made electrodes were given specific shape, these are triangles, squares and circles with the edge or diameter equal to 100 µm. Here the counter electrode and the reference electrode were made out of Pt.

4.2.3 Optical and Polarization Microscopy

The goal of the polarization microscopy measurements was to confirm the presence of DBC gel fibres and to corroborate obtained data with the optical microscopy measurements. We constructed a special cell to be able to carry out optical and polarization microscopy measurements at one go. During and after every electrochemical deposition experiment, as observed using episcopic illumination (reflected light as opposed to transmitted light), the polarizer and analyser were crossed (90°). This setting allowed the observation of the DBC gel fibres since these form crystalline fibrous gel networks in the form of spherulites. Under cross-polarization conditions, spherulitic networks are expected to show a Maltese-cross hair pattern indicating the presence of oriented crystalline fibre domains.

ETHF was followed using sub-macro sized Pt electrodes and optical microscope. The experimental setup (see Figure S1) was mounted to the microscope stage where it was fastened by means of Scotch tape. Images and videos were recorded at magnifications between 5X and 20X. To investigate ETHF at the microfabricated Pt electrodes, Nikon Eclipse

E600 POL microscope was used in Diascopic mode. The experimental setup consisting of the electrode arrays, electrolyte solution was securely fastened on the microscope stage by means of Scotch tape. Images and videos were acquired under normal and cross-polarization (polarizer and analyser at 90° to each other) conditions at objective magnifications ranging from 5X-20X.

4.2.4 Scope of the method

Electrochemically modulated pH allows for the facile hydrogel deposition whereas the size and the shape of the electrode can be used to control the hydrogel dimensions and its final form as shown here and in few other works published over last few years.[31,32,34,35] In all electrode configurations used in this work, the hydrogel deposition was triggered by anodic water oxidation that yielded the desired pH drop. In this work a few different geometrical approaches were pursued and are summarized in Figure 1. In Figure 1A the drawing of a macroscopic layout of the electrode (diameter (DIA) ≥ 200 µm) is shown. As described in the results and discussion section, this configuration yielded two types of hydrogel deposits: (i) a flat – "pancake" like, thin hydrogel films found for lower applied water oxidation potential and a short deposition time, and (ii) oxygen bubble templated, rounded cups formed at higher applied anodic potentials. The electrochemical formation of rounded macroscopic hydrogel (with carbazole-aniline used as LMWG) deposit was also created by Kubiak *et al.* at the Au electrode with DIA = 1.6 mm.[31] In the respective work the hydroquinone oxidation was used, and hence, no gas was formed as in the case of electrochemical water oxidation.

Figure 1B depicts the drawing of a miniaturized system which is represented by a hexagonal array of electrodes with micrometre dimension (DIA = 5 – array 01 or 10 µm – array 02) and a spacing factor (S = 50 or 100 µm for array 01 and 02 respectively) assuring individual behaviour of each electrode within the array. In other words, for the applied experimental time scales, each electrode holds individual hemispherical diffusion zone formed by H^+ heading towards the bulk of the solution. The micro-hemispherical hydrogel deposits can be formed within this configuration and these are simple out-prints of hemispherical diffusion

zones of H^+ transferring towards the bulk of the solution. As shown in Figure 1C, also the shape of the electrode can be used to control the final form of the hydrogel deposit. Examples chosen in this work cover squares, circles and triangles. The methodology is covered and described in following sections.

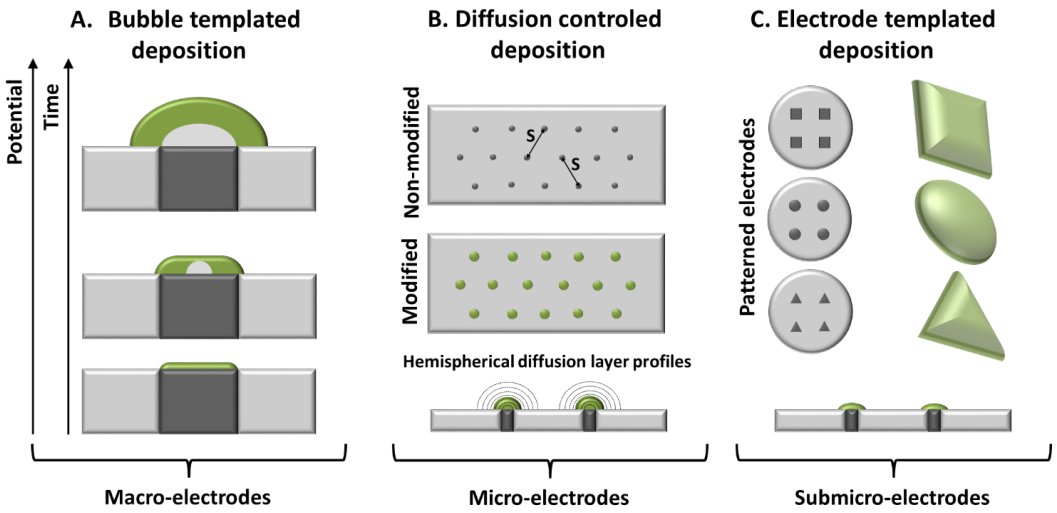

Figure 1. The overview of the ETHF performed at different length scales. A – Macro-electrodes with dimensionality ≥ 200 µm allowing for the flat and oxygen bubble templated hemispherical hydrogel deposits formation. B – Array of microelectrodes with the dimensionality ≤ 50 µm for hemispherical hydrogel microstructures deposition C – Predefined electrode shapes preserved by hydrogel during ETHF process.

4.3 Results & Discussion

4.3.1 Hydrogel formation at macro-electrodes

First, we investigated the effect of different experimental variables (applied potential, time and Na_2DBC concentration) on ETHF at macro Pt electrodes – with DIA equal to 200 µm and 500 µm. Figure 2A shows the height of the hydrogel deposit measured over 300 s for different constant potential values applied to the working electrode (*vs* Ag/AgCl reference electrode) during chronoamperometric measurements. Obtained results are in line with what was reported earlier by others. [13,15] We did not observe any hydrogel formation at

potentials equal up to 1.3 V, and as found from voltammetric measurements (data not shown) substantial currents originating from water oxidation (eq. 1) started rising at potentials higher than 1.4 V.

$$2H_2O - 4e^- \rightarrow 4H^+ + O_2 \qquad \text{(eq. 1)}$$

For all applied potential values, the hydrogels deposits grow in the first few seconds (7 – 15 second depending on the potential applied, see Figure 2A and movie MS1 available as supporting information) after which the deposit height has reached a plateau. This is due to two effects. (i) For low potential values (see image in Figure 2C for 1.5 V) the oxygen evolution is still discrete (formed oxygen dissolves in the adjacent aqueous phase or forms bubbles that cannot be visualized with the employed microscope) and formed hydrogel entirely covers the electroactive surface area of the Pt electrode. A compact layer of a hydrogel at the electrode surface most probably hinders the diffusion of water molecules, and subsequently the formed protons (the diffusion coefficient value for protons in the hydrogel[44] is slightly lower than that recorded in water[45]) and transferring from the bulk DBC molecules, to and from the electrode surface due to an increased local viscosity and crowding effect. (ii) Starting from around 1.8 V water oxidation leads to oxygen bubble formation, entirely covering the electrode surface. This limits the electroactive surface to a multiphase junction located between glass insulation, Pt electrode, gas bubble and formed hydrogel. As a result, these are only the first few seconds (up to 15s – see Fig. 2A) that allows the sufficient number of protons to be formed, which are pushed away (together with the solution containing DBC molecules) from the electrode surface by growing oxygen bubble. Simultaneously the gelation entraps the bubble and forms a very unique shape of a hydrogel hemispherical dome with spherical, bubble templated pocket in its interior. Figure 2B shows the height (averaged over last 150 s of chronoamperometric experiment) of the hydrogel deposit formed at the electrode with the DIA equal to 500 µm as a function of the applied potential from 1.3 V up to 2.5 V. When the electrode with DIA equal to 200 µm was used, a linear growth of a hydrogel was achieved only up to 2.2V (see Figure S2). For higher potential

values the strength of the formed hydrogel did not resist the pressure of the evolving bubble, leading to continues water oxidation and hydrogel growth (see Figure S3) or partial detachment of the hydrogel deposit from the electrode surface. From linear fitting of the hydrogel height growth as a function of the applied potential we can deduce that the growth factor is around 637 µm and 370 µm (in height) per Volt for the electrodes having diameter equal to 500 µm and 200 µm, respectively.

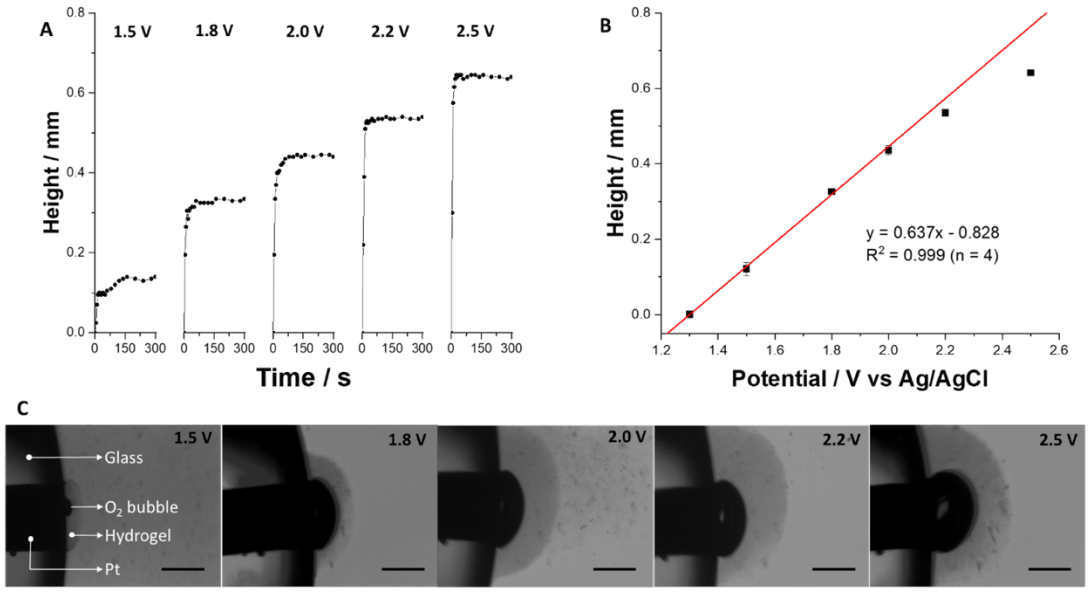

Figure 2. A – Height of a hydrogel deposit for different applied anodic potential values measured for 300 seconds; B – height of the hydrogel deposit in function of the applied potential averaged for last 150 second of deposition time; C – optical microscope images recorded at deposition time t = 300 seconds at different applied potential values (scale bars correspond to 250 µm, DIA of the electrode is 500 µm). The concentrations of all reagents used during the measurements were as follow: [Na_2DBC] = 10 mM; [$NaNO_3$] = 500 mM. Description of the images content is given in the left image of the panel C.

By using simple scrutiny and a few simplifications (negligible dissolution of formed oxygen in the adjacent solution, lack of oxygen diffusion through the hydrogel layer and ideal dimensionality of the formed bubble) we estimated the order of the oxygen pressure inside

the hydrogel deposits. Integration of chronoamperometric transients recorded at different deposition potential values allowed a charge estimation used for water oxidation. From Faraday's law of electrolysis, we then calculated the number of moles of formed oxygen gas. Assuming ideal gas behaviour

$$pV = nRT \qquad \text{(eq. 2)}$$

and spherical dome dimensions of gas bubbles entrapped within hydrogel framework

$$V = \frac{1}{6}\pi h(3r^2 + h^2) \qquad \text{(eq. 3)}$$

where p is the pressure, V is the volume, n is the number of moles, R is the gas constant, T is the temperature, h is the height of a spherical oxygen bubble and r is the radius of the oxygen bubble base, we estimated a pressure of a gas inside the hydrogel cup equal to few bars (3.5 – 5.5 bar) depending on the potential applied. Although these values are probably inflated due to assumption taken, we concluded that the oxygen bubble in the hydrogel pocket is pressurized. This example provides a possible approach towards storage of gases (O_2 and H_2 in the case of H^+ and OH^- triggered gelation respectively) through hydrogel-based encapsulation. The further exploration of this topic was beyond the scope of this work.

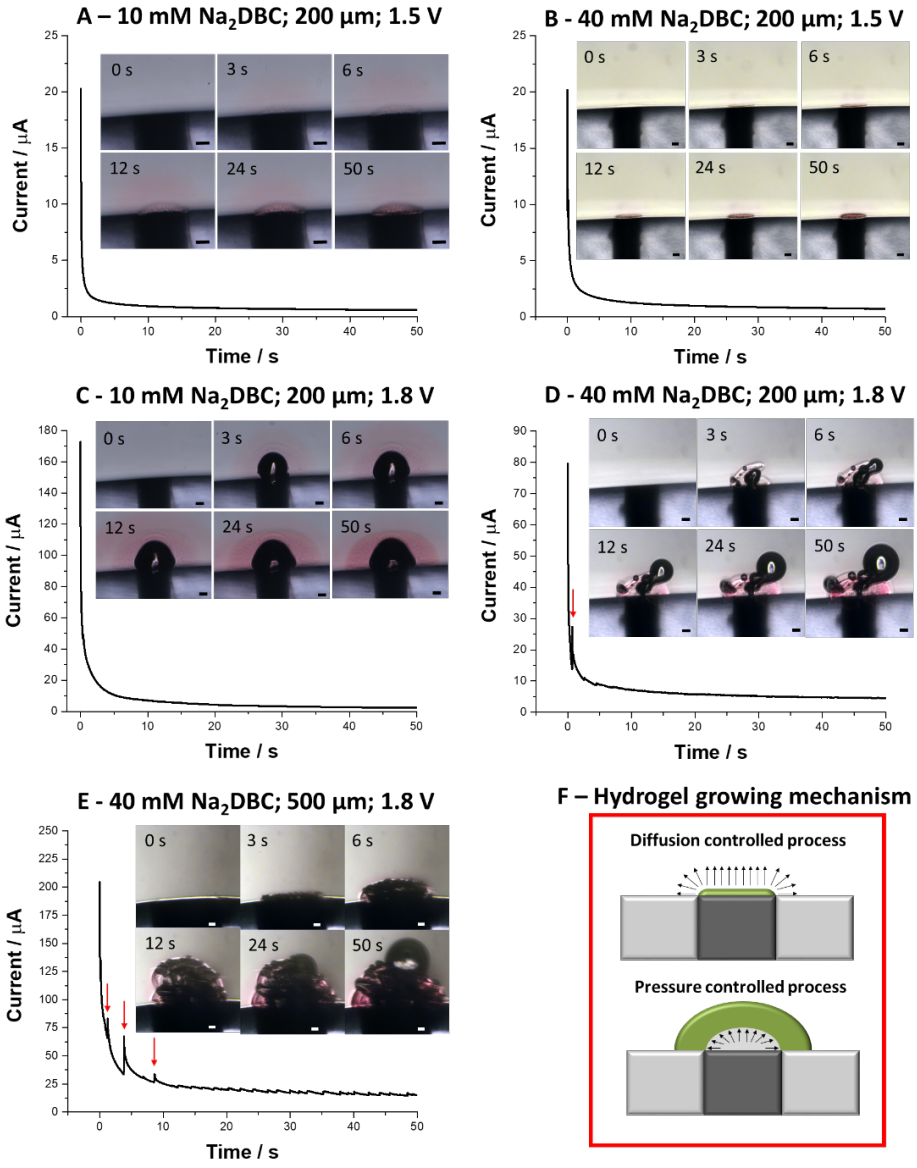

Figure 3. A - E – Chronoamperograms recorded at Pt electrodes having diameter equal to 200 µm and 500 µm at 1.5V and 1.8V (experimental conditions are indicated on the left from each graph). Inserts of each chronoamperogram represents set of images with corresponding time recorded during electrochemical hydrogel formation. Experimental conditions are given next to figure numbering. In all cases [$NaNO_3$] = 500 mM and [Nile Red] =50 µM. All scale bars are equal to 50 µm. F – shows the schematic of two possible hydrogel growth mechanisms.

The effect of [Na_2DBC] on the hydrogel formation at macro electrodes was also investigated. In Figure 3 the chronoamperograms with the images of the hydrogel formed at different experimental conditions are shown. As already indicated before, in most cases, the overall process occurs within first few seconds. For the lower [Na_2DBC] = 10 mM two characteristic shapes of a hydrogel deposits can be distinguished (Figure 3A and 3C). When E = 1.5 V was applied, slightly rounded on the edges but still flat in the middle (for the electrode with DIA = 500 µm flat in the middle and rounded on the edges – Figure 2C) deposit was formed which correspond to the out-print of the diffusion zone governed by proton flux heading from the electrode surface to the bulk of solution formed during water oxidation – see Figure 3A. For higher E = 1.8 V the shaping process was governed by synergistic effect of protons diffusion and convection with the latter caused by the evolution of oxygen bubble further encapsulated in the hydrogel framework – see Figure 3C. Increasing the concentration of Na_2DBC to 40 mM has led to interesting observations. As shown in Figure 3B, for E = 1.5 V, much flatter but still rounded on the edges, deposits were formed. When E = 1.8 V was applied (Figure 3D for the electrode with DIA = 200 µm and Figure 3E for the electrode with DIA = 500 µm) the flat deposit formed within the first three seconds, after which it started to detach due to growing oxygen bubbles. Each delamination step is accompanied by characteristic current spikes (marked with red arrows on Figure 3D and Figure 3E) observed in the chronoamperograms. As the cup detaches, the availability of the platinum surface to the water oxidation results in a fresh proton wave subsequently triggering gelation. The defects in such detaching hydrogel deposits were replenished with bubbles giving the hydrogels a sponge-like microstructure. The oxygen bubbles stay entrapped in the hydrogel network further confirming its potential for gas storing applications.

4.3.2 Hydrogel formation at an array of microelectrodes

Following the success of hydrogel formation on macroscopic Pt electrodes, we explored the possibility of miniaturizing this technique. Current applications of miniaturized electrodes in liaison with hydrogels are mainly focused on sensing.[46–49] In these works, the hydrogel layer is usually prepared using chemical,[47] photochemical or electropolymerization reactions.

Electrochemically triggered deposition is, to the best of our knowledge, is limited only to a few works. These cover the micro-gel electro-addressing on a gold microelectrode in a form of elongated stripes[13] or the squared nano-band electrodes[50] contacted to a solution containing a redox active pH trigger. For our approach we used a commercially available array of circular and planar micro-electrodes that were produced using photolithography. The microscopy images of arrays can be found in the supplementary information (see Figure S4). We investigated the formation of hydrogels using linear sweep voltammetry under optical and polarization microscopy (see Figure 4, S7 and S8) for various concentrations of the gelator (Na_2DBC). Figure 4A shows the time evolution of the growing hydrogel caps formed in a 10 mM Na_2DBC from the micro electrode array (chosen hexagon is one among many) with a single electrode DIA equal to 10 µm. The hydrogel started growing at the E equal to around 1.7 V (potential measured versus pseudo-reference Pt electrode) when the current reached around 1 µA. In contrary to macroscopic electrodes, the hydrogel grows continuously as the potential is swept towards anodic directions (see Figure S5 in supplementary information). This is understandable since, the concentration of H^+ increases at the electrode-solution interface and diffuse towards the bulk of the solution. Moreover, we can speculate that the formed oxygen is pressurised within the hydrogel framework and forms (if any) nano-bubbles which are not blocking the electroactive surface of the electrodes within the array. Occasionally, for higher anodic potential values, individual hydrogel cups were breaking and the released oxygen bubble was covering most or even whole array (see Figure S6 in supplementary information). Under cross-polarization (see Figure 4-B for the array and 4-E for the single hydrogel cup, Figure S7 gives similar observation for different concentrations) we observed that the formed hydrogels displayed cross-hair patterns reminiscent of spherulites (spherical semi-crystalline regions). This assumes that the formed shapes are full hemi-spheres. Efforts to obtain the experimental proof for the exact shape of the hydrogel caps were undertaken but with limited results. We found that the topological analysis of soft matter at the microscopic level is very challenging. Attempts to analyse the hydrogel cups shape using confocal fluorescent microscopy or atomic force microscopy were fruitless. We made Z-stack images (using optical microscopy),

which were not of sufficient resolution quality to yield concrete results. However, work dealing with the electrochemical modification of nano- or micro-electrodes does exist. It was found that the metals electrodeposited over the microelectrodes do take the hemispherical shape of a diffusion layer profile established above such an electrode.[51] Similar observations were made for the electrochemically assisted silica deposition, derived from the sol-gel processing, over array of micropores.[52–55] On top of that, it has been shown that DBC fibres orient themselves along the direction of the H^+ gradient.[8] For all taken together, with high dose of confidence, we concluded that the formed hydrogel fibres have a hemi-spherulitic structure which probably have a radially outward fibre-orientation (see Figure 4-C for visualisation). Upon increasing the Na_2DBC concentration, we observed the changes in the fibres packing density. This can be seen in Figure S7 available in the supplementary information. No hydrogel deposit was found when the Na_2DBC < 2.5 mM. The critical gelator concentration (minimum concentration for the formation of a gel) for DBC is known to be around 2.2 mM.[3] When 5 mM Na_2DBC was applied we noticed (qualitative observation) that the fibres within the formed hydrogel cups appeared to be loosely packed (Figure S7 – 1B and 1C) – open structures with bunches of individual fibres. The electrochemically assisted formation of the silica at the ultramicroelectrodes revealed similar findings and suggest that the reagents generated in a faster way at the microscale affects the morphology of the electrochemically generated deposits.[56] Further increase in concentration from 10 mM up to 40 mM yielded no other visual changes in the hydrogel appearance apart from earlier mentioned changes with regard to packing density. In this concentration range, the DIA of the hydrogel cups stayed roughly the same with only the time having an impact on the them (diffusion of protons). Similar observations were made for the array with the single electrode DIA equal to 5 µm (see Figure S8). The only difference was the smaller dimensionality of the obtained hydrogel cups and higher packing of the deposits given by the number of electrodes within the array. On the whole, we achieved the formation of hydrogels on microelectrode arrays with the ability to exert control over microstructure and morphology by varying the gelator concentration (open vs. closed compact). The SEM characterization of obtained hydrogel morphologies was not possible since upon application

of vacuum (or even exposure to air for longer time) structure disruptive crystallization (of both, the DBC and background electrolyte solution) occurred. In our previous work, we were electrochemically generating DBC fibres at the electrochemically deposited Pt NPs at the copper mesh supports. These were then analysed using cryogenic transmission electron microscopy yielding the fibrous structure of the obtained hydrogels.[32]

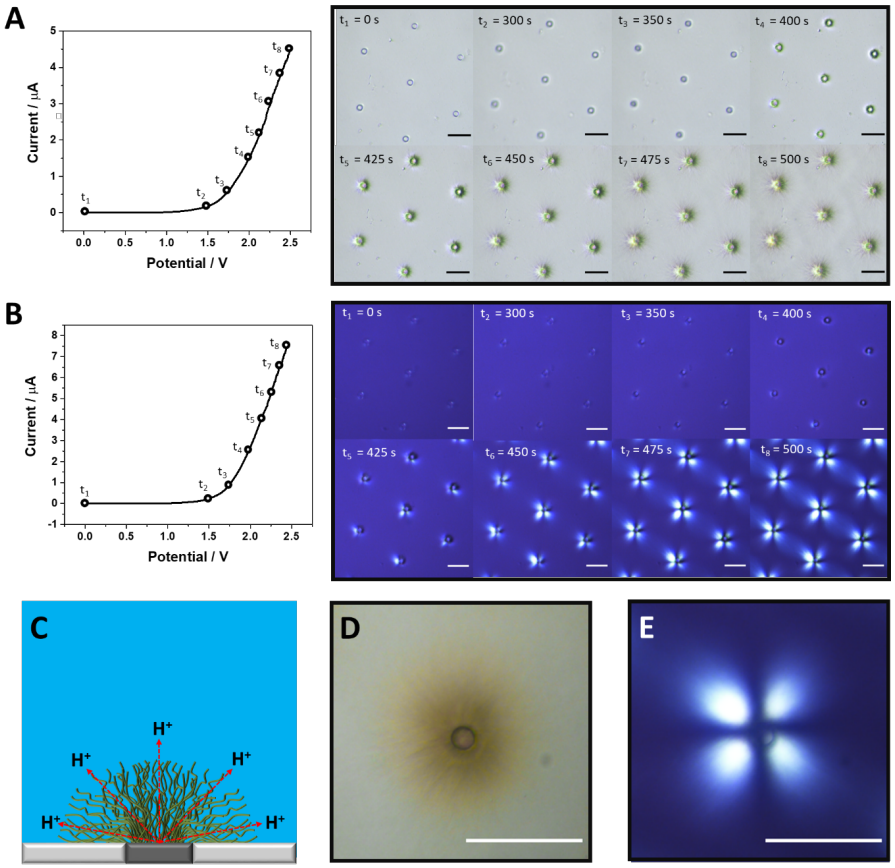

Figure 4. A and B represent linear sweep voltammograms recorded in 10 mM Na_2DBC and 500 mM $NaNO_3$ solution at 5 $mV \cdot s^{-1}$ with corresponding sequence of optical microscope images (on the right from voltammograms) recorded during voltametric hydrogel deposition (A – normal microscopy; B – polarization microscopy)). C is the schematic representation (to the best of our understanding) of the hydrogel deposit grown over platinum microelectrode. D and E are the images taken at higher magnification under optical and polarization microscopy respectively after deposition process. The single electrode DIA = 10 µm; S (pore centre to centre distance) = 100 µm. The scale bars are equal to A and B – 100 µm and D and E – 50 µm.

4.3.3 Hydrogel shaping with different electrode shapes

Having explored the possibility of controlling dimensions and network morphology, we next investigated the ability to shape hydrogels through our technique. The rationale was that the shape of the electrode would influence the final shape of the produced hydrogel. To this end, we designed different Pt electrode arrays (100 µm in size) of three different shapes namely circles, squares and triangles (see Figure 5) respectively. The arrays were setup and connected for optical and polarization microscopy experiments as shown in Figure S1-B. Linear sweep voltammetry from 0 to 2.5 V at a scan rate of $5mVs^{-1}$ was used and images were recorded. Movies MS2 and MS3 (available in supplementary information) show the formation of hydrogels recorded at the electrode array with the single electrode having the shape of square or triangle respectively. For both cases the concentration of Na_2DBC equal to 25 mM. Hydrogels formed at lower concentrations exhibited more loose networks as compared to more compact structures at higher concentration of the gelator. This observation was similar to what was previously observed for micro-electrode arrays. Figure 5 shows the formed hydrogels under normal and cross-polarized conditions recorded after deposition process. The formed hydrogels (Panels D – F) retain the shapes of the underlying electrode with dimensions in the order of a few hundred micrometres. Under cross-polarization (Panels G – I) the hydrogels show birefringent domains unlike the clear Maltese cross pattern observed for smaller micro-electrode arrays. Maltese crosses suggest that gel fibrils are pointing outwards from the electrode centre in analogy to nematic phases trapped in droplets. In the present case, its absence is probably due to complex diffusion layer profiles established over rather non-conventional electrode shapes as well as the presence of many sites of gel nucleation caused by impurities/edge effects etc. Interestingly, we observed that at the initial stages of the deposition process the hydrogel formation begins at the edges and proceeds inwards. Similar observations were reported by Piper *et al* who employed the square band like microelectrodes array for electrochemically assisted carbazole-alanine LMWG deposition.[50] By stopping the electro-catalytic process during this stage, it might be possible to obtain hollow circles, squares and triangles (see Figure S8

in supporting information). On the whole, it is possible to shape hydrogels by careful design of Pt electrode substrates.

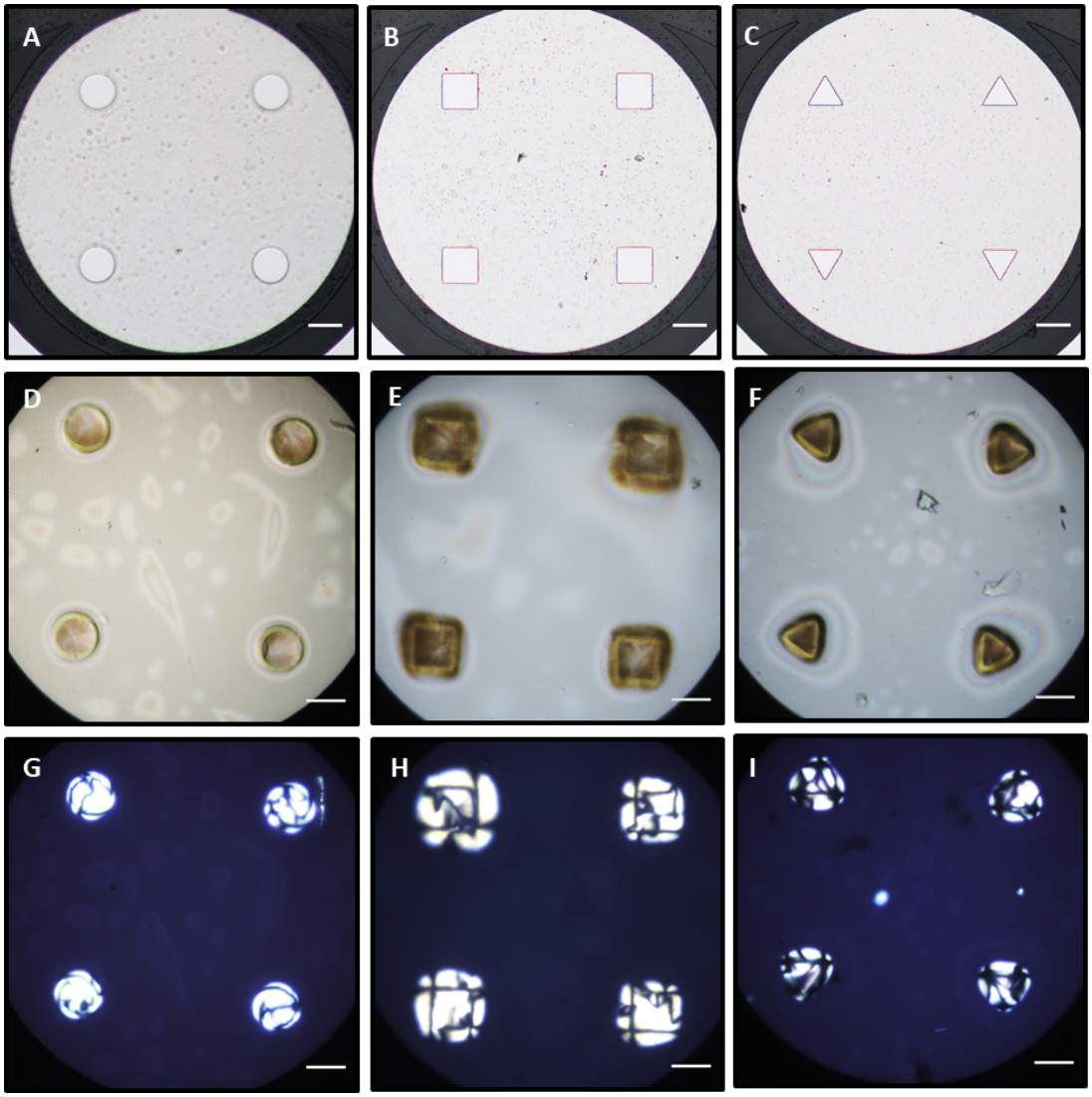

Figure 5. Shaping of hydrogels using array of Pt electrodes with a shape of a circle, square and triangle. A, B and C are the optical microscopy images of an unmodified array. D, E and F are the optical microscopy images recorded after a voltammetric sweep from 0 to 2.5 V at 5 $mV \cdot s^{-1}$ (25 mM Na_2DBC in 0.5 M $NaNO_3$). G, H and I are the image taken with polarization microscopy (conditions are the same as for D, E and F). All scale bars are 100 µm.

4.3.4 Detachment

In order to be able to utilize the produced hydrogels for biomedical applications, it is necessary to be able to detach them after formation. Consequently, we have explored the possibility to detach these hydrogels in a fully controlled manner, again using only an electrochemical trigger. In previous works, the formation and disappearance were well controlled but detachment of the produced hydrogels was not shown. Consequently, in addition to hydrogel shaping, we have given significant attention to controlled and effort-free hydrogel detachment from the electrode surface. Figure 6 image 1 shows the "pancake-like" hydrogel deposit formed at 1.5 V (*vs* Ag/AgCl) in 40 mM Na_2DBC solution at the electrode with diameter equal to 500 µm. The key to detach the hydrogel was to apply a negative potential allowing for the water and/or protons and/or nitrate reduction.

$$H_2O + 2e^- \rightarrow 2OH^- + H_2 \quad \text{(eq. 4)}$$

$$2H^+ + 2e^- \rightarrow H_2 \quad \text{(eq. 5)}$$

$$NO_3^- + H^+ + e^- \rightarrow NO_2 + H_2O \quad \text{(eq. 6)}$$

As shown in Figure 6 image 9, the application of a potential equal to -1.4V resulted in the "pancake-like" hydrogel detachment already after 4 seconds (the detachment can be additionally visualized in movie MS4 available as supporting information). We belief that detachment is due to two synergistic effects: (i) formed hydrogen (and probably small amounts of nitrogen dioxide) bubbles simply pushes away the rigid hydrogel framework from the electrode surface (see Figure 6 images from 3 to 9) whereas (ii) local increase in the pH results in a dissolution of the skin layer of a hydrogel (originating from the dissociation of the carboxylic functions within DBC gelator). Since formed hydrogen bubbles adhere to the hydrogel deposit, after detachment, it flows towards and then remains at the surface of Na_2DBC solution. Similarly, we could detach slightly rounded and still flat deposits formed at the electrode with a diameter equal to 200 µm. This detachment method has some limitations. First of all, the application of a cathodic potential < – 1.5V is not advisable,

as it leads to substantial bubble formation and a rapid hydrogel dissolution (data not shown). The detachment method also fails when it comes to the detachment of the oxygen bubble templated hydrogel deposits obtained at $E_{depostion}$ > 1.6V, most likely because the oxygen bubble (covering the Pt electrode surface) insulating properties inhibit the water and proton reduction reactions. It should be noted that in the case of micro-electrode arrays the inhibiting effect of the oxygen bubble is not as pronounced, but here dissolution of the deposit rather than detachment is playing a major role while the cathodic potential is applied (see Figure S12). As one of the future directions we aim at optimizing the surface adhesion properties to achieve electrochemically controlled hydrogel micro-deposits detachment.

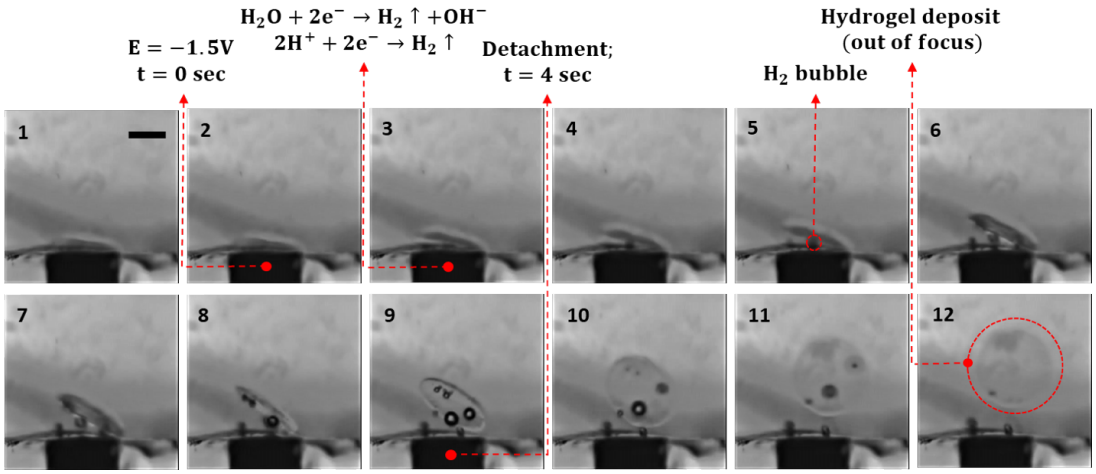

Figure 6. Images from 1 to 12 are the frames taken from the movie recorded during electrochemically controlled detachment of a hydrogel deposits formed at E = 1.5 V in 40 mM Na_2DBC in 500 mM $NaNO_3$ for 150 seconds (see image 1 for the corresponding deposit). The images are saturated with grey colour in order to increase the contrast. Scale bar – 100 µm.

4.4 Conclusions

In this work, we have shown that electrochemical water-splitting reaction catalysed by Pt can be used to trigger the formation of supramolecular hydrogels *via* the acid-induced directed self-assembly of LMWG. Upon application of an anodic potential, a proton gradient is produced at the electrode surface that results in the formation of oriented hydrogel fibres,

as controlled by the direction of the proton diffusion. Using different designs of Pt electrodes, we could establish control over size (macro, sub-macro and micro scales) and shape (circles, squares, triangles) of the produced hydrogels. The formed hydrogels can also be detached using an electrochemical trigger, this is the application of the cathodic potential. To the best of our knowledge this is the first example of a detachable supramolecular hydrogel network without the use of a secondary network.

References

[1] V. Le Sage, V. Lakshminarayanan, E. Mendes, R. Eelkema, J. Van Esch, Dynamic supramolecular hydrogelators: A biomedical perspective, Chim. Oggi. 32 (2014) 62–66.

[2] Q. Liu, M. Zhao, S. Mytnyk, B. Klemm, K. Zhang, Y. Wang, D. Yan, E. Mendes, J.H. van Esch, Self-Orienting Hydrogel Micro-Buckets as Novel Cell Carriers, Angew. Chemie - Int. Ed. 58 (2019) 547–551. https://doi.org/10.1002/anie.201811374.

[3] A. Friggeri, B.L. Feringa, J. van Esch, Entrapment and release of quinoline derivatives using a hydrogel of a low molecular weight gelator., J. Control. Release. 97 (2004) 241–248. https://doi.org/10.1016/j.jconrel.2004.03.012.

[4] C. Maity, W.E. Hendriksen, J.H. van Esch, R. Eelkema, Spatial Structuring of a Supramolecular Hydrogel by using a Visible-Light Triggered Catalyst, Angew. Chemie. 127 (2015) 1012–1015. https://doi.org/10.1002/ange.201409198.

[5] Y. Wang, F. Versluis, S. Oldenhof, V. Lakshminarayanan, K. Zhang, Y. Wang, J. Wang, R. Eelkema, X. Guo, J.H. van Esch, Directed Nanoscale Self-Assembly of Low Molecular Weight Hydrogelators Using Catalytic Nanoparticles, Adv. Mater. 30 (2018) 1–7. https://doi.org/10.1002/adma.201707408.

[6] J. Boekhoven, J.M. Poolman, C. Maity, F. Li, L. van der Mee, C.B. Minkenberg, E. Mendes, J.H. van Esch, R. Eelkema, Catalytic control over supramolecular gel formation., Nat. Chem. 5 (2013) 433–437. https://doi.org/10.1038/nchem.1617.

[7] A.G.L. Olive, N.H. Abdullah, I. Ziemecka, E. Mendes, R. Eelkema, J.H. van Esch, Spatial and Directional Control over Self-Assembly Using Catalytic Micropatterned Surfaces, Angew. Chemie Int. Ed. 53 (2014) 4132–4136. https://doi.org/10.1002/anie.201310776.

[8] I. Ziemecka, G.J.M. Koper, A.G.L. Olive, J.H. van Esch, Chemical-gradient directed self-assembly of hydrogel fibers, Soft Matter. 9 (2013) 1556–1561. https://doi.org/10.1039/c2sm27095a.

[9] D.J. Adams, M.F. Butler, W.J. Frith, M. Kirkland, L. Mullen, P. Sanderson, A new method for maintaining homogeneity during liquid–hydrogel transitions using low molecular weight hydrogelators, Soft Matter. 5 (2009) 1856–1862. https://doi.org/10.1039/b901556f.

[10] E.R. Draper, L.L.E. Mears, A.M. Castilla, S.M. King, T.O. McDonald, R. Akhtar, D.J. Adams, Using the hydrolysis of anhydrides to control gel properties and homogeneity in pH-triggered gelation, RSC Adv. 5 (2015) 95369–95378. https://doi.org/10.1039/C5RA22253B.

[11] Y. Guillemin, J. Ghanbaja, E. Aubert, M. Etienne, A. Walcarius, Electro-Assisted Self-Assembly of Cetyltrimethylammonium- Templated Silica Films in Aqueous Media : Critical Effect of Counteranions on the Morphology and Mesostructure Type, Chem. Mater. 26 (2014) 1848–1858.

[12] X.-W. Shi, C.-Y. Tsao, X. Yang, Y. Liu, P. Dykstra, G.W. Rubloff, R. Ghodssi, W.E. Bentley, G.F. Payne, Electroaddressing of Cell Populations by Co-Deposition with Calcium Alginate Hydrogels, Adv. Funct. Mater. 19 (2009) 2074–2080. https://doi.org/10.1002/adfm.200900026.

[13] Y. Liu, E. Kim, R. V. Ulijn, W.E. Bentley, G.F. Payne, Reversible Electroaddressing of Self-assembling Amino-Acid Conjugates, Adv. Funct. Mater. 21 (2011) 1575–1580. https://doi.org/10.1002/adfm.201002020.

[14] E.R. Draper, K.L. Morris, M.A. Little, J. Raeburn, C. Colquhoun, E.R. Cross, T.O. McDonald, L.C. Serpell, D.J. Adams, Hydrogels formed from Fmoc amino acids, CrystEngComm. 17 (2015) 8047–8057. https://doi.org/10.1039/C5CE00801H.

[15] J. Raeburn, B. Alston, J. Kroeger, T.O. McDonald, J.R. Howse, P.J. Cameron, D.J. Adams, Electrochemically-triggered spatially and temporally resolved multi-component gels, Mater. Horizons. 1 (2014) 241–246. https://doi.org/10.1039/c3mh00150d.

[16] E.K. Johnson, D.J. Adams, P.J. Cameron, Directed Self-Assembly of Dipeptides to Form Ultrathin Hydrogel Membranes, J. Am. Chem. Soc. 132 (2010) 5130–5136. https://doi.org/10.1021/ja909579p.

[17] Y. Liu, Y. Cheng, H.-C. Wu, E. Kim, R. V. Ulijn, G.W. Rubloff, W.E. Bentley, G.F. Payne, Electroaddressing Agarose Using Fmoc-Phenylalanine as a Temporary Scaffold, Langmuir. 27 (2011) 7380–7384. https://doi.org/10.1021/la201541c.

[18] A.Z. Cardoso, A.E. Alvarez Alvarez, B.N. Cattoz, P.C. Griffiths, S.M. King, W.J. Frith, D.J. Adams, The influence of the kinetics of self-assembly on the properties of dipeptide hydrogels, Faraday Discuss. 166 (2013) 101–116. https://doi.org/10.1039/c3fd00104k.

[19] R. Ameloot, L. Stappers, J. Fransaer, L. Alaerts, B.F. Sels, D.E. De Vos, Patterned growth of metal-organic framework coatings by electrochemical synthesis, Chem. Mater. 21 (2009) 2580–2582. https://doi.org/10.1021/cm900069f.

[20] S. Sachdeva, M.R. Venkatesh, B. El Mansouri, J. Wei, A. Bossche, F. Kapteijn, G.Q. Zhang, J. Gascon, L.C.P.M. de Smet, E.J.R. Sudhölter, Sensitive and Reversible Detection of Methanol and Water Vapor by In Situ Electrochemically Grown CuBTC MOFs on Interdigitated Electrodes, Small. 13 (2017) 1–6. https://doi.org/10.1002/smll.201604150.

[21] V. Badets, D. Duclos, D. Quinton, O. Fontaine, D. Zigah, Original Dual Microelectrode : Writing and Reading a local click reaction with Scanning Electrochemical Microscopy, Electrochim. Acta. 201 (2016) 274–278. https://doi.org/10.1016/j.electacta.2015.10.066.

[22] D. Quinton, A. Maringa, S. Griveau, T. Nyokong, F. Bedioui, Surface patterning using scanning electrochemical microscopy to locally trigger a “click” chemistry reaction, Electrochem. Commun. 31 (2013) 112–115. https://doi.org/10.1016/j.elecom.2013.03.021.

[23] S.-Y. Ku, K.-T. Wong, A.J. Bard, Surface patterning with fluorescent molecules using click chemistry directed by scanning electrochemical microscopy., J. Am. Chem. Soc. 130 (2008) 2392–2393. https://doi.org/10.1021/ja078183d.

[24] A. Furst, S. Landefeld, M.G. Hill, J.K. Barton, Electrochemical patterning and detection of DNA arrays on a two-electrode platform, J. Am. Chem. Soc. 135 (2013) 19099–19102. https://doi.org/10.1021/ja410902j.

[25] N. Shida, Y. Koizumi, H. Nishiyama, I. Tomita, S. Inagi, Electrochemically mediated atom transfer radical polymerization from a substrate surface manipulated by bipolar electrolysis: Fabrication of gradient and patterned polymer brushes, Angew. Chemie - Int. Ed. 54 (2015) 3922–3926. https://doi.org/10.1002/anie.201412391.

[26] B. Li, B. Yu, W.T.S. Huck, W. Liu, F. Zhou, Electrochemically mediated atom transfer radical polymerization on nonconducting substrates: Controlled brush growth through catalyst diffusion, J. Am. Chem. Soc. 135 (2013) 1708–1710. https://doi.org/10.1021/ja3116197.

[27] S. Park, P. Chmielarz, A. Gennaro, K. Matyjaszewski, Simplified electrochemically mediated atom transfer radical polymerization using a sacrificial anode, Angew. Chemie - Int. Ed. 54 (2015) 2388–2392. https://doi.org/10.1002/anie.201410598.

[28] A. Walcarius, E. Sibottier, M. Etienne, J. Ghanbaja, Electrochemically assisted self-assembly of mesoporous silica thin films., Nat. Mater. 6 (2007) 602–608. https://doi.org/10.1038/nmat1951.

[29] N. Vilà, J. Ghanbaja, A. Walcarius, Clickable Bifunctional and Vertically Aligned Mesoporous Silica Films, Adv. Mater. Interfaces. 3 (2016) 1–11. https://doi.org/10.1002/admi.201500440.

[30] N. Vilà, J. Ghanbaja, E. Aubert, A. Walcarius, Electrochemically assisted generation of highly ordered azide-functionalized mesoporous silica for oriented hybrid films, Angew. Chemie - Int. Ed. 53 (2014) 2945–2950. https://doi.org/10.1002/anie.201309447.

[31] R. Fernandes, L.Q. Wu, T. Chen, H. Yi, G.W. Rubloff, R. Ghodssi, W.E. Bentley, G.F. Payne, Electrochemically induced deposition of a polysaccharide hydrogel onto a patterned surface, Langmuir. 19 (2003) 4058–4062. https://doi.org/10.1021/la027052h.

[32] V. Lakshminarayanan, L. Poltorak, D. Bosma, E.J.R.R. Sudhölter, J.H. van Esch, E. Mendes, Locally pH controlled and directed growth of supramolecular gel microshapes using electrocatalytic nanoparticles, Chem. Commun. 55 (2019) 9092–9095. https://doi.org/10.1039/c9cc04238e.

[33] L.Q. Wu, A.P. Gadre, H. Yi, M.J. Kastantin, G.W. Rubloff, W.E. Bentley, G.F. Payne, R. Ghodssi, Voltage-dependent assembly of the polysaccharide chitosan onto an electrode surface, Langmuir. 18 (2002) 8620–8625. https://doi.org/10.1021/la020381p.

[34] P.S. Kubiak, S. Awhida, C. Hotchen, W. Deng, B. Alston, T.O. McDonald, D.J. Adams, P.J. Cameron, Polymerization of low molecular weight hydrogelators to form electrochromic polymers, Chem. Commun. 51 (2015) 10427–10430. https://doi.org/10.1039/c5cc03053f.

[35] E.R. Draper, T.O. McDonald, D.J. Adams, Photodimerisation of a coumarin-dipeptide gelator, Chem. Commun. 51 (2015) 12827–12830. https://doi.org/10.1039/c5cc03817k.

[36] E. Palleau, D. Morales, M.D. Dickey, O.D. Velev, Reversible patterning and actuation of hydrogels by electrically assisted ionoprinting, Nat. Commun. 4 (2013) 1–7. https://doi.org/10.1038/ncomms3257.

[37] K. Kaniewska, M. Karbarz, Z. Stojek, Electrochemical attachment of thermo- and pH sensitive interpenetrating-polymers-network hydrogel to conducting surface, Electrochim. Acta. 179 (2015) 372–378. https://doi.org/10.1016/j.electacta.2015.02.196.

[38] V. Urbanova, K. Jayaramulu, A. Schneemann, R.A. Fischer, R. Zbor, Hierarchical Porous Fluorinated Graphene Oxide @ Metal − Organic Gel Composite : Label-Free Electrochemical Aptasensor for Selective Detection of Thrombin, ACS Appl. Mater. Interfaces. 10 (2018) 41089–41097. https://doi.org/10.1021/acsami.8b14344.

[39] J. Das, P. Sarkar, Enzymatic electrochemical biosensor for urea with a polyaniline grafted conducting hydrogel composite modified electrode, RSC Adv. 6 (2016) 92520–92533. https://doi.org/10.1039/C6RA12159D.

[40] L. Liu, M. Etienne, A. Walcarius, Scanning Gel Electrochemical Microscopy for Topography and Electrochemical Imaging, Anal. Chem. 90 (2018) 8889–8895. https://doi.org/10.1021/acs.analchem.8b01011.

[41] N. Dang, M. Etienne, A. Walcarius, L. Liu, Electrochemistry Communications Scanning gel electrochemical microscopy (SGECM): The potentiometric measurements, Electrochem. Commun. 97 (2018) 64–67. https://doi.org/10.1016/j.elecom.2018.10.020.

[42] R. Chen, Y. Li, K. Huo, P.K. Chu, Microelectrode arrays based on carbon nanomaterials: emerging electrochemical sensors for biological and environmental applications, RSC Adv. 3 (2013) 18698. https://doi.org/10.1039/c3ra43033b.

[43] R.W. French, S.N. Gordeev, P.R. Raithby, F. Marken, Paired gold junction electrodes with submicrometer gap, J. Electroanal. Chem. 632 (2009) 206–210. https://doi.org/10.1016/j.jelechem.2009.04.018.

[44] G. Schuszter, T. Gehér-Herczegh, Á. Szucs, Á. Tóth, D. Horváth, Determination of the diffusion coefficient of hydrogen ion in hydrogels, Phys. Chem. Chem. Phys. 19 (2017) 12136–12143. https://doi.org/10.1039/c7cp00986k.

[45] J. Buffle, Z. Zhang, K. Startchev, Metal flux and dynamic speciation at (Bio)interfaces. Part I: Critical evaluation and compilation of physicochemical parameters for complexes with simple ligands and fulvic/humic substances, Environ. Sci. Technol. 41 (2007) 7609–7620. https://doi.org/10.1021/es070702p.

[46] Y. Lu, D. Wang, T. Li, X. Zhao, Y. Cao, H. Yang, Y.Y. Duan, Poly(vinyl alcohol)/poly(acrylic acid) hydrogel coatings for improving electrode-neural tissue interface, Biomaterials. 30 (2009) 4143–4151. https://doi.org/10.1016/j.biomaterials.2009.04.030.

[47] D.H. Kim, J.A. Wiler, D.J. Anderson, D.R. Kipke, D.C. Martin, Conducting polymers on hydrogel-coated neural electrode provide sensitive neural recordings in auditory cortex, Acta Biomater. 6 (2010) 57–62. https://doi.org/10.1016/j.actbio.2009.07.034.

[48] L. Li, L. Pan, Z. Ma, K. Yan, W. Cheng, Y. Shi, G. Yu, All Inkjet-Printed Amperometric Multiplexed Biosensors Based on Nanostructured Conductive Hydrogel Electrodes, Nano Lett. 18 (2018) 3322–3327. https://doi.org/10.1021/acs.nanolett.8b00003.

[49] J. Yan, V.A. Pedrosa, A.L. Simonian, A. Revzin, Immobilizing enzymes onto electrode arrays by hydrogel photolithography to fabricate multi-analyte electrochemical biosensors, ACS Appl. Mater. Interfaces. 2 (2010) 748–755. https://doi.org/10.1021/am9007819.

[50] A. Piper, B.M. Alston, D.J. Adams, A.R. Mount, Functionalised microscale nanoband edge electrode (MNEE) arrays: The systematic quantitative study of hydrogels grown on nanoelectrode biosensor arrays for enhanced sensing in biological media, Faraday Discuss. 210 (2018) 201–217. https://doi.org/10.1039/c8fd00063h.

[51] D.W.M. Arrigan, Nanoelectrodes, nanoelectrode arrays and their applications, Analyst. 129 (2004) 1157–1165.

[52] L. Poltorak, G. Herzog, A. Walcarius, Electrochemically assisted generation of silica deposits using a surfactant template at liquid/liquid microinterfaces, Langmuir. 30 (2014). https://doi.org/10.1021/la501938g.

[53] Y. Liu, A. Holzinger, P. Knittel, L. Poltorak, A. Gamero-Quijano, W.D.A. Rickard, A. Walcarius, G. Herzog, C. Kranz, D.W.M. Arrigan, Visualization of Diffusion within Nanoarrays, Anal. Chem. 88 (2016) 6689–6695. https://doi.org/10.1021/acs.analchem.6b00513.

[54] L. Poltorak, K. Morakchi, G. Herzog, A. Walcarius, Electrochemical characterization of liquid-liquid micro-interfaces modified with mesoporous silica, Electrochim. Acta. 179 (2015) 9–15. https://doi.org/10.1016/j.electacta.2015.01.129.

[55] A. Holzinger, G. Neusser, B.J.J. Austen, A. Gamero-Quijano, G. Herzog, D.W.M. Arrigan, A. Ziegler, P. Walther, C. Kranz, Investigation of modified nanopore arrays using FIB/SEM tomography, Faraday Discuss. 210 (2018) 113–130. https://doi.org/10.1039/c8fd00019k.

[56] G. Herzog, E. Sibottier, M. Etienne, A. Walcarius, Electrochemically assisted self-assembly of ordered and functionalized mesoporous silica films: impact of the electrode geometry and size on film formation and properties, Faraday Discuss. 164 (2013) 259–273. https://doi.org/10.1039/c3fd00021d.

Appendix – Supporting Information

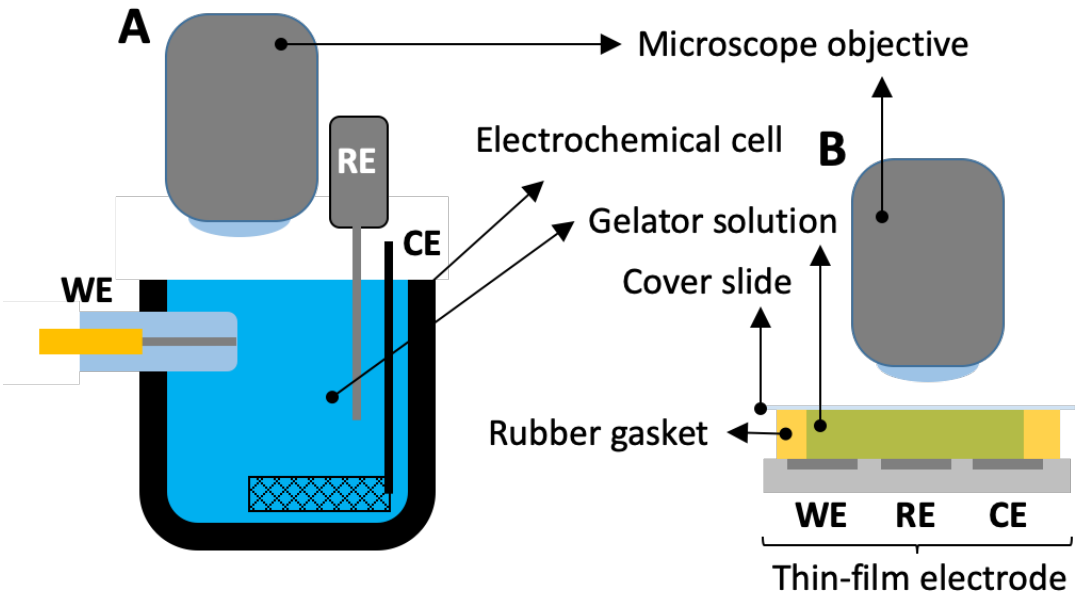

Figure S1. Two electrochemical cells used during the measurements. A – is the setup used to study hydrogel deposition at the macroscopic electrodes with diameters equal to 200 µm and 500 µm. B – is the setup used to investigate array of microelectrodes. WE, RE and CE stands for working, reference and counter electrodes respectively.

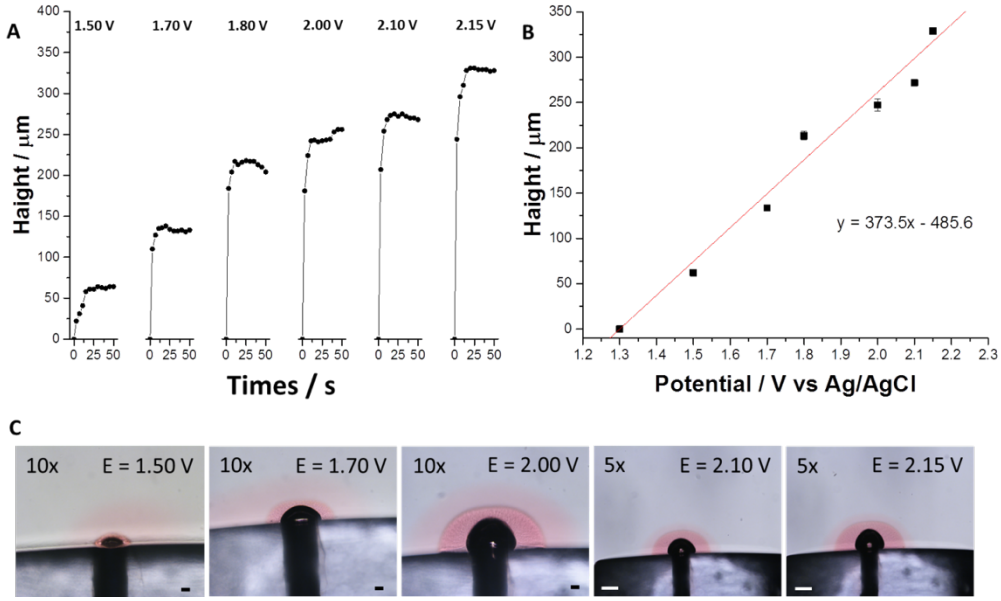

Figure S2. A –Height of a hydrogel deposit for different applied anodic potential values measured for 50 seconds; B – height of the hydrogel deposit in function of applied potential averaged for last 35 deposition seconds; C – optical microscope images for hydrogel deposits recorded at deposition time t = 50 seconds at different applied potential values indicated in upper right corner of each image (the magnification is given in the upper left corner, black and white scale bars correspond to 50 and 200 µm respectively). The concentrations of all reagents are as follow: [Na_2DBC] = 10 mM; [KNO_3] = 500 mM; [Nile red] = 50 µM.

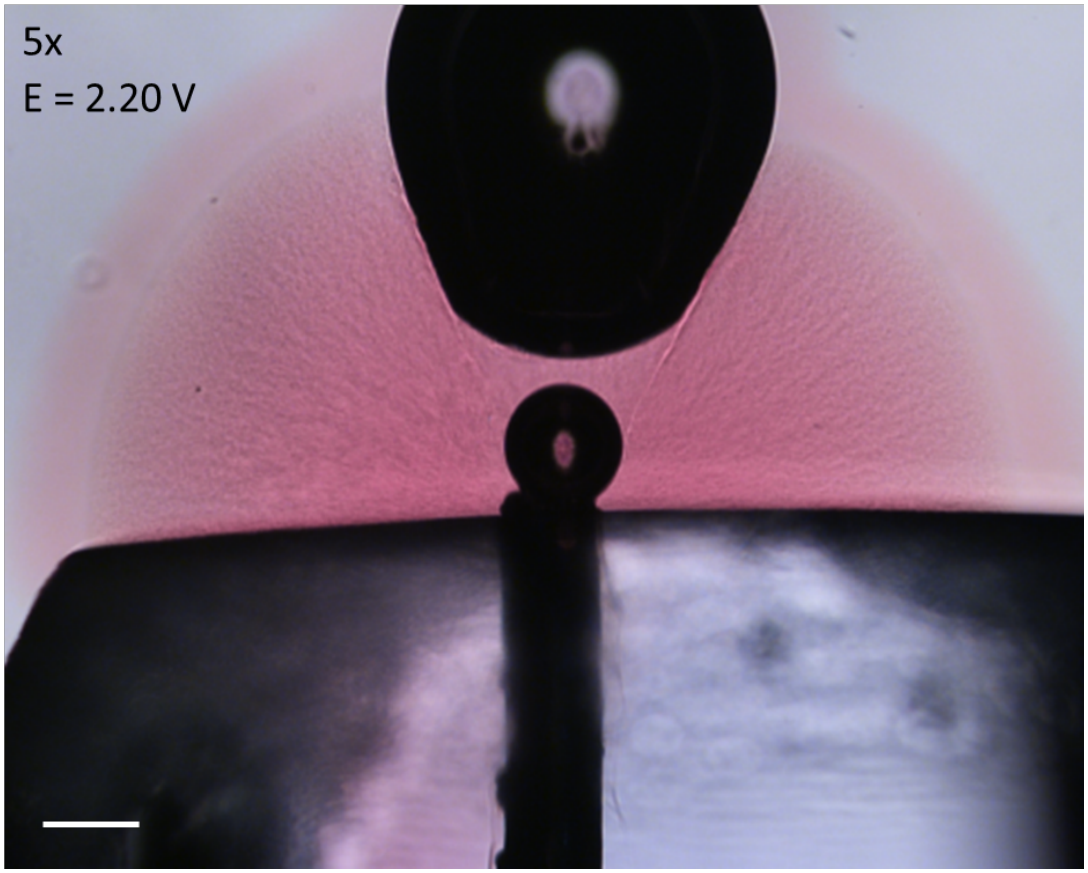

Figure S3. Hydrogel deposition at E = 2.20 V with the Pt electrode having 200 µm in diameter. The concentrations of all reagents are as follow: [Na_2DBC] = 10 mM; [KNO_3] = 500 mM; [Nile red] = 50 µM. The scale bare correspond to 200 µm.

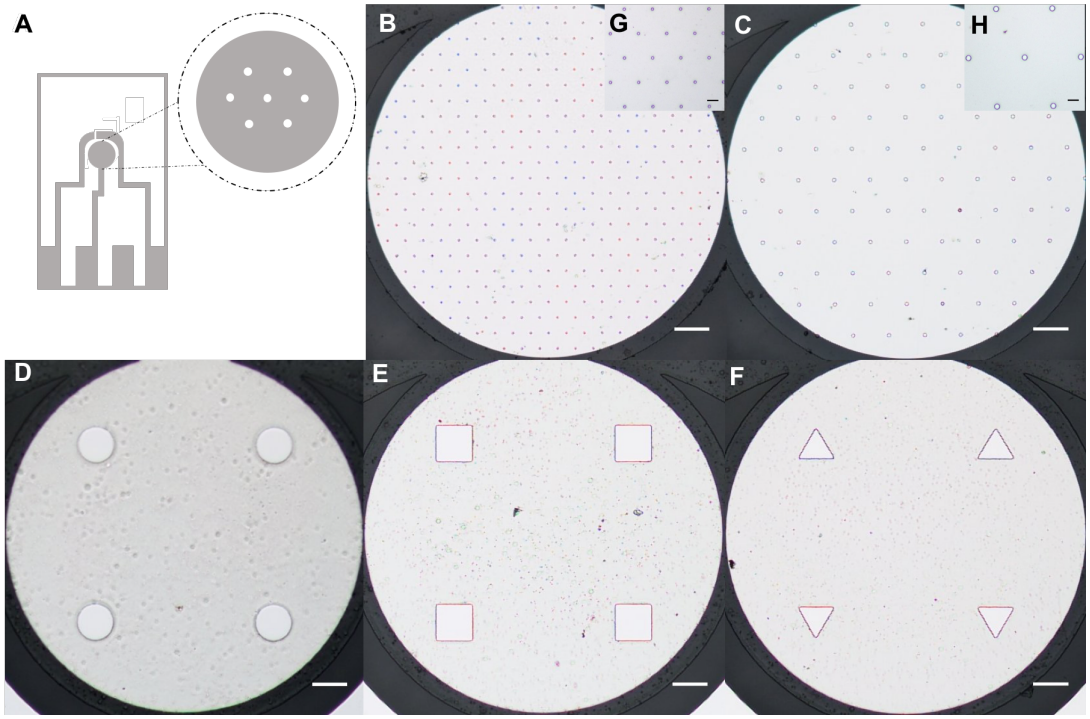

Figure S4. Schematic of chip containing microelectrodes [A], Optical micrographs of microelectrodes produced using lithography, the diameter of the electrodes are 5 [B}, 10 [C] and 100 µm [D] respectively. Different shapes of the electrodes, circle [D], squares [E], triangles [F]. Scale bar is 100 µm. Insets G and H respectively show the hexagonal array design to achieve maximum packing of electrodes on the chip, scale bar is 20 µm

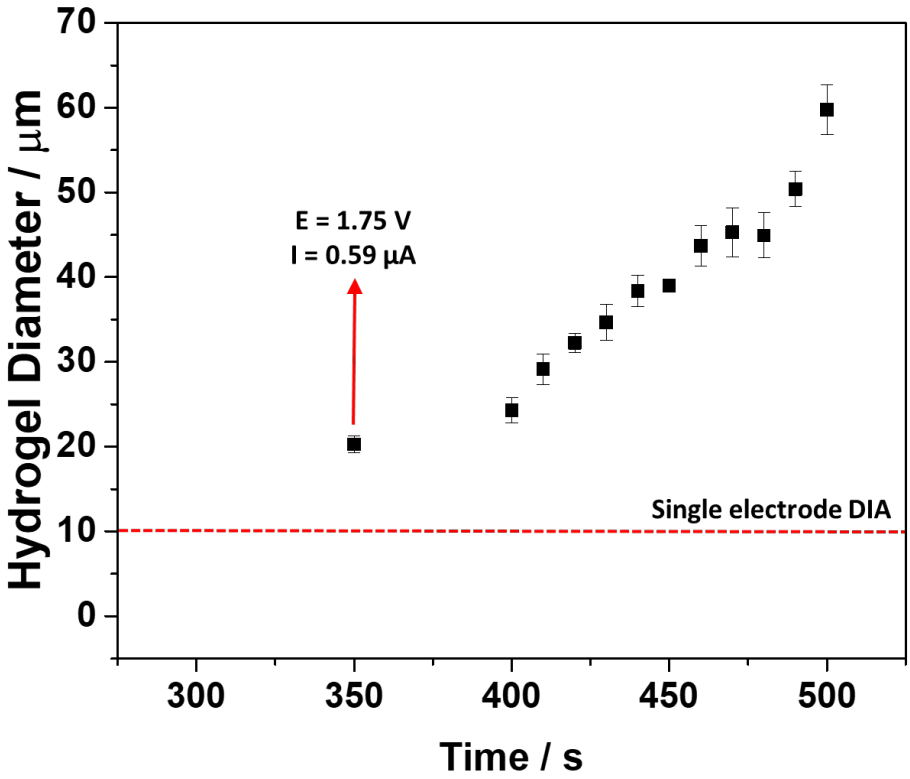

Figure S5. The diameter (DIA) of the hydrogel cups in the function of deposition time (calculated from corresponding linear sweep voltammogram from Figure 4A from the main text). Each point is an average DIA of hydrogel cups growing above seven electrodes forming one hexagon.

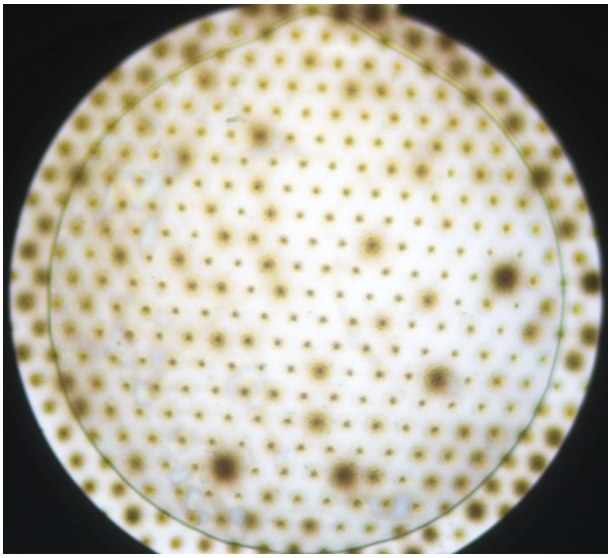

Figure S6. The optical microscopy image taken after hydrogel deposition over the array of Pt microelectrodes having a diameter of 5 µm. The array is covered with the oxygen bubble released due to the hydrogel cup detachment.

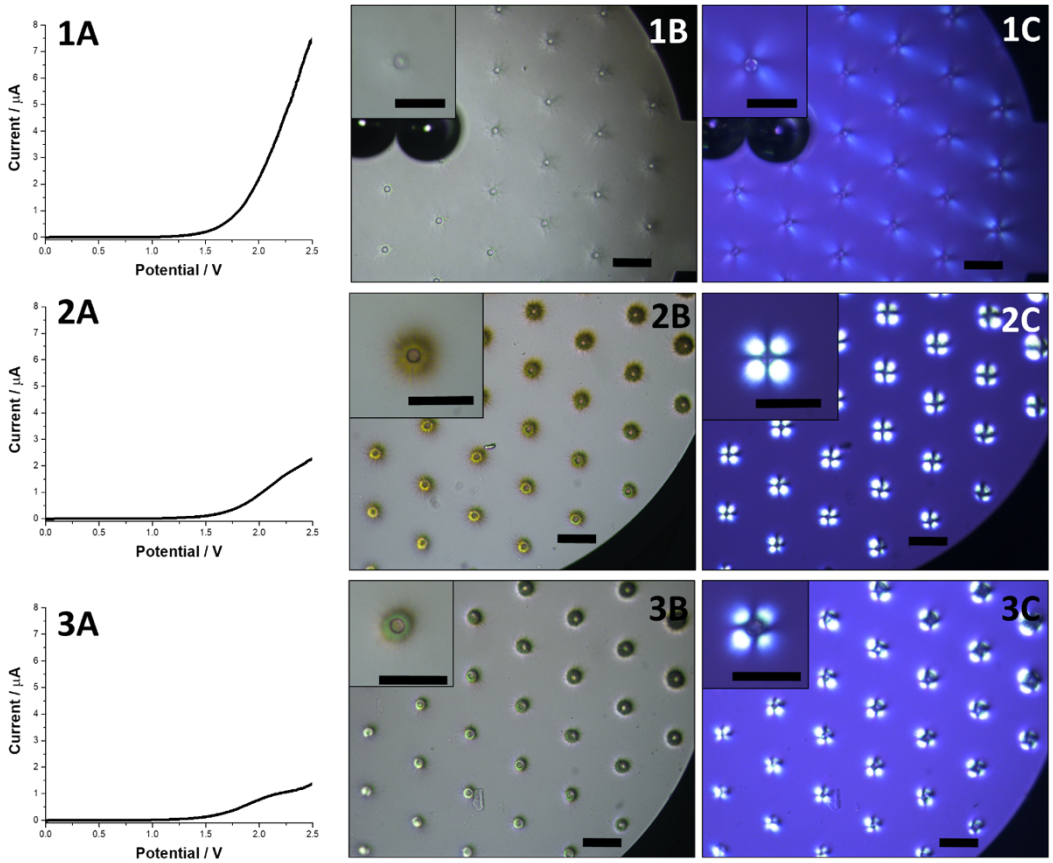

Figure S7. Linear sweep voltammograms recorded for 5 mM (1A); 15 mM (2A); 25 mM (3A) Na_2DBC at 5 mVs^{-1}. Images on the right from the linear sweep voltammograms were recorded under normal and polarization microscopy mode. All scale bars correspond to 50 µm.

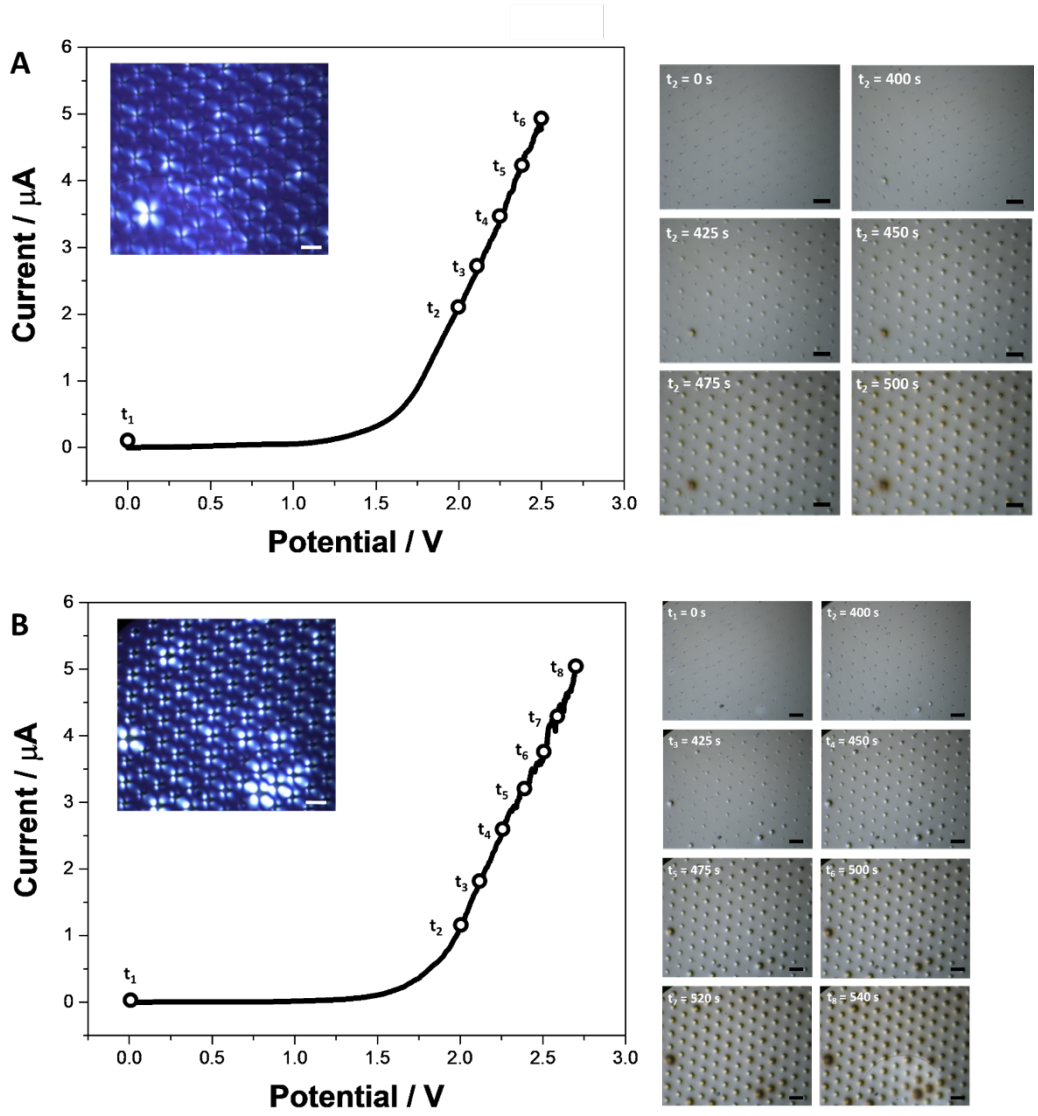

Figure S8. The linear sweep voltammograms recorded in the A – 15 mM and B – 25 mM Na_2DBC solution at 5 mVs^{-1}. On the right from the voltammograms one can find the set of the corresponding optical microscopy images recorded at different deposition times (marked on the upper left corner). The inset of each linear sweep voltammogram is the polarization microscopy image recorded after hydrogel deposition. The scale bars correspond to 50 µm each.

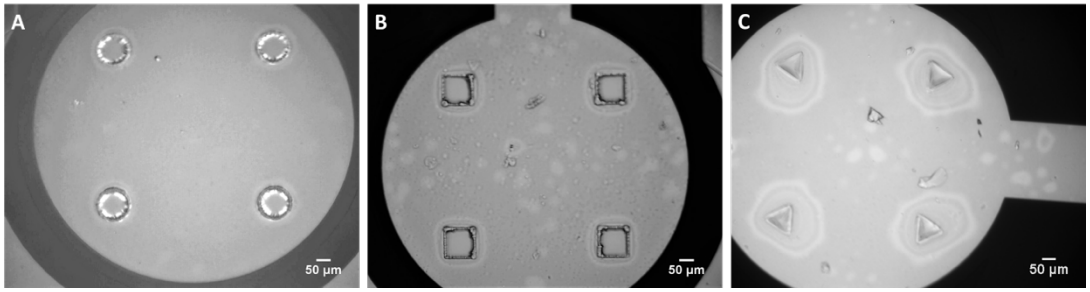

Figure S9. The images showing empty hydrogel circles (A), squares (B) and triangles (C) recorded at the beginning of the deposition process for the electrodes holding micrometre dimensionality (circles DIA = 100 µm, squares and triangles edge = 100 µm). The Na_2DBC was equal to 25 mM. Deposition technique: LSV at 5 mVs^{-1}.

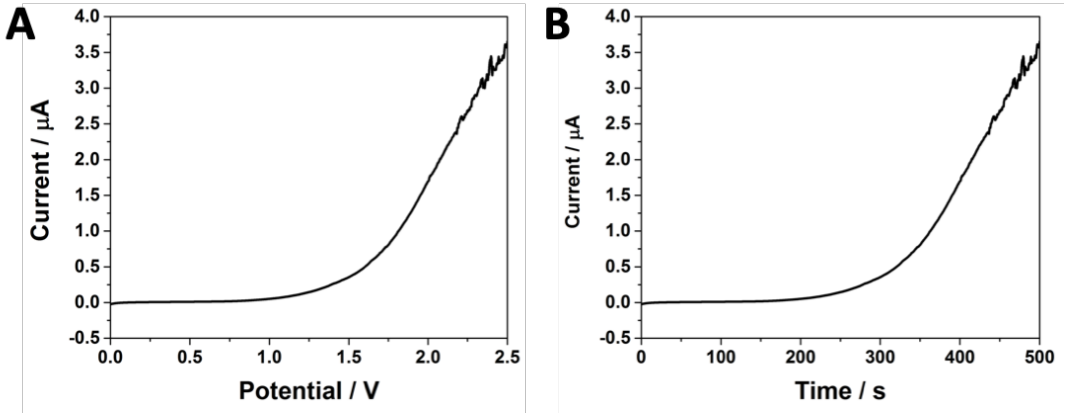

Figure S10. Linear sweep voltammograms (A) and (B) corresponding to movie MS2 for the formation of hydrogel deposit on micro-fabricated Pt electrodes in the shape of squares (edge = 100 µm). The Na_2DBC was equal to 25 mM.

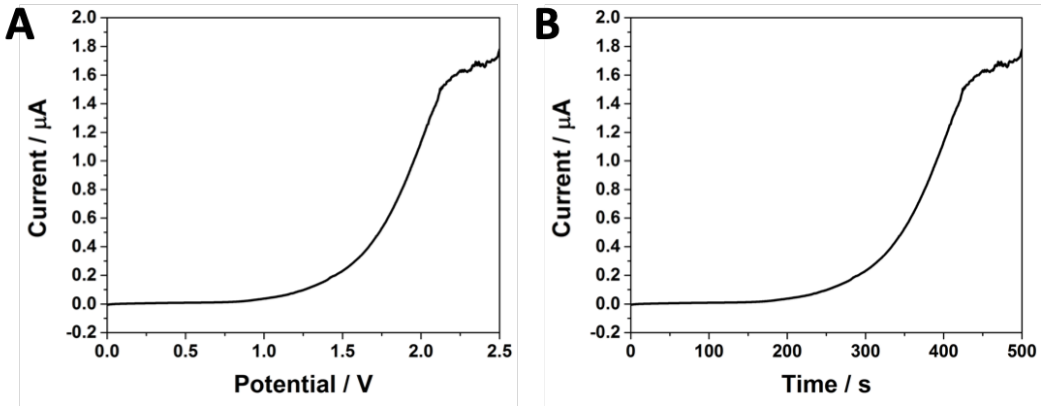

Figure S11. Linear sweep voltammograms (A) and (B) corresponding to movie MS2 for the formation of hydrogel deposit on micro-fabricated Pt electrodes in the shape of triangles (edge = 100 µm). The Na_2DBC was equal to 25 mM.

Chapter 5

Locally pH controlled and directed growth of supramolecular gel microshapes using electrocatalytic nanoparticles

---

Abstract: Controlled localization of platinum nanoparticles (Pt NPs) at the solid support assisted by the polarized liquid – liquid interface is reported. The electro-catalytic water oxidation resulted in the local pH modulation followed by directed self-assembly of Dibenzoyl-L-Cystine hydrogelator forming a structured hydrogel retaining the shape of Pt NPs deposit.

This chapter has been published as V. Lakshminarayanan, L. Poltorak, D. Bosma, E. J. Sudholter, J. van Esch, E. Mendes, *Chem. Commun.* **2019**, DOI 10.1039/C9CC04238E.

5.1 Introduction

Supramolecular hydrogels have been reported to find applications in the fields of cell culturing,[1] drug delivery systems[2] among many others. The ability to exert spatial control over the formation of these materials is therefore of high value. Directed self-assembly of supramolecular hydrogelators composed of low molecular weight gelators has seen a rapid progress in recent years. With the ability to control supramolecular gel formation using pH or catalysts,[3,4] researchers have shown that spatial structuring at the microscale is possible by using light,[5] catalytic surfaces,[6] electrochemistry,[7,8] reaction-diffusion[9] and very recently, charged polymer brushes.[10] However, such approaches need the aid of masks to create patterns, secondary supporting networks to act as reservoirs for the gelator precursors or micro-contact printing to template micropatterns. Hence, new techniques allowing for localized control over hydrogel formation and structuring can pave the way for novel soft material fabrication and patterning. Electrochemical approaches for hydrogel study and formation established so far, although limited to only a few reports, have shown promise due to their ease of use, reversibility or multiplexing ability.[7,11,12] In this work, we take this approach to the next level by demonstrating localized control over hydrogel formation. This is achieved with the help of a polarized liquid-liquid interface to deposit Pt NPs on a conducting substrate of fluorine doped tin oxide (FTO) electrodes. The polarized liquid – liquid interface also known as the interface between two immiscible electrolyte solutions (ITIES) is soft, renewable, free from defects and allows the electrochemical study of interfacial ion or electron transfer processes. The liaison between ITIES and functional materials is a relatively new and unexplored topic.[13] The ion or electron transfer reactions or the self-assembly process can lead to interfacial region modification with a number of functional materials (*e.g.* molecular sieves, liquid mirrors, metal catalysts).[14–16] When the ITIES is contacted to conducting support the so-called three phase junction is formed. At the junction where the three phases meet, the interfacial ion transfer coupled to a redox reaction can result in very precise electrochemical deposition (*e.g.* the formation of Au NPs or silica).[17–19] In this work, we have employed this property to make patterned (rings, stripes and spots) hydrogels by controlled formation of Pt NPs that will act as catalyst for the

electrochemical splitting of water to produce a proton gradient. Controlled and localized Pt NPs deposition at the micro-meter scale is facilitated by the ITIES (micro-capillary supported liquid – liquid interface or by a three-phase junction system). The proton gradient thus produced causes the self-assembly of the hydrogelator Dibenzoyl-L-Cystine (DBC). For simplicity, we have chosen an off-the shelf gelator as a model molecule. We believe that this technology platform gives solid foundation for future electrochemically assisted deposition and writing of supramolecular hydrogels.

5.2 Results and Discussion

First, we focus on the demonstrations that an electro-catalytic effect of Pt NPs on hydrogel formation occurs. The FTO electrode placed in an electrochemical cell (experimental details are available in section 2.1 of the SI) was contacted via a circular opening to a 1 mM aqueous solution of K_2PtCl_6 and the Pt NPs were deposited via chronoamperometry for a period of 10 min. The potential applied (E = – 1.5 V *vs* Ag/AgCl) was sufficient to reduce $PtCl_6^{2-}$ to metallic Pt according to reaction 1 and 2:

$$\mathrm{Pt^{IV}Cl_6^{2-} + 2e^- \rightarrow Pt^{II}Cl_4^{2-} + 2Cl^-} \quad (1)$$

$$\mathrm{Pt^{II}Cl_4^{2-} + 2e^- \rightarrow Pt^0 + 4Cl^-} \quad (2)$$

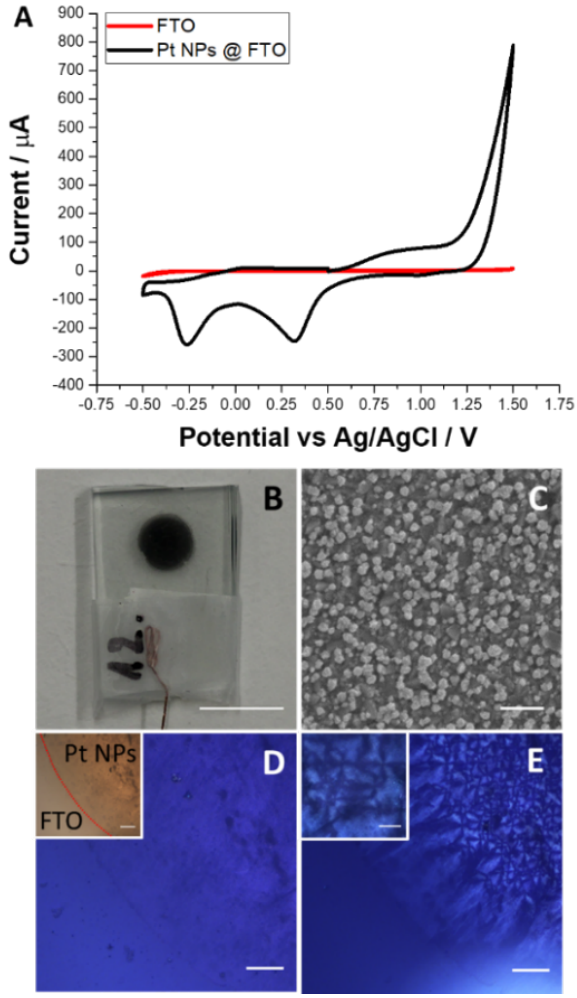

Figure 1. A – Cyclic voltammograms recorded in an aqueous solution of 250 mM $NaNO_3$ before (red) and after (black) Pt NPs deposition at -1.5V via a single step chronoamperometry for 10 min. **B** – is the photo of the corresponding, modified electrode. **C** – shows a SEM image of the area containing Pt NPs. **D** – is the optical microscopy image of the Pt NPs deposited (before hydrogel formation) on FTO under cross-polarized condition (inset shows image under normal light conditions with the boundary of Pt NPs indicated). **E –** is the optical microscopy image recorded under cross-polarization, after hydrogel formation the same FTO surface section is shown in D and E). The inset shows the Maltese cross-hair pattern zoomed in further. Scale bars are: B – 5 mm; C – 1 µm; D, D inset and E – 200 µm; E inset – 100 µm.

Fig. 1B shows the FTO electrode decorated with a dark circle containing Pt NPs. Investigation by scanning electron microscopy (SEM) revealed that the deposited Pt NPs are well dispersed over the support and that their size ranges from 100 to 200 nm (see Fig. 1C and S5 in Appendix). Additional characterization by X-ray photoelectron spectroscopy (XPS) (see Fig. S4 in Appendix) confirmed the presence of metallic Pt. The cyclic voltammograms recorded in aqueous 250 mM $NaNO_3$ before (red line in Fig. 1A) and after deposition of Pt NPs (black line in Fig. 1A) show a clear electro-catalytic effect towards water oxidation. For the latter, the anodic current recorded at 1.5 V was 115 times higher as compared to a non-modified FTO electrode having the same planar surface area. Two additional cathodic peaks recorded around 0.32 V and – 0.26 V are typical fingerprints of oxygen reduction and H^+ adsorption to the Pt electrodes, respectively.[20] The Pt NPs deposited on the FTO substrate were then used for the electrochemically assisted hydrogel deposition experiments. An aqueous 40 mM solution of the sodium salt of the DBC gelator with additionally 250 mM $NaNO_3$ as supporting electrolyte was used. Linear sweep voltammetry was carried out at a scan rate of 10 $mV \cdot s^{-1}$ with the forward polarization towards more anodic potential (typically the experiment was stopped between 2.5 – 3.0 V) and the polarized optical microscopy (POM) was used *in situ* to follow the changes at the surface of the FTO electrode. It is known that DBC gel fibres orient themselves along the diffusion gradient of the protons,[21] and hence, their presence can be followed and confirmed using POM. In Fig. 1D is shown the POM image of the FTO electrode modified with Pt NPs. The boundary between the Pt NPs modified and non-modified region is observed by microscopy as is indicated by the red line (inset in Fig. 1D). The application of a linear increasing anodic potential triggers the water oxidation reaction:

$$2H_2O - 4e^- \rightarrow 4H^+ + O_2 \quad (3)$$

As the local concentration of H^+ increases, we can observe the emergence of the DBC hydrogel (see Fig. 1E together with inset). From the image recorded we conclude that: (i) the hydrogel is built from DBC fibres and structured by the linear diffusion of protons from the

support; (ii) in some of the regions of the support the emergence of so-called Maltese cross patterns indicate the radial orientation of the fibres, which in turn may suggest the presence of the isolated Pt NPs clusters or preferential electro-catalytic sites (behaving as the individual nano-electrodes).[22] The presence of DBC fibres was further confirmed by using Cryo-transmission electron microscopy investigations on electrochemically modified copper grids (see Fig. S9 in Appendix with the corresponding description) decorated with Pt NPs and clearly showed the formation of fibres growing from the Pt NPs surface. In order to control the local deposition of Pt NPs we combined the $PtCl_6^{2-}$ (initially present in the organic phase) transfer reactions across the electrified liquid – liquid interface with its reduction occurring at the FTO. First, we synthesized the organic phase soluble salt – $PtCl_6(BTPPA)_2$ *via* a simple metathesis reaction (see section 1.3 in Appendix for details). We then studied its electrochemical behaviour at the ITIES in a typical four electrode configuration as described in section 2.2 of the Appendix. We expected to find proof of principle that there is a transfer of $PtCl_6^{2-}$. In Fig. 2A shows the ion transfer voltammogram recorded at the interface between the aqueous 10 mM NaCl and 10 mM BTPPATPBCl (hydrophobic salt) dissolved in the 1,2-dichloroethane (the organic phase). The observed potential window is limited by $Na^+_{aq\leftrightarrow org}$ and $Cl^-_{aq\leftrightarrow org}$ transfer on the more and less positive potential sites, respectively. Addition of $PtCl_6(BTPPA)_2$ at µM concentration to the organic phase results in the emergence of two peaks with $E_{1/2}$ = 0.25 V within the available potential window (Fig. 2B). The positive peak is attributed to the $PtCl^{2-}_{6,org\rightarrow aq}$. The ratio of the integrated positive and negative signals approaching unity indicate the reversibility of the process.

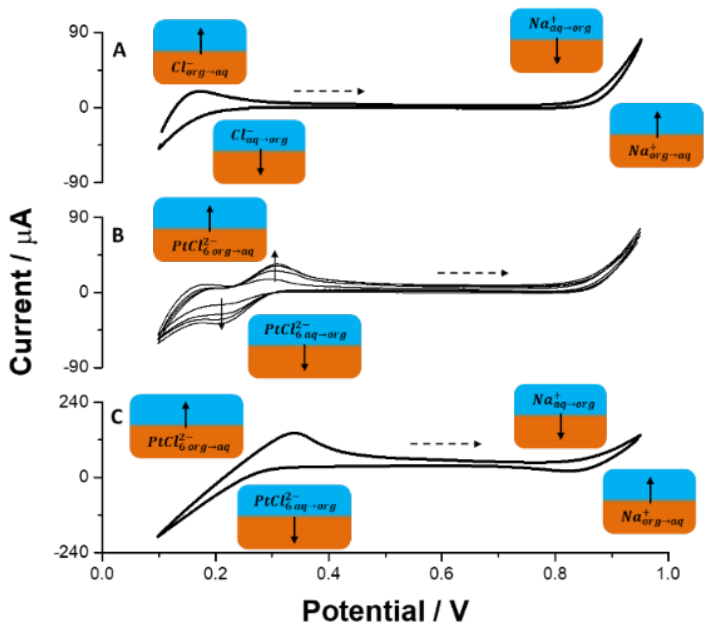

Figure 2. Ion transfer voltammograms recorded at the Liquid-liquid Interface formed between **A** – 10 mM NaCl (aq) // 10 mM BTPPATPBCl (org); **B** – 10 mM NaCl (aq) // x µM (x = 58; 116; 174 and 232 µM) $BTPPA_2PtCl_6$ in 10 mM BTPPATPBCl (org) and **C** – 10 mM NaCl (aq) // 5 mM $BTPPA_2PtCl_6$ (org). Scan rate was 10 mVs^{-1}; dashed arrow indicate the direction of the forward scan.

In Fig. 2C shows the recordings when the organic phase contained only 5 mM $PtCl_6(BTPPA)_2$ (the concentration used in further experiments) and shows the potential window, which is now limited on the negative potential side by the $PtCl^{2-}_{6,aq\leftrightarrow org}$. The concept of a three phase junction modification was mainly studied in the group of Opallo, where Au NPs or silica material were electrochemically generated in a defined locus.[17–19] To the best of our knowledge, this is the first time that the three phase junction is decorated with Pt NPs. The modification follows a few mutually related ion and electron transfer reactions that are depicted together with the electrical scheme in Fig. 3. First the reductive potential is applied to the FTO electrode and the $PtCl_6^{2-}$ present in the organic phase undergoes a reduction to metallic Pt (according to reaction 1 and 2) at the three phase

junction. For an applied potential (E = – 1.5V) its reduction in the organic phase is unlikely due to very high resistance of the circuit (high resistivity of the organic phase and the position of the reference electrode), and is therefore excluded. The Cl^- formed within the junction or on the organic side of the ITIES will partition to the aqueous phase due to its high intrinsic hydrophilicity:

$$\mathrm{Cl^-_{ITIES\ or\ org}} \rightarrow \mathrm{Cl^-_{aq}} \tag{4}$$

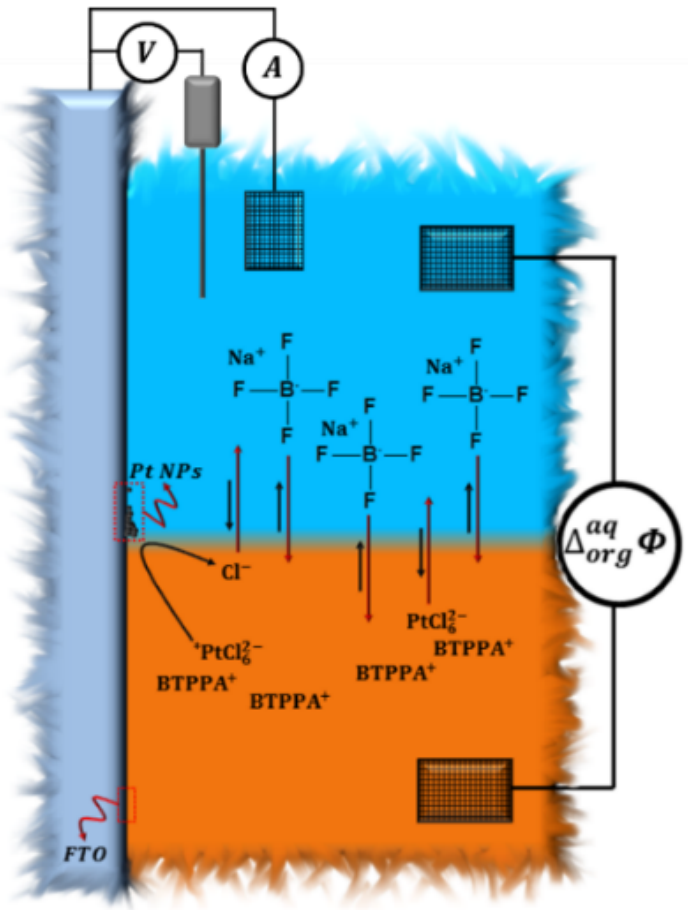

Figure 3. Schematic representation of the three-phase junction system. Organic phase is 1.2-dichloroethane. For details refer to text.

In order to maintain the charge-balance, the anion (still soluble in the aqueous phase and significantly less hydrophilic than Cl^-) from the aqueous phase should transfer to the organic phase. This was provided with unidirectional BF_4^- transfer:

$$\mathrm{BF}_{4,\mathrm{aq}}^- \rightarrow \mathrm{BF}_{4,\mathrm{org}}^- \quad (5)$$

As confirmed with the control experiment, in the absence of a charge balancing ion, the reaction 1, 2 and 4 will not occur and no deposit will be found (data not shown). Although $PtCl_6^{2-}$ is more hydrophobic than BF_4^- ($logP^0_{DCE,BF_4^-}$ = 3.4[23] < $logP^0_{DCE,PtCl_6^{2-}}$ = 5.1 – as calculated in section 3 of the Appendix) we found that for experimental concentrations of $[BF_{4,aq}^-]$ = 100 mM and $[PtCl_6^{2-}]$ = 5 mM the latter was partitioning from the organic to the aqueous phase (clear colour change of the aqueous phase was observed over time):

$$\mathrm{PtCl}_{6,\mathrm{org}}^{2-} \rightarrow \mathrm{PtCl}_{6,\mathrm{aq}}^{2-} \quad (6)$$

Whenever the $PtCl_6^{2-}$ will diffuse towards the cathodically polarized FTO electrode the reaction 1 and 2 will occur. To demonstrate the control over directed self-assembly of hydrogelators, different configurations of FTO substrate and liquid-liquid interface were made (see Fig. 4, row A). The detailed experimental information can be found in sections 2.2 – 2.5 of the Appendix. Three designs were implemented to control the localization of Pt NPs: i) design where the conductive substrate was dipped into the organic phase (solution of 5 mM $BTPPA_2PtCl_6$ in 1,2-DCE) and contacted with the aqueous phase on top (Fig. 4 – A1) ; ii) design where a micro-droplet of the organic phase containing 5 mM $BTPPA_2PtCl_6$ is casted on top of the FTO substrate (Fig. 4 – A2); iii) design where a micro-capillary filled with the organic phase is positioned close to the FTO substrate (Fig. 4 – A3).

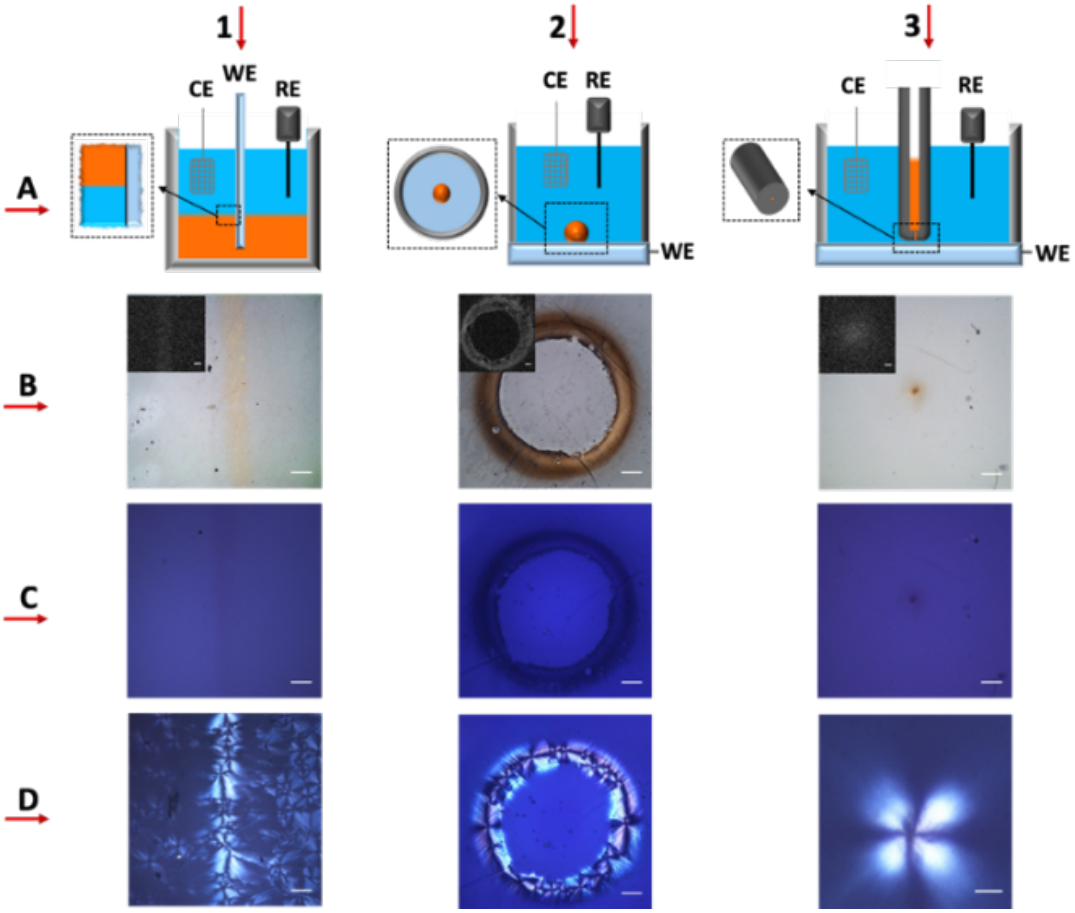

Figure 4. Three configurations used for localized Pt NPs deposition **1A** – scheme of a three phase junction for stripe deposition; **1B** – scheme of a three phase junction for ring deposition and **1C** – scheme of a micro-capillary supporting ITIES for micro-spot deposition. **Panel B** correspond to optical microscopy images (insets show the Energy Dispersive X-ray Spectroscopy mapping of Pt). **Panels C and D** represent polarization microscopy images before and after hydrogel deposition, respectively. The columns 1, 2 and 3 shows the results for stripe, ring and micro-spot respectively. Scale Bars are: 100 µm (left to right, B1 - B3, C1 - C3, D1 - D2) and 50 µm (D3) respectively.

In the first two designs, the formation of Pt NPs occurs at the three-phase junction while in the third design, this junction is absent and the Pt NPs are produced by transfer of $PtCl_6^{2-}$ from the organic to aqueous phase followed by its reduction at the FTO substrate. The Pt NPs reach micro-patterns that result from the designs are in the form of a stripe (*ca*

175 µm), ring (*ca* 1.5mm diameter, 225 µm thick rim) and a spot (*ca* 60 µm diameter) respectively (Fig. 4 panel B). It was also observed that the width of the pattern was dependent on the deposition time (data not shown). The presence of the Pt NPs was confirmed in all three cases via SEM (Fig. S8 in Appendix) in combination with EDS elemental mapping (inset Fig. 4 row B).

The formation of hydrogels from these patterns was carried out using linear sweep voltammetry (see section 2.6 of Appendix). It can be seen (Fig. 4 image 1D, 2D and 3D) that there is birefringence under cross-polarization indicating formation of oriented fibres. The time evolution of the hydrogel pattern together with a linear sweep voltammogram is shown in Fig. S10 (see Appendix) . From the nature of the polarization pattern, it can be concluded that the DBC fibres are oriented radially outward based on the diffusion of the protons (towards a bulk phase) produced at the interface of Pt NP catalyst and the aqueous gelator environment. The produced hydrogels retain their shape of the base micro-pattern while being broader. Especially interesting is the hydrogel deposition obtained over a micro-spot as shown in Fig. 4 panel 3. As the region filled with Pt NPs has micrometre size, it resembles a single microdisc electrode, at which the mass transport (to and from the electrode) will be governed by a hemispherical diffusion. Very prominent and clear Maltese cross patterns indicate that the formed hydrogel has radial orientation and probably dome-like shape. This observation is in line with similar hemispherical shapes of silica,[24–26] metallic[27] or polymeric[28] deposits obtained over an array of nano- and micro-electrodes.

5.3 Conclusions

Electrochemically controlled Pt NPs deposition proposed in this work was used to produce sophisticated hydrogel patterns by combining them with supramolecular hydrogelators. Polarized liquid – liquid interface was used to control localization of Pt NPs, thereby creating new opportunities to design complicated and unusual gel patterns in a very straightforward manner. The electro-catalytic effect of Pt NPs towards water oxidation allowed the local pH change that triggered the growth of structured hydrogel directly from the support.

Electrochemical patterning of hydrogels using the technique developed in this work can be used as a platform to create functional soft matter down to micro- or nano-metre scale. As such, it opens new gel processing directions with potential applications in cell culturing, drug delivery, tissue engineering, sensing, diagnostics *etc.* Such an approach may be used to produce nano-patterned electro responsive surfaces capable of templating hydrogels and other functional soft materials.

References

1 V. Jayawarna, M. Ali, T. A. Jowitt, A. F. Miller, A. Saiani, J. E. Gough and R. V. Ulijn, *Adv. Mater.*, 2006, **18**, 611–614.

2 A. Friggeri, B. L. Feringa and J. van Esch, *J. Control. Release*, 2004, **97**, 241–8.

3 J. Boekhoven, J. M. Poolman, C. Maity, F. Li, L. van der Mee, C. B. Minkenberg, E. Mendes, J. H. van Esch and R. Eelkema, *Nat. Chem.*, 2013, **5**, 433–7.

4 F. Trausel, F. Versluis, C. Maity, J. M. Poolman, M. Lovrak, J. H. Van Esch and R. Eelkema, , DOI:10.1021/acs.accounts.6b00137.

5 C. Maity, W. E. Hendriksen, J. H. van Esch and R. Eelkema, *Angew. Chemie*, 2015, **127**, 1012–1015.

6 A. G. L. Olive, N. H. Abdullah, I. Ziemecka, E. Mendes, R. Eelkema and J. H. van Esch, *Angew. Chemie Int. Ed.*, 2014, **53**, 4132–4136.

7 Y. Liu, E. Kim, R. V. Ulijn, W. E. Bentley and G. F. Payne, *Adv. Funct. Mater.*, 2011, **21**, 1575–1580.

8 J. Raeburn, B. Alston, J. Kroeger, T. O. McDonald, J. R. Howse, P. J. Cameron and D. J. Adams, *Mater. Horiz.*, 2014, **1**, 241–246.

9 M. Lovrak, W. E. J. Hendriksen, C. Maity, S. Mytnyk, V. van Steijn, R. Eelkema and J. H. van Esch, *Nat. Commun.*, 2017, **8**, 15317.

10 Y. Wang, S. Oldenhof, F. Versluis, M. Shah, K. Zhang, V. van Steijn, X. Guo, R. Eelkema and J. H. van Esch, *Small*, 2019, 1804154.

11 E. R. Cross and D. J. Adams, *Soft Matter*, 2019, **15**, 1522–1528.

12 M. Zelzer and R. V Ulijn, *Chem. Soc. Rev.*, 2010, **39**, 3351–7.

13 L. Poltorak, A. Gamero-Quijano, G. Herzog and A. Walcarius, *Appl. Mater. Today*, 2017, **9**, 533–550.

14 L. Poltorak, K. Morakchi, G. Herzog and A. Walcarius, *Electrochim. Acta*, 2015, **179**, 9–15.

15 E. Smirnov, P. Peljo, M. D. Scanlon, F. Gumy and H. H. Girault, *Nanoscale*, 2016, **8**, 7723–7737.

16 T. J. Stockmann, L. Angel, V. Brasiliense, C. Combellas and F. Kanoufi, *Angew. Chemie Int. Ed.*, 2017, **56**, 13493–13497.

17 J. Niedziolka and M. Opallo, *Electrochem. Commun.*, 2008, **10**, 1445–1447.

18 I. Kaminska, M. Jonsson-niedziolka, A. Kaminska, M. Pisarek, R. Ho, M. Opallo and J. Niedziolka-jonsson, *J. Phys. Chem. C*, 2012, **116**, 22476–22485.

19 I. Kaminska, J. Niedziolka-jonsson, A. Roguska and M. Opallo, *Electrochem. commun.*, 2010, **12**, 1742–1745.

20 D. Huang, B. Zhang, J. Bai, Y. Zhang, G. Wittstock, M. Wang and Y. Shen, *Electrochim. Acta*, 2014, **130**, 97–103.

21 I. Ziemecka, G. J. M. Koper, A. G. L. Olive and J. H. van Esch, *Soft Matter*, 2013, **9**, 1556.

22 D. W. M. Arrigan, *Analyst*, 2004, **129**, 1157–1165.

23 M. Suzuki, S. Kihara, K. Maeda, K. Ogura and M. Matsui, *J. Electroanal. Chem.*, 1990, **292**, 231–244.

24 Y. Liu, A. Holzinger, P. Knittel, L. Poltorak, A. Gamero-Quijano, W. D. a. W. D. A. W. D. a Rickard, A. Walcarius, G. G. Herzog, C. Kranz and D. W. M. M. D. W. M. Arrigan, *Anal. Chem.*, 2016, **88**, 6689–6695.

25 L. Poltorak, G. Herzog and A. Walcarius, *Langmuir*, , DOI:10.1021/la501938g.

26 A. Holzinger, G. Neusser, B. J. J. Austen, A. Gamero-Quijano, G. Herzog, D. W. M. Arrigan, A. Ziegler, P. Walther and C. Kranz, *Faraday Discuss.*, 2018, **210**, 113–130.

27 C. Zhu, G. Meng, Q. Huang, Z. Li, Z. Huang, M. Wang and J. Yuan, *J. Mater. Chem.*, 2012, **22**, 2271–2278.

28 Y. Sakurai, S. Okuda, H. Nishiguchi, N. Nagayama and M. Yokoyama, *J. Mater. Chem.*, 2003, **13**, 1862–1864.

Appendix – Supporting Information

1. Materials:

Sodium Nitrate ($NaNO_3$) (98.5%, Sigma Aldrich), Sodium Chloride (NaCl) (99%, Sigma Aldrich), Potassium Hexachloroplatinate (K_2PtCl_6) (99.9%, Sigma Aldrich) , Sodium Tetrafluoroborate ($NaBF_4$) (97%, Sigma Aldrich), Nitric Acid (HNO_3) (60%, Sigma Aldrich), Hydrochloric Acid (HCl) (1M, Sigma Aldrich)) , Sodium Hydroxide (NaOH) (99%,Pellets, Sigma Aldrich), Dibenzoyl-L-Cystine (DBC) (98%, Sigma Aldrich), Tetramethylammonium Chloride (TMA-Cl) (98%, Sigma Aldrich), Potassium Tetrakis(4-chlorophenylborate) (97%, Sigma Aldrich) (K^+TPBCl), Bis(triphenylphosphoranylidene)ammonium Chloride (BTPPA-Cl) (97%, Sigma Aldrich), Chlorotrimethylsilane (99%, Sigma Aldrich) , 1,2-Dichloroethane (1,2-DCE) (Solvent grade, VWR International), Ethanol (Solvent grade, Biosolve), Methanol (Solvent grade, VWR International) and Acetone (Solvent grade, Biosolve) were obtained from commercial suppliers. Salts Na_2-DBC, BTPPA-TPBCl, and $(BTPPA)_2PtCl_6$ were synthesized according to protocols described below.

1.1 Na_2-DBC protocol of preparation

Sodium salt of the gelator (DBC) was prepared by titrating acidified gelator against 0.1 M NaOH (1:2 molar ratio). The solution contained neutralized and non-neutralized gelator was passed through an Acrodisc syringe filter (0.2 µm, PTFE membrane) to remove any possible impurities and non-neutralized gelator which was present as white precipitate in the solution. The resulting clear solution was checked for turbidity and freeze dried under vacuum to yield a white flaky powder which was used for further experiments.

1.2 BTPPA-TPBCl protocol of preparation

BTPPA-TPBCl was used as the organic phase (1,2-dichloroethane) supporting electrolyte and was prepared by simple metathesis reaction reported elsewhere.[1] In brief, 0.6 g of BTPPA-Cl dissolved in 25 mL of water:methanol (1:2 v:v) was added dropwise to a vigorously stirred solution of 0.5 g of K-TPBCl dissolved in water:methanol mixture (1:2 v:v). Resulting white precipitate was than filtered under vacuum and washed with 100 mL of water:methanol (1:2

v:v) mixture. Next, white precipitate was recrystallized from acetone giving large and transparent crystals. After washing with 50 mL of water:acetone (1:1 v:v) mixture it was dried under vacuum and used in experiments.

1.3 $(BTPPA)_2PtCl_6$ protocol of preparation

$(BTPPA)_2PtCl_6$ was used as the organic phase soluble salt of the Pt NPs precursor $PtCl_6^{2-}$. Its preparation is similar to already described BTPPA-TPBCl. The only difference is the ratio between BTPPA-Cl to K_2PtCl_6 equal to 1.1 g to 1.9 g, respectively. The resulting salt had an appearance of orange flakes very well soluble in the 1,2-DCE.

2. Electrochemical experiments

The electrochemical experiments described in the main text of this work and in the supporting information were performed in different electrochemical configurations using few types of custom-made electrochemical cells. All electrochemical experiments were performed using Potentiostat/Galvanostat Autolab 302N or portable potentiostat EmStat3+ from PalmSens that were controlled with the Nova 1.10 or PSTrace software respectively.

2.1 Pt NPs deposition in three-electrode configuration

The Pt NPs deposition over Fluorine-doped tin oxide (FTO) was performed in a three-electrode configuration using dedicated Teflon cell shown in **Fig. SI1-A**. The FTO served as the working electrode, Ag/AgCl was used as the reference electrode whereas 5 cm long Pt wire served as the counter electrode. The cell itself allowed the position of a FTO electrode between O-ring terminated cell and a plate that was attached to the cell body via two screws. The electroactive surface area was defined by O-ring with a diameter equal to 5 mm. Chronoamperometry at $E = -1.5$ V was used for the electrochemical deposition of Pt NPs from 1 mM K_2PtCl_6 in 250 mM $NaNO_3$. Further characterization of Pt NPs was performed with cyclic voltammetry at scan rate equal to 50 $mV \cdot s^{-1}$ in 250 mM $NaNO_3$.

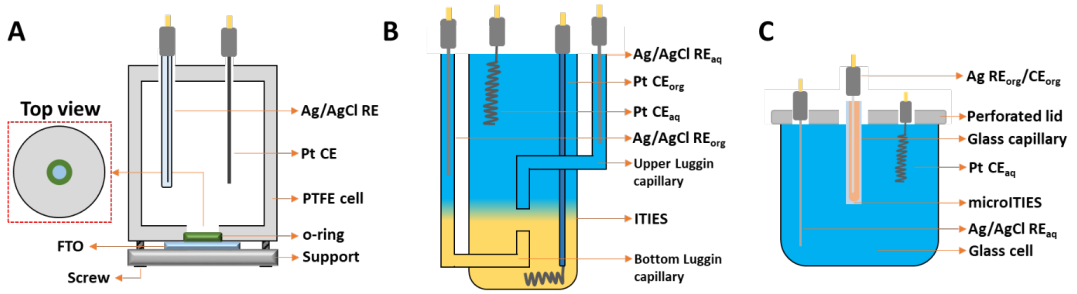

Figure S1. Different electrochemical cells used in this work. **A** – is the cell used to modify FTO electrode with the Pt NPs; **B** – is the "cactus like" cell to study interfacial behaviour of $BTPPA_2PtCl_6$ at macroscopic liquid – liquid interface and **C** is the cell used to characterize micropipettes that were used to support micro-liquid-liquid interface. The abbreviations used stand for: **PTFE** – polytetrafluoroethylene, **RE** – reference electrode, **CE** – counter electrode, **aq** – the aqueous phase, **org** – the organic phase and **ITIES** – the interface between two immiscible electrolyte solutions.

2.2 Macroscopic electrified liquid – liquid interface

Experiments at the macroscopic liquid – liquid interface were performed in four-electrode configuration in the "Cactus like" glass cell with two Luggin capillaries **(see Fig S1B).** The geometrical diameter of a liquid – liquid interface placed in this cell was equal to 0.65 cm. The counter electrodes were made out of Pt spiral wires. The organic phase counter electrode was additionally sealed in glass to prevent the contact with the aqueous phase. Both, the organic and the aqueous phase reference electrodes were made out of Ag/AgCl wires. During experiments, the organic phase reference electrode was immersed into the solution of 10 mM NaCl, 10 mM BTPPA-Cl that was contacted to the organic phase in the bottom Luggin capillary. Typical composition of a cell can be denoted with a following scheme:

$$(aq)\ Ag\ \Big|AgCl\Big|^{10\ mM\ \ NaCl}\Big|\Big|^{10\ mM\ BTPPA-TPBCl}_{x\ \mu M/mM\ BTPPA_2PtCl_6}\Big|^{10\ mM\ NaCl}_{10\ mM\ BTPPA-Cl}|AgCl|Ag\ (org)$$

Scheme 1. Electrochemical cell used at macroscopic liquid – liquid interface. Double line indicates liquid – liquid interface under investigation.

Ion transfer voltammetry was used to characterize the interfacial behaviour of $BTPPA_2PtCl_6$ dissolved in the organic phase. The forward polarization was from more positive to less positive potential values. The scan rate was equal to 10 $mV \cdot s^{-1}$.

2.3 Miniaturized electrified liquid – liquid interface

Miniaturization was achieved with the help of metal templated glass-micro-capillaries.[2,3] In brief, the gold μ-wire with diameter equal to 25 μm was sealed in a glass capillary (ID: 1.6 mm and OD: 2.0 mm) upon heating in Bunsen burner flame. Attention has to be taken to entrap only part of the wire. Next, gradual polishing with fine polish paper allowed the removal of glass excess until μ-wire is exposed (**see Figure S2**). Following that, gold μ-wire was dissolved in aqua-regia (3:1 HCl:HNO_3) and the capillary has been washed few times with miliQ water (see empty pore in the inset of **Figure S2**). In order to assure that only the organic phase will be present inside the pore during the experiments, the internal walls of the pore were modified with trimethylsilyl groups via chemical vapor deposition of chlorotrimethylsilane.

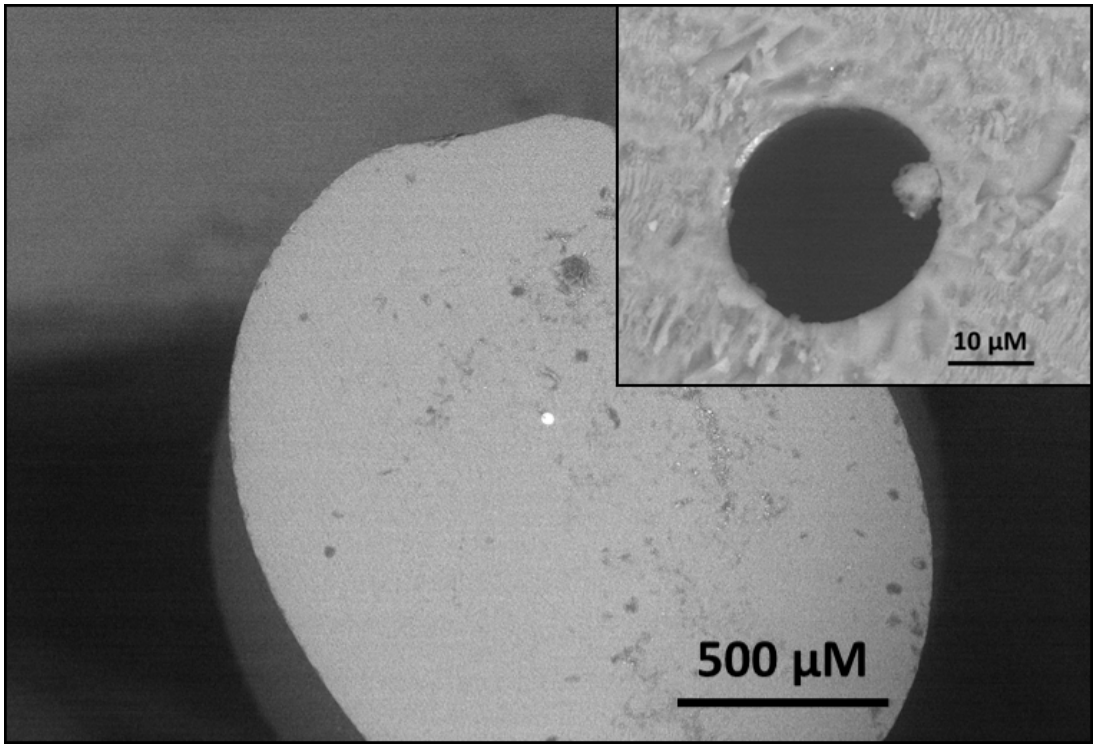

Figure S2. SEM image of the gold µ-wire (25 µm in diameter) embedded in glass after polishing. Insert shows the µ-pore formed after gold wire dissolution in *aqua regia*.

Four electrode configuration was used to polarized miniaturized liquid – liquid interface. The organic phase was placed inside the capillary and then silver wire working as the organic phase counter and pseudo-reference electrode was inserted (see **Figure S1C**). The capillary together with the connection was placed in the aqueous phase through a hole in a lid of a glass cell. The Ag/AgCl and spiral Pt wire were used as the aqueous phase reference and counter electrodes respectively. The electrochemical cell can be described using scheme 2:

$$(aq)\ Ag\ \Big|AgCl\ \Big|\begin{matrix}10\ mM & NaCl\\ x\mu M & TMA-Cl\end{matrix}\Big|\Big|\begin{matrix}10\ mM\ BTPPA-TPBCl\\ in\ 1{,}2-DCE\end{matrix}|Ag\ (org)$$

Scheme 2. Electrochemical cell used at miniaturized liquid – liquid interface. Double line indicates liquid – liquid interface under investigation.

The micro-capillaries used for local Pt NPs deposition were first characterized using ion transfer voltammetry as shown in **Figure S3**. The blank voltammogram (**Figure S3A**) was recorded in the cell described in scheme 2 for x = 0. Here, the forward polarization was from less positive to more positive potential values (scan rate 10 $mV{\cdot}s^{-1}$). In this graph, the potential window is limited on both sides by the transfer of the aqueous phase background electrolyte ions. Positive and negative currents on the more positive potential site arise from the Na^+ transfer to the organic phase and back to aqueous phase, respectively. The interfacial transfer of Cl^- is limiting the negative side of the potential window. Here, the negative and the positive currents are due to Cl^- transfer to the organic and back to the aqueous phase, respectively. After adding TMA-Cl to the aqueous phase (Scheme 2, x = 40 µM) we recorded voltammogram shown in **Figure S3B**. The voltammetric response is asymmetric, this is sigmodal wave on the forward scan and peak shaped signal on the reversed scan, and is in agreement with the asymmetric diffusion layer profiles established on both sides of the liquid – liquid interface (see insets of **Figure S3B**).

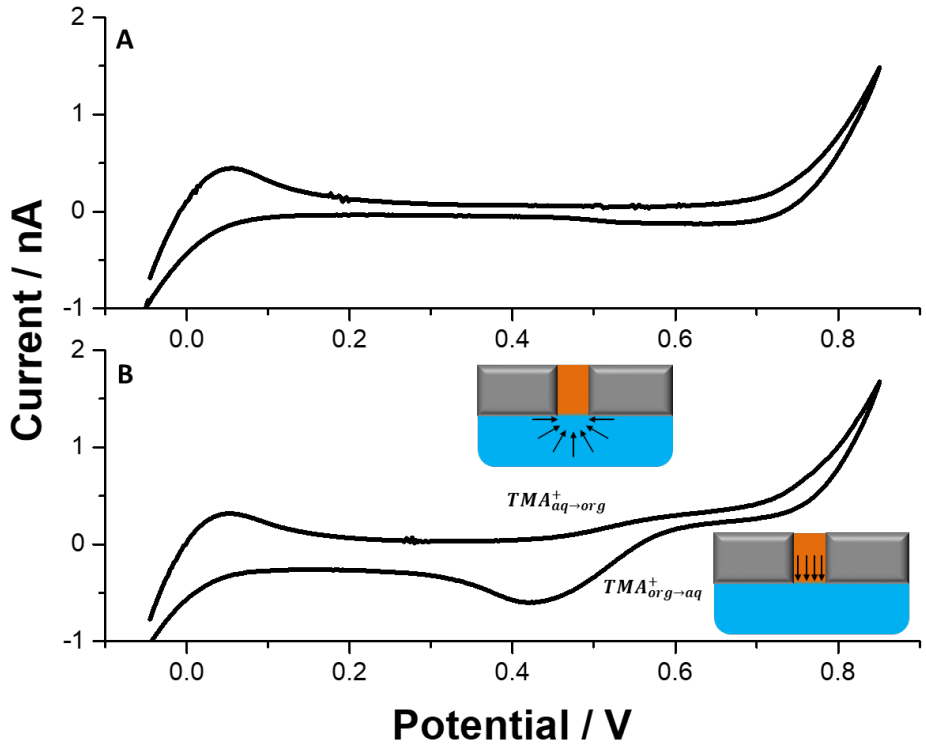

Figure S3. Ion transfer voltammograms recorded at the micro-pore supported interface between 10 mM NaCl and 10 mM $BTPPA^+TPBCl^-$ in the absence (A) and in the presence (B) of 40 µM TMA^+Cl^-. The current of the forward wave (0.25 nA) correspond to pore radii equal to 12 µm (24 µm in diameter).

The transfer of ions from the aqueous to the organic side of the interface is analogical to the mass transfer of an analyte towards micro-disc electrode, and hence, can be described with the Saito expression:

$$I_{ss} = 4nFDCr \quad \text{(eq. 1)}$$

where I_{ss} is the faradaic current (steady state current), n is the molecular charge, r is radius of a capillary, D is the TMA^+ diffusion coefficient ($13.8 \cdot 10^{-6}$ $cm \cdot s^{-2}$)[4] and C is the concentration of an analyte. Simple rearrangement of the eq. 1 allows for the good capillary

dimensionality estimation. The calculated diameter of capillary used to record the voltammogram from Fig. SI3-B is equal to 24.0 µm and is almost identical with the diameter measured from the SEM image (24.1 µm) available in **Figure S2**.

2.4 Pt NPs deposition at three-phase junction

In all experiments involving three-phase junction configuration, the working electrode (FTO) was contacted with the 1 mM $BTPPA_2PtCl_6$ dissolved in 1.2-DCE and 100 mM $NaBF_4$ dissolved in miliQ water. FTO was traversed the planar liquid – liquid interface or a 5 µL droplet was cast on top of it. The Ag/AgCl reference electrode and the Pt counter electrode were always placed in the aqueous phase. The corresponding schemes are available in Fig. 3-A and -B in the text of main manuscript. Pt NPs deposition was performed using chronoamperometry at E = –1.5 V.

2.5 Pt NPs deposition with planar liquid – liquid interface

The microcapillary described in section 2.3 was filled with the organic phase being 1 mM solution of $BTPPA_2PtCl_6$ in 1.2-DCE. Next, with the help of the step motor this capillary was approached to the FTO support (the approached was stopped when an edge of the capillary contacted the FTO electrode). The solution of 10 mM $NaBF_4$ in 250 mM $NaNO_3$ was added. The E = –1.5 V was applied to the FTO and hold for 30 minutes. The reference and the counter electrodes were Ag/AgCl and Pt wire respectively.

2.6 Electrochemically assisted hydrogel deposition

In all cases, the electrochemically assisted hydrogel deposition was conducted on the FTO electrode decorated with Pt NPs used as the working electrode. Ag/AgCl and Pt served as the reference and counter electrode respectively. The working electrode was polarized towards anodic potential values during linear sweep voltammetry scan. The starting potential was set to 0 V and the stop potential was set to 3.0 V. The hydrogel formation was monitored with optical polarization microscopy and the experiment was stopped when the

hydrogel framework was disrupted by the oxygen bubble(s) formation (usually in the potential range from 2.0 V to 2.5 V). The scan rate was 10 $mV \cdot s^{-1}$.

3. Water – 1,2-dichloroethane partition coefficient and Gibbs free energy of ion transfer calculations

The electrochemistry at the liquid – liquid interface can serve as a simple tool for the partition coefficient calculation, and hence, allows for the evaluation of the molecular hydrophilicity. The potential drop across the polarized liquid – liquid interface can be described with the Nernst like equation for the ion transfer reaction:

$$\Delta_{org}^{aq}\phi = \Delta_{org}^{aq}\phi_i^0 + \frac{2.303RT}{z_iF} log \frac{a_i^{org}}{a_i^{aq}} \qquad \text{(eq. 2)}$$

where $\Delta_{org}^{aq}\phi$ is the potential applied from the external power source across the liquid – liquid interface, $\Delta_{org}^{aq}\phi_i^0$ is the standard Galvani potential of ion "I" transfer, z is the chare of the transferring ion, $a_i^{org\ or\ aq}$ is the ion activity in the organic or the aqueous phase whereas R, T and F have their usual meanings. Partition coefficient can be simply defined as:

$$logP_{aq/org}^{i} = log \frac{a_i^{org}}{a_i^{aq}} \quad \text{(eq. 3)}$$

Eq. 2 can be rearranged so that the $logP_{aq/org}^{i}$ can be expressed with $\Delta_{org}^{aq}\phi$ and $\Delta_{org}^{aq}\phi_i^0$:

$$logP_{aq/org}^{i} = \frac{\Delta_{org}^{aq}\phi z_iF}{2.303RT} - \frac{\Delta_{org}^{aq}\phi_i^0 z_iF}{2.303RT} \qquad \text{(eq. 4)}$$

Furthermore, one can define the standard value of portion coefficient ($logP_{aq/org}^{i,0}$) with only $\Delta_{org}^{aq}\phi_i^0$:

$$logP_{aq/org}^{0,i} = -\frac{\Delta_{org}^{aq}\phi_i^0 z_iF}{2.303RT} \qquad \text{(eq. 5)}$$

The $\Delta_{org}^{aq}\phi_i^0 z_i F$ for BF_4^- was taken from literature, whereas for $PtCl_6^{2-}$ it was calculated using following expression:

$$\Delta_{org}^{aq}\phi_i^0 = \Delta_{org}^{aq}\phi_{1/2}^{ref} - \frac{2.303RT}{z_i F} log \frac{\gamma_i^{org}}{\gamma_i^{aq}} - \frac{2.303RT}{z_i F} \log\left(\frac{D_i^{aq}}{D_i^{org}}\right)^{0.5} \quad \text{(eq. 6)}$$

Where $\Delta_{org}^{aq}\phi_{1/2}^{ref}$ (taken from ion transfer voltammogram) is the half-wave potential, $\gamma_i^{aq\ or\ org}$ and $D_i^{aq\ or\ org}$ are the activity coefficients and diffusion coefficients of ion "i" in the concerned phase, respectively.

Moreover, with the knowledge of $\Delta_{org}^{aq}\phi_i^0$ we can easily calculate the standard Gibbs free energy of the ion transfer reaction:

$$\Delta_{org}^{aq}G_i^0 = zF\Delta_{org}^{aq}\phi_i^0 \qquad \text{(eq. 7)}$$

Calculated values of $\Delta_{org}^{aq}G_{BF_4^-}^0$ and $\Delta_{org}^{aq}G_{PtCl_6^{2-}}^0$ equal to -19.4 and -29.1 kJ·mol^{-1} respectively.

4. X-ray Photoelectron Spectroscopy (XPS)

XPS characterization was done on ThermoFisher Scientific (K-alpha surfaces analysis) instrument using a 400 µm) beam spot. The survey scan is shown in Fig. SI4-A. The majority of the peaks obtained were that for Tin and Oxygen. In the grey spot (Fig. SI4-C) the XPS spectra indicate the presence Pt as shown by the two peaks found around 71 and 74 eV respectively[5] (**Figure S4B**). Additionally, the line scan (Figure S4D) performed from the edge of the grey spot towards the region that was not exposed to H_2PtCl_6 solution during electrochemical deposition show a clear decrease in the Atomic % of Pt as opposed to Sn.

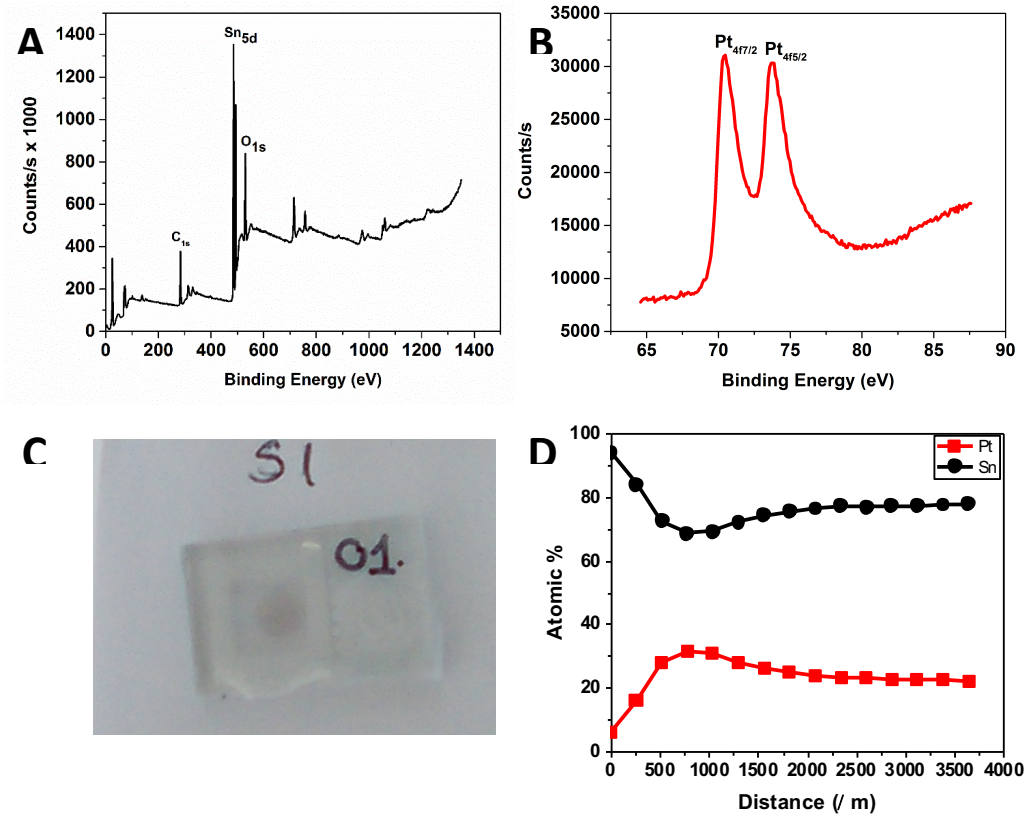

Figure S4. XPS characterization of Pt deposited FTO substrate. Survey scan (A) showing major observed peaks. Narrowed down region showing two peaks for Pt (B). Image of the sample used for XPS characterization (C). Line scan (D) spectra recorded from the edge to centre of the grey spot in (B) shows an increase in Atom % of Pt indicating the presence of Pt.

5. Scanning Electron Microscopy (SEM) & Energy Dispersive X-ray Spectroscopy (EDS)

SEM and EDS characterization was performed on a JEOL JSM 6010 InTouchScope™ microscope. Pt deposited FTO substrates were loaded onto the SEM sample holder and kept in place by the means of carbon tape. They were placed in the imaging chamber under vacuum. Images were recorded at an acceleration voltage of 20kV at various magnifications. EDS spectra was recorded of the samples by focusing on the region of interest, to obtain a map of elemental distribution (EDS elemental mapping). Particle size analysis was carried out using Fiji (ImageJ V2.0.0-rc-69/1.52i). A total of 100 particles were analysed.

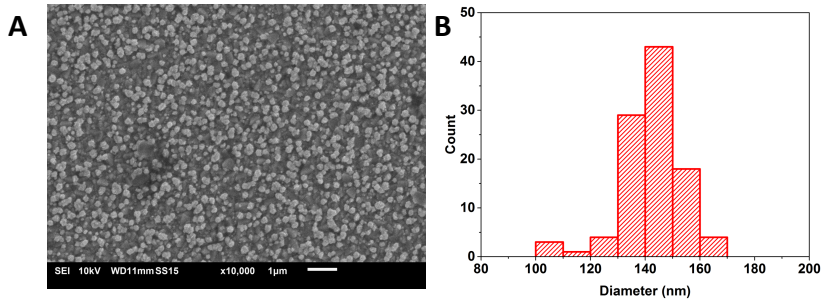

Figure S5. Full scale SEM image from Figure 1C (A) and histogram (B) of particle sizes based on image analysis.

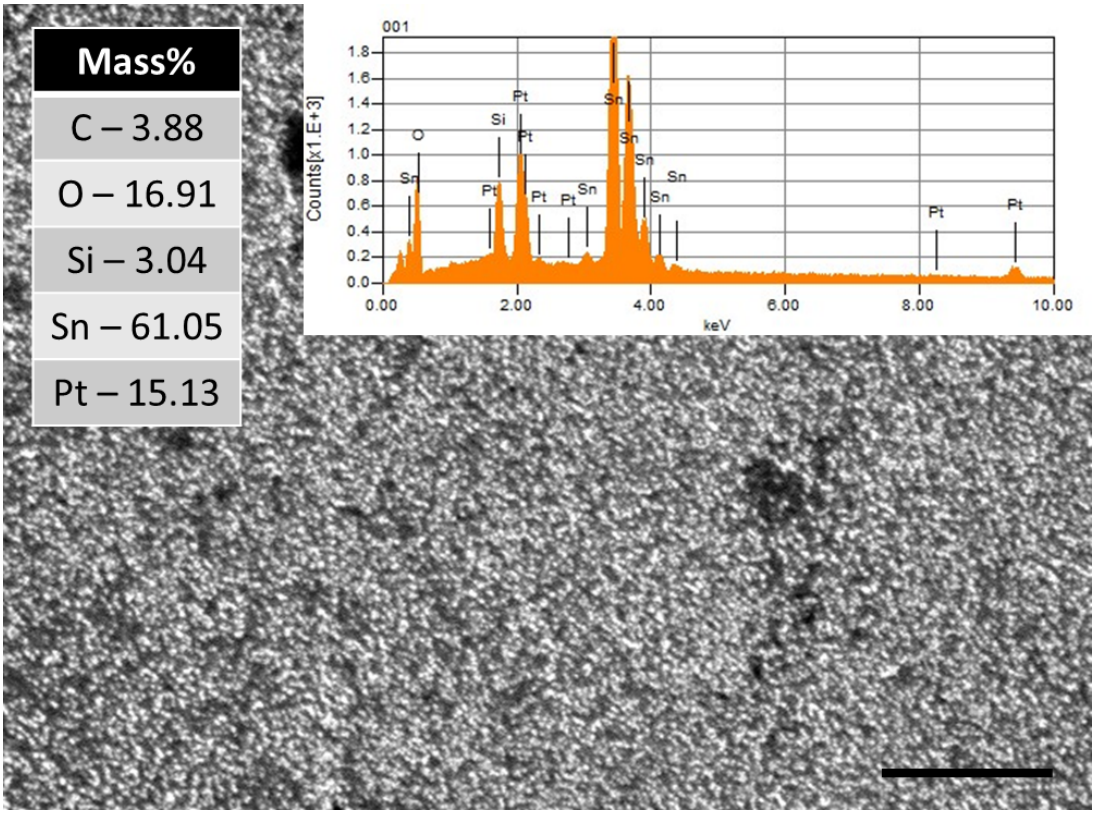

Figure S6. SEM image of the FTO modified with Pt NPs from 1 mM K_2PtCl_6 solution with corresponding EDS spectra (right inset). Table available in the left corner of the figure gives mass%.

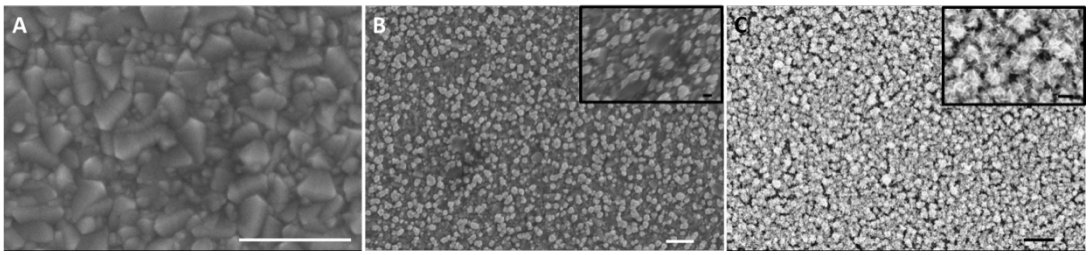

Figure S7. SEM image of the A – bare FTO; B – FTO modified with Pt NPs after 10 minutes deposition time and C – FTO modified with Pt NPs after 20 minutes deposition time. $E_{deposition}$ = – 1.5V from 1 mM K_2PtCl_6 in 0.25 M $NaNO_3$.Scale bars correspond to 1 µm (inset 200 nm).

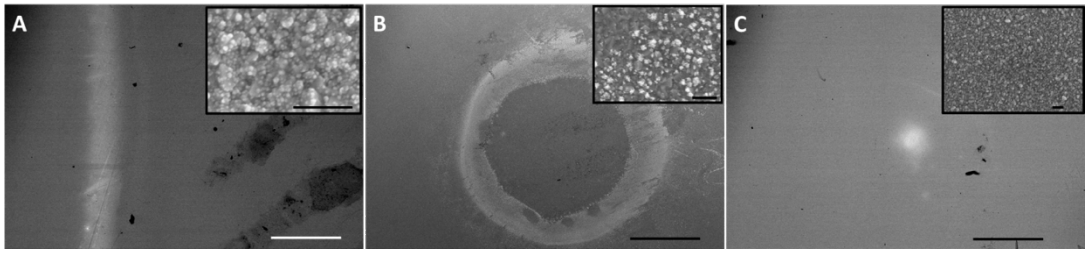

Figure S8. SEM image of the A – Pt NPs stripe ($t_{deposition}$ = 10 min, $E_{deposition}$ = – 1.5V); B – Pt NPs ring ($t_{deposition}$ = 10 min, $E_{deposition}$ = – 1.5V); and C – Pt NPs µ-spot ($t_{deposition}$ = 20 min, $E_{deposition}$ = – 1.5V). Concentration of $BTPPA_2PtCl_6$ in DCE was equal to A – 1 mM and B and C – 5 mM. Insets shows the regions with Pt NPs. Scale bares: 500 µm (inset 1 µm).

6. Transmission Electron Microscopy (TEM) & Cryo-TEM

Pt NPs deposited over Formvar® coated Cu grids were imaged in a JEOL JEM 1400 Plus electron microscope equipped with a TViPs 4K camera and EDS detector at an acceleration voltage of 120V using a single-tilt holder. Deposition was performed from 1 mM H_2PtCl_6 in 250 mM $NaNO_3$ solution at E = –1.5V for 10 min. For Cryo-TEM experiments, Quantifoil™ R1.2/1.3 100 Holey carbon Cu 200 mesh grids were first coated with Pt. The coated grids were held on a forcep and placed inside a solution of gelator precursor and electrolyte (setup shown in **Figure S8B**). Hydrogel was deposited through Linear-Sweep Voltammetry (Grid – WE, Pt strip – CE & RE) at the rate of 10mV/s from 0 to 1.8 V. The grids were then loaded

onto the loading station of a Leica Vitribot with Cryogen (liquid ethane maintained -185°C using liquid Nitrogen). The grids were immediately plunged into the Cryogen and transferred to the electron microscope. Images were recorded at an acceleration voltage of 120V under low dose conditions.

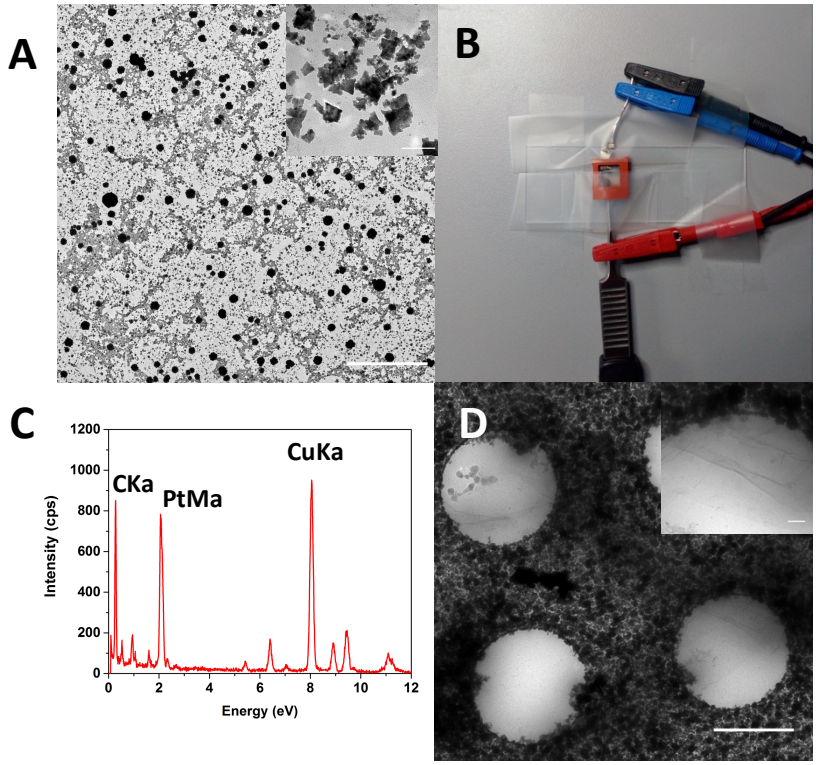

Figure S9. Transmission Electron Microscopy Characterization of Pt NPs (A) which were used in this work. Optical image (B) showing electrode configurations, red – working electrode, blue and black – counter and reference electrode respectively. EDS spectra shows presence on the Platinum (NPs), Carbon (from TEM grid) and Copper (from TEM grid). Cryo-TEM images shower hydrogel fibres formed using linear-sweep voltammetry. Scale bars are: 2 µm and 1 µm (A & D) and inset scale bars are 50 nm (A) and 100 nm (D) respectively.

7. Polarization Optical Microscopy (POM)

For Optical and Polarization microscopy measurements, Nikon Eclipse E600 POL microscope was used. Pt NPs coated FTO substrates were fastened to a slide by means of a scotch tape. The unit was then placed under the objective of the microscope. For electrochemical hydrogel formation, two rubber square spaces were placed on top on the FTO substrate in order to hold the gelator salt solution (40mM Na_2DBC in 250mM $NaNO_3$). To prevent lensing effect from the solution, a glass coverslip was placed on top. All connections were then made with the potentiostat. Illumination was provided using the microscope on Diascopic mode. Hydrogel formation was observed at different magnifications (5 – 20X) both under normal and polarized (polarizer and analyser were 90° to each to other) conditions.

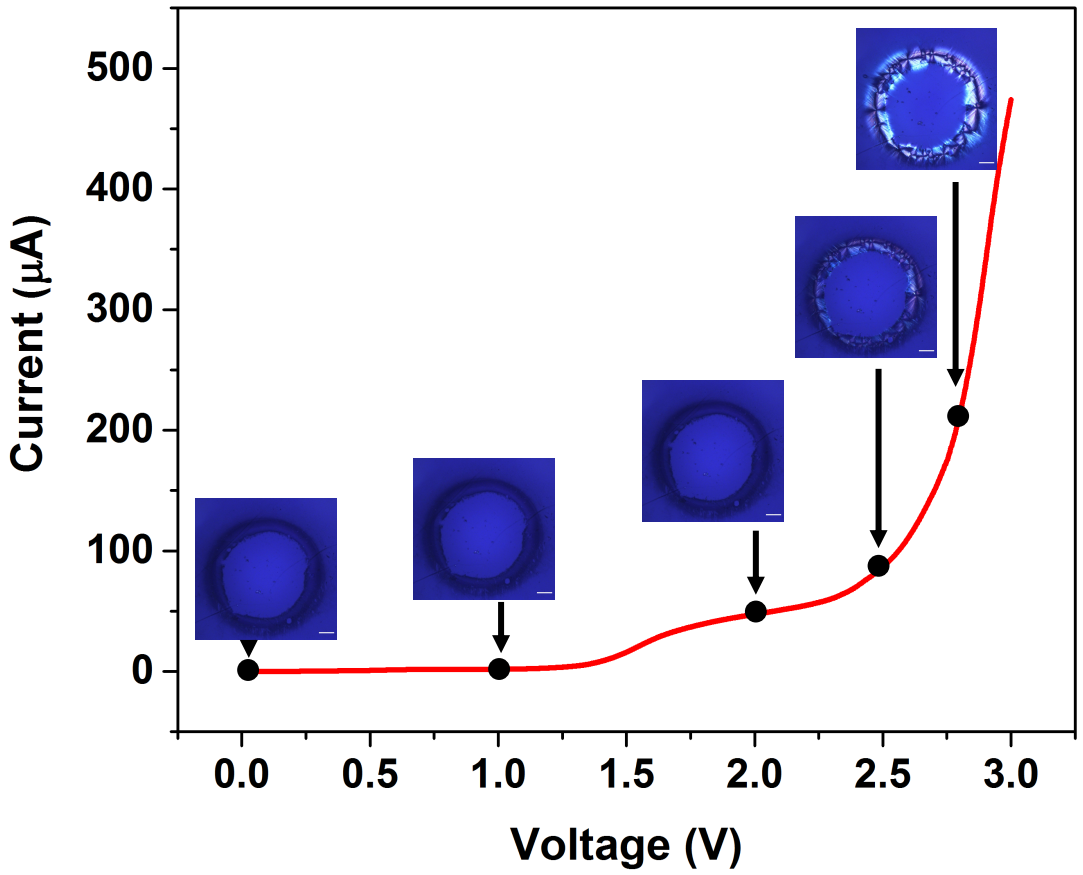

Figure S10. Linear sweep voltammogram with forward polarization towards anodic potential and scan rate equal to 10mVs^{-1} recorded at FTO electrode decorated with Pt NPs in the shape of a ring. Hydrogel formation as followed by optical microscopy under cross-polarizers progressively increases with time as indicated by the increase in the current intensity (increase in number of oriented fibres). Scale bar of microscopy images is 200 μm.

References

[1] L. Poltorak, Electrochemical modification of the liquid – liquid interface with mesoporous silica, (2015) 76. http://docnum.univ-lorraine.fr/public/DDOC_T_2015_0105_POLTORAK.pdf (accessed February 21, 2019).

[2] L. Poltorak, I. Eggink, M. Hoitink, E.J.R. Sudholter, M. De Puit, Electrified soft interface as a selective sensor for cocaine detection in street samples, Anal. Chem. 90 (2018) 8–13. Doi: 10.1021/acs.analchem.8b00916.

[3] T.J. Stockmann, J. Zhang, J.C. Wren, Z. Ding, Hydrophobic alkylphosphonium ionic liquid for electrochemistry at ultramicroelectrodes and micro liquid|liquid interfaces, Electochim. Acta. 62 (2012) 8–18. doi:10.1016/j.electacta.2011.10.087.

[4] T. Hinoue, E. Ikeda, S. Watariguchi, Y. Kibune, Thermal modulation voltammetry with laser heating at an aqueous|nitrobenzene solution microinterface: determination of the standard entropy changes of transfer for tetraalkylammonium ions., Anal. Chem. 79 (2007) 291–8. doi:10.1021/ac061315l.

[5] C. Palacio, P. Ocón, P. Herrasti, D. Díaz, A. Arranz, XPS and ARXPS study of silver underpotential deposition on platinum in acid solution, J. Electroanal. Chem. 545 (2003) 53–58. doi:10.1016/S0022-0728(03)00105-0.

Summary

Supramolecular hydrogels that are formed from low molecular weight gelators are a new class of soft materials which are gaining prominence. Depending on their molecular make up, these soft gel materials are formed based on different triggers, pH being one among them. In order to build applications with pH-triggered supramolecular gelators, it is necessary to understand their structure-property relationships and learn how to predict, control material properties. As explained in chapter 1, this thesis dealt with the above topics via three distinct fronts: Gelation kinetics, predictive modelling and electrochemical patterning.

Chapter 2 explored the gelation kinetics and its effect on the network structure of pH-triggered supramolecular hydrogels. Using the model system of N-N' Dibenzoyl L-Cystine and Glucono δ-Lactone, the kinetics of gelation was monitored using a rheometer. Based on the network branching model developed for organogelators, the rheological data was analysed and compared against network visualization obtained via Confocal Laser Scanning Microscopy. The results showed that network structure changed from linear to spherulitic as the concentration of GDL of increased. This was reconciled with the fractal dimension values obtained by the Avrami model exponent. The higher concentration of the pH-trigger, the higher the driving force for the unprotonated gelator to undergo protonation and self-assembly which leads to increased branching.

Chapter 3 continued on the topic of kinetics of gelation from a modelling perspective and sought to understand if it was possible to build a simple predictive model for gelation time, a quantity that is useful for formulations while also measurable via rheology. Using the same model system of Chapter 1, a model was built combining the acid equilibrium of the trigger – gelator and a random graph model. The random graph model considered the supramolecular gel network to comprise of free monomers, monomers with one monomer its neighbourhood, monomers with two monomers in its neighbourhood and monomers which have sticky sites. Based on the percolation threshold of the model and experimental

gelation times measured via rheology, an agreement was observed for a range of gelator and pH trigger concentrations. This was only an early attempt and would need fine tuning based of the model assumptions.

Chapter 4 shifted the focus towards fabrication of soft microgel particles based on pH-triggered supramolecular hydrogels in a simple and facile manner. Platinum (Pt) catalysed water-splitting reaction was used to create a localized proton gradient which triggered the formation and deposition soft microgels on the interface of the Pt electrodes which were exposed to a solution of decarboxylated gelator. Upon hydrogel formation, the potential applied on the electrode was reversed to be able to detach the produced hydrogel from the electrode surface through the format of a gas bubble. This principle was proved at two different Pt electrode diameters - 500 μm and 200μm respectively thereby paving the way for hydrogel patterning used Pt electrode dimension/shape.

Chapter 5 built on the technology displayed in chapter 4 and explored to miniaturize and exert further control. Through controlled deposition of Pt nanoparticles on a conductive glass substrate, different shapes and dimensions of electrodes were prepared. The electrode patterns acted as templates to shape hydrogel formation on applying electric potential. The formation of the hydrogel patterns was observed and confirmed through polarization optical microscopy.

In conclusion, this doctoral thesis provides methods to understand the microstructure, predict gelation times, and achieve controlled electrochemically-triggered fabrication of hydrogels formed by pH-triggered supramolecular hydrogelators. The methodologies presented in this thesis can be applied by researchers in academia and industry to design more efficient formulations based on hydrogels for drug delivery, cell culturing, diagnostics or other applications in the biomedical or non-medical domain.

Samenvatting

Supramoleculaire hydrogels die zijn gevormd uit gelators met een laag molecuulgewicht vormen een nieuwe klasse zachte materialen die steeds meer bekendheid krijgen. Afhankelijk van hun moleculaire samenstelling worden deze zachte gelmaterialen gevormd op basis van verschillende triggers, waarvan de pH er één is. Om toepassingen te bouwen met pH-getriggerde supramoleculaire gelators, is het noodzakelijk om hun structuur-eigenschapsrelaties te begrijpen en te leren hoe materiaaleigenschappen kunnen worden voorspeld en gecontroleerd. Zoals uitgelegd in hoofdstuk 1, behandelde dit proefschrift de bovenstaande onderwerpen via drie verschillende fronten: gelatiekinetiek, voorspellende modellering en elektrochemische patroonvorming.

Hoofdstuk 2 onderzocht de geleringskinetiek en het effect ervan op de netwerkstructuur van pH-getriggerde supramoleculaire hydrogels. Met behulp van het modelsysteem van N-N' Dibenzoyl L-Cystine en Glucono-δ-Lactone werd de kinetiek van gelatie gevolgd met behulp van een reometer. Gebaseerd op het netwerkvertakking-model ontwikkeld voor organogelators, werden de reologische gegevens geanalyseerd en vergeleken met netwerkvisualisatie verkregen via confocale laserscanmicroscopie. De resultaten toonden aan dat de netwerkstructuur veranderde van lineair naar sferulitisch naarmate de concentratie van GDL toenam. Dit werd in overeenstemming gebracht met de fractale dimensiewaarden verkregen door de Avrami-modelexponent. Hoe hoger de concentratie van de pH-trigger, hoe groter de drijvende kracht voor de niet-geprotoneerde gelator om protonering en zelfassemblage te ondergaan, wat leidt tot verhoogde vertakking. Dit was slechts een vroege poging en zou moeten worden verfijnd op basis van de modelaannames.

Hoofdstuk 3 ging verder op het onderwerp van de kinetiek van gelatie vanuit een modelleringsperspectief en probeerde te begrijpen of het mogelijk was om een eenvoudig voorspellend model voor de geleringstijd te bouwen, een grootheid die nuttig is voor formuleringen maar ook meetbaar is via reologie. Met behulp van hetzelfde modelsysteem uit Hoofdstuk 1 werd een model gebouwd dat het zuurevenwicht van de trigger-gelator en

een willekeurig grafiekmodel combineert. Het willekeurige grafiekmodel ging ervan uit dat het supramoleculaire gelnetwerk bestond uit vrije monomeren, monomeren met één monomeer in de buurt, monomeren met twee monomeren in de buurt en monomeren met kleverige plaatsen. Gebaseerd op de percolatiedrempel van het model en experimentele geleringstijden gemeten via reologie, werd een overeenkomst waargenomen voor een reeks gelator- en pH-triggerconcentraties.

Hoofdstuk 4 verlegde de focus naar de fabricage van zachte microgeldeeltjes op basis van pH-getriggerde supramoleculaire hydrogels op een eenvoudige en gemakkelijke manier. Het platina (Pt) gekatalyseerde watersplitsingsreactie werd gebruikt om een gelokaliseerde protongradiënt te creëren die de vorming en afzetting van zachte microgels op het grensvlak van de Pt-elektroden veroorzaakte die werden blootgesteld aan een oplossing van gedecarboxyleerde gelator. Bij de vorming van hydrogel werd de op de elektrode aangelegde potentiaal omgekeerd om de geproduceerde hydrogel van het elektrodeoppervlak te kunnen losmaken door het formaat van een gasbel. Dit principe werd bewezen bij twee verschillende Pt-elektrodediameters - respectievelijk 500 µm en 200 µm, waardoor de weg werd vrijgemaakt voor hydrogelpatroonvorming met behulp van de afmeting/vorm van de Pt-elektrode.

Hoofdstuk 5 bouwde voort op de technologie die in hoofdstuk 4 werd getoond en onderzocht hoe deze te miniaturiseren en verdere controle uit te oefenen. Door gecontroleerde afzetting van Pt-nanodeeltjes op een geleidend glassubstraat werden verschillende vormen en afmetingen van elektroden vervaardigd. De elektrodepatronen fungeerden als sjablonen om hydrogelvorming vorm te geven bij het aanleggen van elektrische potentiaal. De vorming van de hydrogelpatronen werd waargenomen en bevestigd door middel van optische polarisatiemicroscopie.

Concluderend biedt dit proefschrift methoden om de microstructuur te begrijpen, de geleringstijden te voorspellen en een gecontroleerde elektrochemisch getriggerde fabricage

te bereiken van hydrogels gevormd door pH-getriggerde supramoleculaire hydrogelators. De methodologieën gepresenteerd in dit proefschrift kunnen door onderzoekers in de academische wereld en de industrie worden toegepast om efficiëntere formuleringen te ontwerpen op basis van hydrogels voor medicijnafgifte, celkweek, diagnostiek of andere toepassingen in de biomedische of niet-medische domeinen

About the author

Vasudevan Lakshminarayanan was born in Chennai, Tamil Nadu, India on April 30 and was raised there. He did his schooling in Chennai and moved to Trichy to pursue his Bachelor's in Technology in Chemical Engineering at the National Institute of Technology, Tiruchirappalli (NITT). He graduated his Bachelor's with distinction in 2011 and moved abroad to the Netherlands to pursue his Master of Science in Chemical Engineering – Molecular Engineering at Delft University of Technology (TU Delft). During his Masters, Vasudevan carried out his internship and thesis work at DSM Food Specialities, Delft under the supervision of Dr. Gabriel Meesters. In 2013, he graduated 'Cum Laude' and began his PhD journey in the Advanced Soft Matter group under the supervision of Prof. dr. Jan van Esch and Dr. hab. Eduardo Mendes. During PhD, he supervised two Master students and tutored in two courses - Soft Matter for Chemical Products (MSc. level) and Structuur en Eigenschappen van Materialen (BSc. level). In 2018, he transitioned from academia to the industry to work as a R&D consultant at Bright Society. In 2019, he joined Unilever R&D as part of the Unilever future leaders' programme (UFLP). He currently manages a team of product developers as R&D Manager and delivers innovative technologies through new products in the creamy & delicious category of Dressings. Besides his technical background, Vasudevan is a singer, whistler and recording artist. He collaborates with musicians and performs in music festivals in the Netherlands, Germany and the rest of Europe.

List of publications

1. V. Lakshminarayanan, C. Chockalingam, E. Mendes, J. H. van Esch, *ChemPhysChem* **2021**, DOI 10.1002/CPHC.202100276.
2. S. El Asjadi, V. Lakshminarayanan, N. A. M. Besseling, S. J. Picken, E. Mendes, *J. Appl. Polym. Sci.* **2021**, DOI 10.1002/app.49626.
3. V. Lakshminarayanan, L. Poltorak, E. J. R. Sudhölter, E. Mendes, J. van Esch, *Electrochim. Acta* **2020**, DOI 10.1016/j.electacta.2020.136352.
4. V. Lakshminarayanan, L. Poltorak, D. Bosma, E. J. Sudholter, J. van Esch, E. Mendes, *Chem. Commun.* **2019**, DOI 10.1039/C9CC04238E.

5. K. Zhang, A. Suratkar, S. Vedaraman, V. Lakshminarayanan, L. Jennings, P. J. Glazer, J. H. van Esch, E. Mendes, *Macromolecules* **2018**, DOI 10.1021/acs.macromol.8b01158.
6. Y. Wang, F. Versluis, S. Oldenhof, V. Lakshminarayanan, K. Zhang, Y. Wang, J. Wang, R. Eelkema, X. Guo, J. H. van Esch, *Adv. Mater.* **2018**, DOI 10.1002/adma.201707408.
7. J. S. Foster, J. M. Zurek, N. M. S. Almeida, W. E. Hendriksen, V. A. A. Le Sage, V. Lakshminarayanan, A. L. Thompson, R. Banerjee, R. Eelkema, H. Mulvana, et al., *J. Am. Chem. Soc.* **2015**, *137*, DOI 10.1021/jacs.5b06988.
8. V. Le Sage, V. Lakshminarayanan, E. Mendes, R. Eelkema, J. Van Esch, *Chim. Oggi/Chemistry Today* **2014**.

Acknowledgements

I will never forget my PhD since it was and probably till date the most challenging goals that I set for myself. In this journey, I have a number of people to thank and express gratitude towards.

Firstly, I would like to thank my promotor Prof. Jan van Esch for considering me for this PhD position and being a critical supervisor. During the years we have had many discussions, scientific and non-scientific and I am grateful for your patience, the advice you gave on my work and career. I also would like to thank my co-promotor Dr. hab. Eduardo Mendes for the supervision, scientific criticisms and the stimulating conversations that transcended beyond science and even into art.

Secondly, I would like to thank Dr. hab. Łukasz Półtorak. I am extremely grateful to you for being a trusted partner in research and not shying away from my turning my wild ideas into a reality. Your scientific contributions to my thesis is immense and I will never forget your support which came at a crucial time in my PhD journey. I wish you all success in your academic career. Your resourcefulness and ability to turnaround ideas into tangible projects will only help you to scale heights in the domains of electrochemistry and soft matter.

Thirdly, I would like to thank Dr. Ivan Kryven. Thank you for the wonderful collaboration and co-authorship which has yielded a chapter in this thesis. I wish you all success further in scientific and mathematical research. I would like to thank Prof. dr. Ernst Sudhölter from OMI group for your valuable comments on our manuscripts.

Next, I would like to acknowledge the technicians in my research group who trained me and helped characterize samples on various equipment. I would like to Louw Florusse and Wiel Evers for helping me with TEM and Cryo-TEM respectively. Thanks to your training and support I could become a Cryo-TEM FPOC (First Point of Contact) for Advanced Soft Matter (ASM) group and support colleagues with their measurement needs. I would like to thank

Ben Norder for the several rheology measurements that I had to carry out during my PhD. I would like to thank Duco Bosma for the SEM measurements. I would like to thank Lars van der Meer for laboratory access and other support. I would like to thank Piet Doppert for the support with Differential Scanning Calorimetry measurements.

Beyond supervision, partnership, co-authorship, technical trainings, it is important to also have a good social life in a research group. Here, I would like to thank the group members (academic staff, Post-Doctoral researchers, fellow PhDs,) who have been in the ASM group during my PhD times – Stephen Picken, Ger Koper, Rienk Eelkema, Alexandre Olive, Chandan Maity, Elena Galan Garcia, Dainius Janeliūnas, Frank Versluis, Sander Oldenhof, Emanuel Negro, Peggy Bohlander, Qian Liu, Roman Latsuzbaia, Karolis Vilcinskas, Wouter Hendriksen, Vincent Le Sage, Matija Lovrak, Serhii Mytnyk, Susan van Rossum, Tomasz Piskorz, Hendrik Hubbe, Benjamin Klemm, Irene Piergentili, Yiming Wang, Kai Zhang. I would also like to thank Dr. Gareth Lloyd who visited our research group during my PhD period. I would like to thank Stephen Eustace for your support in NMR measurements and the lively discussions on science, culture and languages. Thank you in advance for photographing the doctoral defence ceremony as well. I would like to specially thank a few group members for their friendship and support – Cansel Temiz, Emma Westsson, Fanny Trausel. Cansel, thank you for being a great colleague during my PhD and now a family friend. Thank you for being one of my paranymphs as well. I wish you the best in your career ahead. You are a unique person and I look forward to seeing your art in major galleries in the times to come. Emma, it was great to have shared an office space and spent many hours discussing scientific, non-scientific topics and philosophies. I am grateful for friendship and look forward to the next time we will meet. Fanny, thank you for your friendship in the ASM group. It was fun organizing the ASM study excursion along with you. It was also beautiful to be part of your wedding. I wish you all the best in your industrial career.

I would like to my two Master students, Cindhuja Chockalingam and Bianca Vijai Vicveshcumar. Cindhuja, you were my first MSc. student. I am grateful to have been your

supervisor and be part of your transformation from a student to a researcher by the end of your Masters study. Your experimental results are part of this thesis and I am happy that we could publish them in a scientific journal too. I am happy to see the progress you are having in the industrial R&D domain. Bianca, thank you for being a sincere student and generating a lot of experimental data. Although we could not publish them at the end, they were crucial in making the decision to not pursue a research front. This saved time eventually. I wish you success in your career.

Next to the friendships within the research group, I was fortunate to have a support system of friends in the same building. I would like to thank Krishna Kowlgi, Venkatesh Seshan, Abrar Hakeem, Sumit Sachdeva, Naveen Kumar, Manas Mandalahalli for the many conversations that we had over coffee and chai. Towards the end of my PhD, I had the opportunity to work as the programme coordinator for the PDEng programme. Thank you, Pieter Swinkels, for the opportunity. Thank you Mahsa Hajivandi and Rene Aggenbach for your support. I would like to thank NanoNexNL for funding the majority of my PhD through programme 07A.11. I also would like to thank Menno de Jong from NanoFM for your valuable insights and discussion from the application side of the low molecular hydrogelators.

Finally, I would like to thank my inner circle. Gabrie, I cannot thank you enough for the amount of patience and steering you have given me since I became your Masters student many years ago. I look forward to your continued mentorship as I navigate through the rest of my life. Vaibhav, thank you for being one of my paranymphs and helping with the printing of this thesis. Amrit, my heartfelt thanks for the encouragement and support you gave during some of the most difficult times of my PhD journey. My best wishes to you for an incredible life and career ahead. Uncle and aunty, it is a pleasure being your son-in-law. Thank you for your presence in my life. My dearest sister Bhuvaneswari, thank you for being a patient listener and cheering me up when things were not easy. I look forward to spending time with brother-in-law Aravind and my two lovely nieces – Srinidhi and Srimaya. Amma and Appa, no words can describe the gratitude that I feel for bringing me into this world.

Thank you for raising me and instilling in me the curiosity and drive that got me through my PhD. My beloved wife, Rajamaadhanghi, thank you for coming into my life and making it so much brighter. I am grateful for your boundless love and support. I look forward to our journey through life and achieving goals together.

Vasudevan Lakshminarayanan

Delft, The Netherlands

June 2024